# HEAT TRANSFER MEASUREMENTS AND ENHANCEMENT FOR MATERIALS AND PROCESSES IN POLYMER EXTRUSION BASED ADDITIVE MANUFACTURING

by

HARDIKKUMAR MANGALDAS PRAJAPATI

DISSERTATION

Submitted in partial fulfillment of the requirements

For the degree of Doctor of Philosophy at

The University of Texas at Arlington

May, 2020

Arlington, Texas

Supervising Committee:

Dr. Ankur Jain (Committee Chairperson)

Dr. Ashfaq Adnan

Dr. Miguel Amaya

Dr. Ratan Kumar

Dr. Narges Shayesteh

ACKNOWLEDGEMENTS

This journey has been a truly amazing and life-changing experience for me. I would like to take this opportunity to express my deepest gratitude to people without whom it would not have been possible.

I wish to express my sincere appreciation to my supervisor, Professor Ankur Jain for inspiring my interest in the heat-transfer field. The interaction during the thermal conduction class has encouraged me to join his lab-Microscale Thermophysics Laboratory from Master. The opportunity he has provided me to work on experiments helped me a lot during my Ph.D. I still remember the day when I first time experimentally saw the exponential decay of temperature. I am grateful for his constant support and guidance. At the time when he knew I can handle the problem, he always let me go on my own. He has played a true role as an academic father and made be a better problem solver and thinker.

I am thankful to my dissertation committee for their time, guidance, and support. Without their valuable suggestion and advice, I would not have been able to finish my Dissertation. Their evaluation helped me to realize my shortcoming.

I would also like to thank Divya, Darshan, Swapnil, and everyone at Microscale Thermophysics Laboratory for providing constructive criticism and helping me at various stages of research. I would like to recognize the invaluable support that Kermit Beird has provided to develop the experimental setup.

I cannot forget the countless sacrifices of my family. They have always supported me mentally, emotionally, and financially without expecting anything in return. They took all the hardship in

their lives so that I can pursue this degree. I would like to thank them for understanding my ambition for this degree. I would like to thank my friends Swapnil and Saurabh for being there whenever needed.

Financial support from the MAE department at the University of Texas at Arlington is truly appreciated. Without their support, this journey could not have accomplished.

May 5, 2020.

LIST OF FIGURES

ABSTRACT

HEAT TRANSFER MEASUREMENTS AND ENHANCEMENT FOR MATERIALS AND PROCESSES IN POLYMER EXTRUSION BASED ADDITIVE MANUFACTURING

Hardikkumar Mangaldas Prajapati, Ph.D.

The University of Texas at Arlington, 2020

Supervising Professor: Dr. Ankur Jain

Additive manufacturing (AM) is a burgeoning method for manufacturing over the subtractive manufacturing methodologies. Among the various method of polymer additive manufacturing the fused deposition modeling (FDM) also known as 3D printing is the most popular technique. In this technique, a rastering extruder dispenses a thermoplastic material on to a bed at a temperature greater than its glass transition temperature to build the part. Due to the additive nature of the process, AM introduces several challenges related to functional properties such as strength, thermal conductivity, etc of the eventual part.

Measurement of thermal conductivity of additively manufactured polymer samples in the filament rastering direction and the build direction is done. Experimental data indicate significant orthotropy in thermal conductivity, with the value in the build direction being much lower than in the raster direction. As significant anisotropy is found in build and raster direction, an effort has been made to reduce it by post-processing i.e thermal annealing. This work reports significant enhancement in build-direction thermal conductivity of polymer extrusion-based parts as a result of thermal annealing. Over 150% improvement is observed when annealed at 135 °C for 96 hours. A theoretical model based on Arrhenius kinetics for neck growth and a heat transfer model for the consequent impact on inter-layer thermal contact resistance is developed. The theoretical model

may play a key role in developing practical thermal annealing strategies that account for the multiple constraints involved in annealing of polymer parts.

The process of filament-to-filament adhesion during polymer extrusion additive manufacturing (AM) is critically influenced by temperature distribution around the filament. Infrared thermography-based measurement of the temperature distribution in the filament in the standoff region and an analytical model for heat transfer in this region are studied. The analytical model predicts an exponentially decaying temperature distribution, the nature of which is governed by the characteristic length, a parameter that combines multiple process parameters such as mass flow rate, filament diameter, heat capacity, and cooling conditions.

While past works have reported side-view (x-z) temperature measurement using infrared thermography, A measurement of the in-plane (x-y) temperature field is done on the build plane by infrared thermography carried out from under the build plate using an infrared-transparent window and infrared right-angle prism mirror. Direct measurement of in-plane temperature distribution of build plate, filament, and pre-post heater is carried out with an infrared camera. A few key features revealed by measurements include symmetrical and asymmetrical temperature distributions for single and multi-line printing, respectively, upstream-downstream asymmetry, and the thermal influence between lines being limited only to the adjacent line.

TABLE OF CONTENTS

# CHAPTER 1

# INTRODUCTION

In polymer based additive manufacturing (AM), a thermoplastic material heated up to a temperature exceeding the glass transition temperature is selectively rastered from a nozzle on to a platform bed [1,2,3]. This class of additive manufacturing techniques has been widely used for a number of engineering and biomedical applications [4, 5]. While originally used only for printing of non-functional prototypes and models, polymer AM is now increasingly being investigated for printing functional components capable of bearing thermal and mechanical load [6]. Extrusion AM processes typically use materials such as acrylonitrile butadiene styrene (ABS), ULTEM, and other amorphous thermoplastics due to the wide range of temperatures in which they exhibit glassy, viscous behavior that allows them to be softened, deposited and bonded during layered printing processes.

While additive manufacturing offers capability to manufacture parts that are difficult or impossible through traditional manufacturing methods and a significantly expanded design space, additively manufactured parts often suffer from poor mechanical and thermal properties compared to the properties of the underlying materials. Several papers have reported reduced mechanical properties [7-10], showing lower modulus, strength, toughness, and strong anisotropy in parts built using polymer extrusion AM. This is usually due to incomplete adhesion between adjacent lines in the build plane or in the build direction due to unoptimized process parameters. An understanding of process-structure-property relationships as well as post-process strategies for improving thermal and mechanical properties is therefore essential.

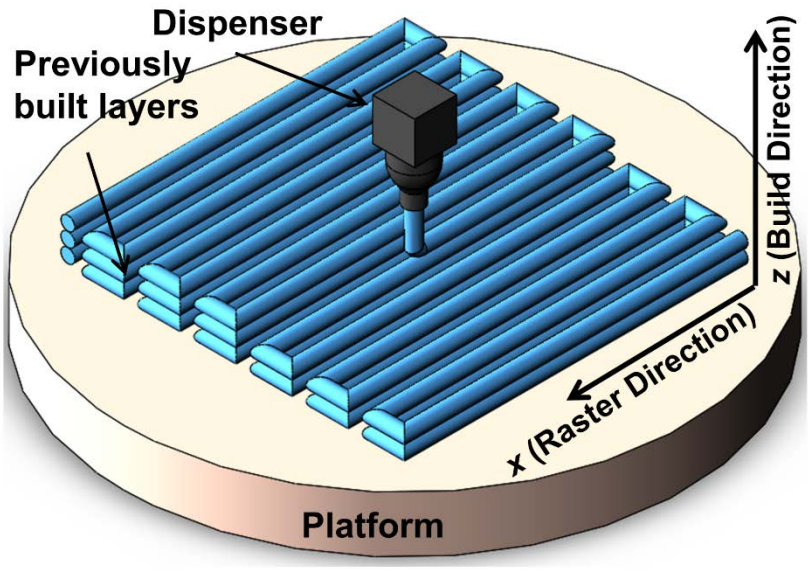


Figure 1.1 General schematic of the filament rastering process in Fused Deposition Modeling (FDM) for polymer-based additive manufacturing.

Similarly, thermal conductivity of the built part is likely to deviate from thermal conductivity of the pristine material. Direct measurement of thermal properties of the FDM built part is therefore critical. Further, due to the unique distinction between raster and build directions Figure 1.1, thermal conductivity is also expected to be different in the two directions. While there is a reasonable amount of literature on anisotropic mechanical properties of FDM-built parts [11-14], there is very little available literature on the investigation of thermal transport properties such as thermal conductivity in FDM-built parts. For example, thermal conductivity, Weng, et al. report thermal expansion coefficients of FDM-built ABS parts, but do not report thermal conductivity [15]. Other papers that measure thermal conductivity only report a single value of this property, and do not account for possible variations in different directions [16]. Shemelya, et al. have used the transient plane source method to measure the in-plane and out-of-plane thermal conductivities of FDM-built parts [17]. Some dependence on the filament material has been reported, although the effect of process and design parameters such as raster width and air gap has not been studied.

Chung, et al. [18] have also presented similar measurements to understand the effect of random voids. However, due to the randomness of voids introduced into this work, it is difficult to make any conclusions of the inherent dependence of these properties on process parameters. In addition to anisotropic thermal conductivity, the thermal contact resistance that may exist between successive layers in the z direction due to the presence of interfaces has also not been reported. Such interfacial thermal resistance may impede the flow of heat in z direction in a similar manner as the impact on mechanical strength [12,14], and reduce the z-direction thermal conductivity compared to the x direction. The lack of such data may partly be due to the significant difficulties in experimental measurement of direction-dependent thermal properties. Such a measurement requires samples with consistently aligned raster lines. This is often not available as part of standard processes on commercial FDM tools which by default produce parts with hatched line configurations. Further, forcing heat flow in a single direction during a thermal property measurement and embedding temperature sensors in successive layers in order to measure the interfacial temperature difference are also not straightforward. Despite these difficulties, characterization of anisotropic thermal transport in FDM parts is very important for understanding the fundamental relationships between process parameters and thermal properties of the built part. Such an understanding will help design FDM process flows for building parts with exceptional thermal functionality, such a ultra-low thermal conductivity, or highly directional thermal transport. A good understanding of thermal contact resistance between successive layers could potentially be used to tailor thermal properties without affecting other performance parameters. This could contribute towards understanding and reconciling multiphysics design trade-offs that exist between thermal performance, mechanical performance and weight of the built part.

In the present study, experimental measurement of anisotropic thermal conductivity and inter-layer thermal contact resistance in FDM-built parts is investigated. Measurements indicate that there exists strong anisotropy in thermal conduction in these parts, wherein thermal conductivity in the *z* direction is significantly lower than in the *x* direction. These thermal conductivity values are found to be functions of the air gap between filament lines during the deposition process. Experimental measurements are found to be in good agreement with an analytical model of thermal conduction developed in this paper. Further, a significant thermal contact resistance between successive layers is measured, and found to be a non-monotonic function of the air gap. These measurements provide a previously-unavailable insight into the fundamental nature of thermal conduction in parts built by additive manufacturing. The anisotropy in thermal conduction, as well as thermal contact resistance measured here could potentially be used for designing and building parts with novel thermal functionality, such as parts with ultra-low thermal conductivity and/or highly directional heat flow.

It is clearly important to develop strategies to improve and repair thermal conductivity, particularly in the build direction. To a limited extent, this could be done by choosing the optimal process parameters [19,20]. However, this approach has practical limitations based on the range in which these process parameters can be varied and their impact on throughput. For example, it has been shown that thermal conductivity of a polymer extrusion based part is higher for lower extrusion speed [19,20], which, however, is undesirable as it reduces throughput.

Post-process thermal annealing is a possible approach for improving thermal properties of additively manufactured parts. Thermal annealing is commonly used for improving grain structure in traditionally manufactured metal parts through exposure to high temperature for a period of time

[22]. Thermal annealing has also been used to a limited extent for modifying the microstructure of parts manufactured using polymer AM, with the motivation of improving mechanical properties [6]. Significant increase in fracture toughness has been reported for 3D printed ABS parts that are isothermally annealed at temperatures of 125ºC, 135ºC, and 175ºC for times between 2 and 168 hours [6]. The physical mechanisms and models for healing at thermoplastic interfaces via thermal treatment have been documented in the literature [22,23,24]. Improved filament-to-filament adhesion is known to occur through sintering and reptation across bead interfaces [25,26]. Similar to mechanical strength, thermal conductivity is also a strong function of the contact area and quality of bonding between filaments. Therefore, the mechanisms of reptation-based enhancement in filament-to-filament adhesion due to thermal annealing might improve thermal conductivity, similar to reported improvement in mechanical properties [6]. However, there is a lack of work on the effect of annealing on thermal conductivity, and theoretical modeling to predict the extent of thermal conductivity enhancement as a function of annealing parameters. Some work has been reported on measurement of neck size as a function of annealing temperature and time [27], and theoretical modeling of the neck growth process [28]. However, there is a lack of work on connecting these processes to the thermal properties of the built part.

In following study, an experimental and theoretical analysis of post-process thermal annealing for improving build-direction thermal conductivity in additively manufactured parts is developed. Post-process exposure of polymer extrusion built parts to different temperatures for different times, followed by measurement of build-direction thermal conductivity is carried out. Significant enhancement in thermal conductivity is reported as a result of annealing. For example, a 150% improvement is reported for annealing at 135 °C for 96 hours, which increases thermal conductivity of the part to nearly the value for the underlying material. A theoretical model based

on a power-law Arrhenius relationship between annealing parameters and inter-layer neck size, and a thermal conduction based relationship between thermal contact resistance and neck size is proposed. Theoretical predictions are found to be in good agreement with direct experimental measurements. The design space of thermal annealing parameters is explored using this theoretical model, highlighting several interesting trade-offs and important considerations in designing a robust thermal annealing strategy. Experimental data on the effect of annealing on thermal properties and the theoretical model – both not reported in past literature – are expected to improve the fundamental understanding of and optimize heat transfer in polymer AM processes, potentially leading to parts with unique thermal properties, such as high thermal conductivity, anisotropic thermal conductivity as well as spatially-varying thermal conductivity.

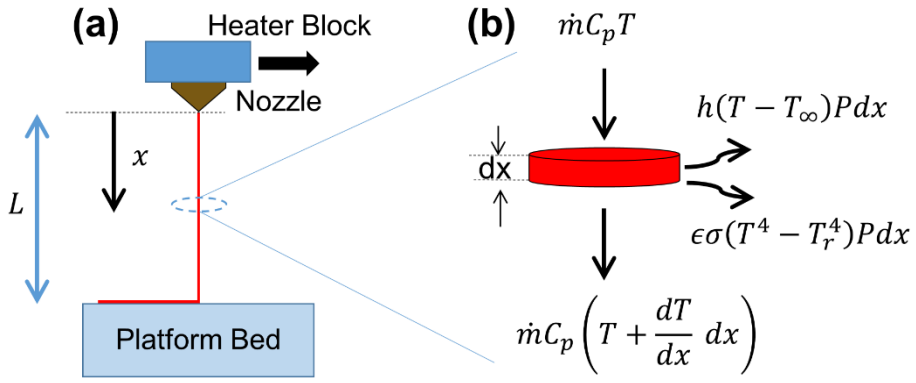


Figure 1.2. (a) Schematic of a typical polymer extrusion process showing the standoff region between the nozzle tip and platform; (b) steady state energy balance in an infinitesimal element in the filament in the standoff region showing thermal advection, convection and radiation.

Multiple heat transfer processes occur during polymer additive manufacturing and impact the quality of the built part [19,29-34]. A comprehensive understanding of thermal effects during polymer AM is critical for optimizing the physical properties of the built part. Figure 1.2 shows a schematic of this process, which can be divided into three distinct regions, each with a set of key heat transfer processes – within the nozzle assembly prior to dispense, during filament travel from

nozzle tip to bed, and on the bed. Important heat transfer processes in the nozzle assembly prior to dispensing include heating up of the polymer wire in the barrel and extrusion of the softened wire through the nozzle tip. Once dispensed on the bed, heat transfer occurs from the filament to the bed, adjacent filaments and the surroundings [30,32,27]. The nature of these processes on the bed ultimately determines the extent of bonding between adjacent filaments, and therefore the overall quality of the part [30]. In addition to the nozzle assembly and the bed, Figure 1.2 also shows a standoff region between the two that the filament travels through. Even though the stand-off distance is usually very short (lower than 1 mm), heat transfer in this region may be important to study as it determines the temperature of the filament reaching the bed. Process parameters must be chosen such that the filament does not significantly cool down between the nozzle tip and bed, so that the filament is delivered on the bed at a temperature close to the nozzle tip temperature.

Significant research has been carried out on understanding heat transfer processes within the nozzle assembly and on the bed. Several papers have reported thermal modeling and measurements of processes in the nozzle assembly in which the polymer is melted and extruded through a nozzle [33-35]. Temperature has been measured through embedded thermocouples [34]. Theoretical modeling and finite-element simulations have been reported for characterizing heat transfer, fluid flow and polymer rheology in the barrel [36-38]. Heat transfer from the barrel walls to the polymer is a key challenge here due to poor thermal conductivity of the polymer [39]. Preheating the polymer wire prior to entering the barrel has been explored as a means to improve thermal performance [39]. Infrared thermometry has also been used for measuring the temperature field in the heater block prior to dispense [39]. Hydrodynamics, non-Newtonian flow, viscoelastic effects and material rheology have all been recognized as having significant impact on thermal performance within the nozzle, and have thus been studied in detail [34,35,40].

Significant amount of work has also been carried out for understanding heat transfer in the bed once the filament has been deposited [19,29-32]. Temperature distribution during the filament bonding process has been measured through infrared thermometry [41]. Relationships between the temperature field and quality of filament-to-filament bonding have been studied [30]. Theoretical modeling and numerical simulations of temperature distribution within the filament, between filament and ambient and between filament and bed have been carried out [27]. Numerical simulations of heat transfer between successive layers has also been reported [42]. It has been shown that print speed influences the rate at which the filament cools down after deposition, but not the extent of bonding between adjacent filaments [43]. Past research in this direction indicates that bed temperature and filament temperature as deposited on the platform both govern the bonding process on the bed after the filament has been deposited [30,42]. In particular, the filament temperature at the end of the standoff region provides the thermal initial condition from where the temperature of the filament evolves as heat is transferred from the newly deposited filament to adjacent filaments, bed and the ambient. This highlights the importance of studying heat transfer in the standoff region, and of understanding which experimental parameters influence the filament temperature at the end of the standoff region. It is important to design the dispense process and standoff distance in order to minimize temperature drop in the standoff region so that the filament is deposited at nearly the same temperature as the nozzle tip.

While heat transfer processes in the nozzle and on the bed are relatively well understood, relatively less work has been reported on modeling and measurements in the standoff distance between the nozzle tip and bed. Even though the standoff distance is very short, heat transfer in this region is very important to study, since cooling off of the filament during this process may severely reduce the filament temperature as it hits the bed, and therefore impact the quality of

bonding. While nozzle temperature, stand-off distance and cooling conditions are all expected to play a key role in determining filament temperature distribution in the standoff region, an exact relationship between these parameters and the temperature distribution is not known. Clearly, there is a need for theoretical modeling of this process in order to develop accurate, predictive tools and for experimental validation through systematic measurements. Infrared thermography has been used in the past to measure the temperature profile of extruded polyethylene terephthalate (PET) microfibers from a die, but not for parameters typical for polymer AM [45]. The small value of the stand-off distance, small size of the filament and need for non-intrusive temperature measurement all present significant challenges in this direction.

This study presents theoretical modeling and experimental measurement of temperature distribution in the polymer filament in the stand-off region between the nozzle and bed. Based on an assumption of thermal steady state, an ordinary differential equation for the temperature distribution is derived and solved. The resulting solution shows that the temperature distribution is governed by a single parameter, which is named the characteristic length. Two distinct heat transfer regimes in the standoff region are identified based on the value of x0 relative to the standoff length. Experimental measurement of temperature distribution in the filament between the nozzle and bed using infrared thermography is found to be in good agreement with the theoretical model in a wide variety of experimental conditions. The validated theoretical model is analyzed for understanding the parametric regimes that result in low temperature drop between the nozzle and bed. Heat transfer analysis and measurements presented in this work improve our fundamental understanding of polymer based additive manufacturing processes, and may result in practical design tools for improving and optimizing polymer additive manufacturing processes.

In contrast to side-view measurement presented in these papers, there remains a lack of experimental measurement of in-plane temperature distribution on the build plane (x-y). Side-view measurements provide temperature distribution in the x-z plane, and therefore, specifically investigate adhesion between filaments in adjacent layers. On the other hand, adhesion between neighboring filaments on the same plane is also important, and this can be understood by measuring the in-plane temperature distribution. Unfortunately, there are several challenges in such a measurement. While a side view measurement can be carried out by mounting an infrared camera on the side of the 3D printer [41, 45], a view of the in-plane temperature field from the top is challenging, because the moving nozzle assembly blocks the view of the key region of interest where the filament is being deposited. By the time the nozzle moves away and allows optical access to the overhead IR camera, thermal diffusion would be largely complete.

Given the difficulty of measuring the temperature field from the top, next work presents an alternate approach for measurement of in-plane temperature distribution on the build plate from underneath. Figure 1.3 shows a schematic of the infrared thermography setup. Cross-section and bottom views are shown in Figures 1.3(a) and 1.3(b), respectively. A small section of the build plate is replaced with an infrared-transparent Sapphire window. In conjunction with an IR-opaque graphite layer sprayed on the build plate, and an infrared right-angle prism mirror mounted underneath, this enables visualization of in-plane temperature distribution that is not disrupted by the moving nozzle. While viewing from the bottom does not offer thermal information related to printing of the second and subsequent layers, the information obtained on the interaction between the first layer and the print bed itself may help understand filament-to-bed thermal interactions and stress development. Further, while past side view measurements help understand inter-layer bonding, the present work may help with understanding intra-layer bonding, i.e. bonding between

in-plane neighbor filaments. When combined, the two distinct measurement approaches may provide a more comprehensive thermal picture of the polymer AM process.

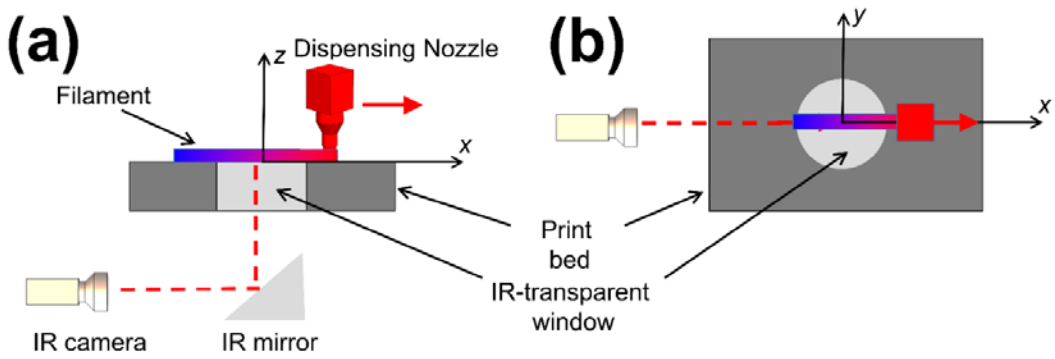


Figure 1.3 Schematic of the experimental approach for bottom-view measurement of in-plane temperature field on the print bed. (a) and (b) show side view and bottom view, respectively. Use of graphite layer on print bed facilitates measurement of in-plane temperature distribution, whereas filament temperature is measured when no graphite is present. Note that these schematics are not to scale.

# CHAPTER 2

## Measurement of Anisotropic Thermal Conductivity and Inter-Layer Thermal Contact Resistance in Polymer Fused Deposition Modeling (FDM)

**Published as**: Prajapati, H., Ravoori, D., Woods, R.L., Jain, A., 'Measurement of anisotropic thermal conductivity and inter-layer thermal contact resistance in polymer fused deposition modeling (FDM),' *Additive Manufacturing*, 21, pp. 84-90, 2018

# Introduction

Additive manufacturing, or 3D printing, is an exciting manufacturing technique relying on layer-by-layer build-up as opposed to the subtractive approach in most traditional machining processes. Specifically, in polymer-based additive manufacturing processes, filaments of a polymer are dispensed from a rastering extruder to define each layer. Due to the directional nature of this process, it is of interest to determine whether thermal transport properties of the built part are direction dependent. Such an understanding is critical for accurate design of components that serve a thermal function. This paper reports measurement of thermal conductivity of additively manufactured polymer samples in the filament rastering direction and in the build direction. Samples are designed and built in order to force heat flow only in one direction during thermal property measurement. Experimental data indicate significant anisotropy in thermal conductivity, with the value in the build direction being much lower than in the raster direction. Both thermal conductivities are found to depend strongly on the air gap between adjacent filaments. A thermal conduction model is found to be in good agreement with experimental data. These measurements are also used to determine the inter-layer thermal contact resistance, which is found to be a non-monotonic function of the air gap. Cross section images of samples confirm the strong effect of the air gap on the microstructure, and hence on thermal properties. Results from this paper provide a key insight into the anisotropic nature of thermal conduction in additively manufactured components, and establish the presence of significant inter-layer thermal contact resistance. These results may be helpful in the fundamental understanding of heat transfer in 3D-printed components, as well as in accurate design and fabrication of heat transfer components through 3D printing.

## 2.1. Experiments

### 2.1.1. Sample preparation

All tested sample are fabricated on Stratasys Fortus450-MC with ABS and ULTEM thermoplastic materials. Solid models of samples are prepared using a CAD software and converted into .stl files. These digital models are then sliced using Insight software, and tool paths of extruder are exported in .cmb format. In these experiments, the height of each layer is 0.25 mm, and raster width is 0.41 mm with multiple values of the air gap (eight for ABS and seven for ULTEM). The air gaps are chosen to be 0 mm, 0.127 mm, 0.203 mm, 0.254 mm, 0.3810 mm, 0.6350 mm are 0.7620 mm for both materials. An additional air gap of 0.508 mm is chosen for ABS. Two sets of such samples are built, such that the cylindrical axis is oriented with either the build or raster direction. All the raster lines in each layer are stacked in the same orientation. This deviates from the default practice of dispensing filaments at +/- 45$^{\circ}$ orientation in alternating layers. This is done to force heat flow in only one direction – raster or build – and therefore measure the directional thermal conductivity. Default values are chosen for all other settings such as extruder speed, dispense temperature for the main and supporting material, etc. Samples of 25.4 mm by 25.4 mm size and two different thicknesses – 5 mm and 8 mm – are built in order to facilitate thermal conductivity measurement using the 1D steady state heat flux method [46].

### 2.1.2. Thermal conductivity measurement

The primary thermal property of interest for additively manufactured samples is the thermal conductivity in raster and build directions, which can be determined from the amount of heat flux in a particular direction for a given temperature gradient in that direction. The directional thermal conductivity of additively manufactured samples is measured by a heat flow meter instrument (FOX50, LaserComp-TA Instruments), as shown in Figure 2.1. This instrument utilizes the two

thickness method. In this method, a sample is sandwiched between two flat isothermal plates maintained at different temperatures. One-dimensional heat transfer occurs through the sample, eventually resulting in a steady-state one-dimensional temperature field within the sample. Temperatures of the two plates are measured through embedded thermocouples. An insulating guard is provided around the sample to minimize stray heat loss. Heat flux is measured in both plates to confirm that there is minimal stray heat loss. Based on Fourier's law, the total thermal resistance of the sample of thickness $L_1$, which comprises material resistance through the sample, and the two contact resistances between sample surface and instrument, can be determined from

$$R_1 = \frac{L_1}{k} + 2R_C = \frac{\Delta T}{Q_1} \qquad (1)$$

Where $Q_1$ is the measured heat flux resulting from the imposed temperature gradient and $R_c$-refers to the contact resistance between sample and instrument. If the same measurement is repeated with a sample of thickness $L_2$ at the same temperature gradient, resulting in a measured heat flux of $Q_2$, then the thermal conductivity of the material being tested can be determined from

$$k = \frac{Q_1 Q_2 (L_1 - L_2)}{(Q_2 - Q_1)\Delta T} \qquad (2)$$

where the sample-to-instrument thermal contact resistance is assumed to remain the same in both experiments.

In these experiments, the sample thicknesses are chosen to be 8mm and 5mm in order to stay within the instrument's heat flux measurement capability. Further, each measurement is carried out twice to ensure repeatability.

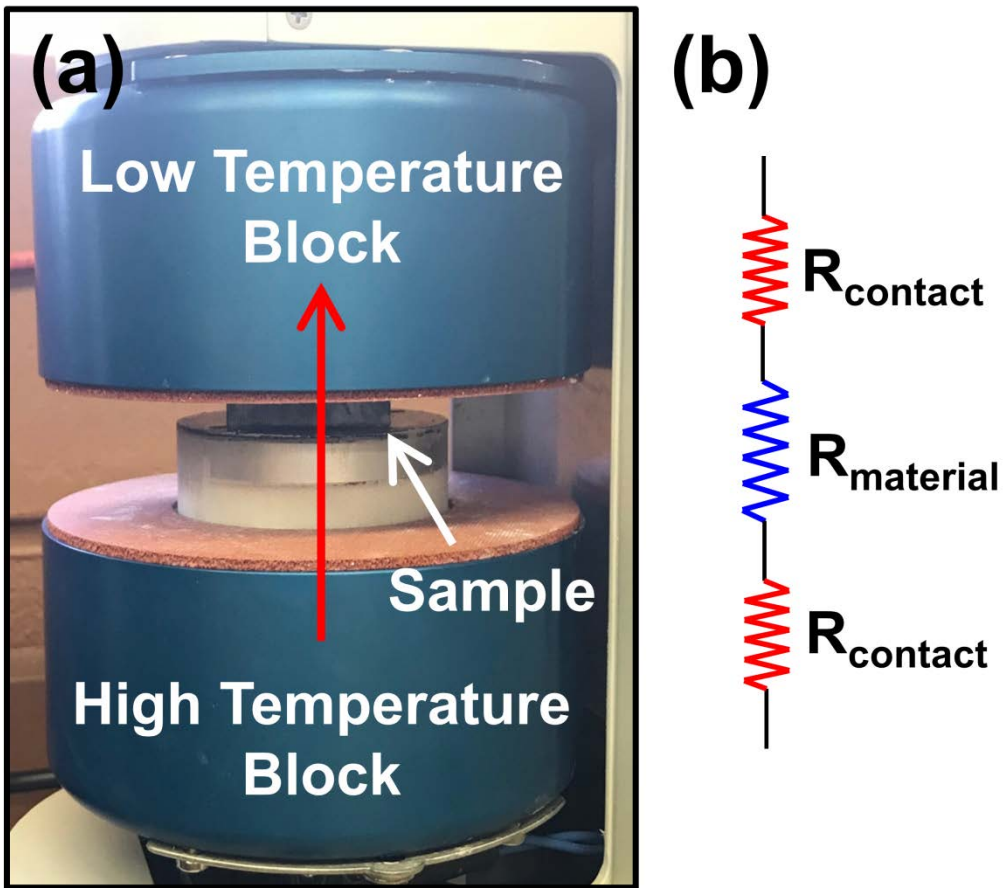


Figure 2.1 (a) Picture of the experimental setup based on one-dimensional steady state heat flux for measurement of thermal conductivity of additively manufactured components; (b) Schematic of the key thermal resistances involved in this measurement.

### 2.1.3. Visualization of cross section of samples

After thermal property measurements, samples are cut in the *yz* plane in order to visualize the internal structure of the samples. Since ABS and ULTEM are thermoplastic, the use of conventional cutting tools is found to be ineffective, as it leads to removal and re-deposition of the material on the internal structure during the cutting process. Instead, a small, the lead cut is made in the sample, which is then soaked in liquid nitrogen for 2-3 mins. This makes the sample temporarily brittle, which can be easily broken by applying an impact load on the lead cut. This

results in preservation of the internal structure of the sample, making it possible to image the cross-section. A Nikon Eclipse ME600 microscope is used for visualization.

### 2.2. Theoretical modeling of thermal conductivity and thermal contact resistance

Test samples printed using the procedure outlined in section 2.1 comprise aligned filaments with a width of $w_f$ with an air gap of $w_a$ between adjacent filaments. In these experiments, each layer is built with the same filament orientation. In order to consolidate the part, the edges of the part are usually printed with zero air gap. Since this covers only a small fraction of the part along the outside edges, estimated to be less than 5%, it is reasonable to neglect this for heat transfer analysis, and assume heat transfer in the part to be driven by thermal resistances through the filament material and air gap, and by inter-layer thermal contact resistances. While the final shape of the filament may be quite complicated, as an approximation, each filament is assumed to be a parallelepiped, with a width $w_f$ in the cross section, shown schematically in Figure 2.2. The air gap between adjacent filaments is assumed to be $w_a$. Assuming that the total number of layers is $n$, heat transfer in the raster direction comprises $n$ thermal resistances in parallel, each of which represent the thermal resistance of a layer. The thermal resistance of each layer in turn comprises $x$-direction thermal resistances from the filament and air gap, arranged in parallel. Assuming the thermal conductivities of the filament and air to be $k_f$ and $k_a$ respectively, the effective thermal conductivity of the additively manufactured part in the raster direction is found through the series-parallel combinations of thermal resistances to be

$$k_x = \frac{w_a k_a + w_f k_f}{w_a + w_f} \tag{3}$$

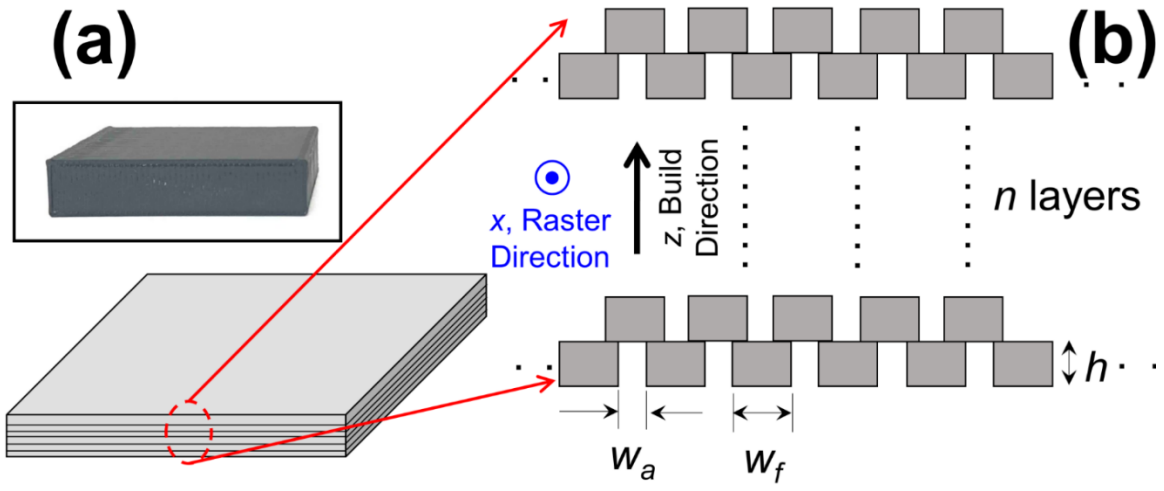


Figure 2.2 (a) Overall schematic of a FDM-printed part, also showing a picture of a sample printed in this work; (b) Schematic model of the internal geometry of an additively manufactured component showing the filament and air components in the thermal resistance network in a single layer, and in the entire part comprising multiple layers in the build direction.

In the build direction, the thermal resistances of the *n* layers are arranged in series. Thermal resistance of each layer in turn comprises *z*-direction thermal resistances of the filament and air gap arranged in parallel. In addition, interfacial thermal contact resistance between adjacent layers also contributes towards total thermal resistance in the build direction. Combining all these contributions, the effective thermal conductivity in the build direction is found to be

$$\frac{1}{k_z} = \frac{w_a + w_f}{w_a k_a + w_f k_f} + \frac{R_c}{h} \qquad (4)$$

where $R_c$ is the thermal contact resistance between adjacent layers and $h$ is the layer height.

Note from equations (3) and (4), that in the absence of $R_c$, $k_x$ and $k_z$ are equal to each other. However, due to the presence of non-zero thermal contact resistance occurring due to imperfect thermal contact between adjacent layers, equations (3) and (4) show that $k_z$ will be lower than $k_x$, thereby resulting in thermal conduction anisotropy in the additively manufactured part.

Equations (3) and (4) show that $R_c$ can be determined from measured values of $k_x$ and $k_z$ as follows:

$$R_c = h\left(\frac{1}{k_z} - \frac{1}{k_x}\right) \qquad (5)$$

Equations (2) and (3) also show that both $k_x$ and $k_z$ are functions of process and design parameters, including filament material, raster width and air gap. This indicates the possibility of tuning effective thermal conductivities in both directions by changing these process and design parameters.

The next section presents results from experimental measurements of thermal conductivities in the raster and build directions, as well as the interfacial thermal contact resistance obtained from equation (5). Comparison of experimental data with analytical model results is also discussed.

### 2.3. Results and Discussion

Thermal conductivity in the raster direction is measured for two different filament materials, ABS and ULTEM for a number of values of $w_a$, the air gap between filament lines. For these experiments, the filament line width, $w_f$, is held constant at 0.41 mm. Samples of thicknesses 5mm and 8mm, in which the raster direction coincides with the axial direction of the thermal conductivity measurement setup shown in Figure 2.2 are designed and built. Figures 2.3(a) and 2.3(b) plot the measured thermal conductivity in raster direction, $k_x$ as a function of air gap, $w_a$ for ABS and ULTEM respectively. The theoretical relationship between the two based on equation (3) from section 2.2 is also plotted in these figures. Figure 2.3 shows that as the air gap increases, thermal conductivity in the raster direction reduces significantly for both materials in a similar fashion. This occurs primarily because of the increased fraction of air gap in the cross-section, and

therefore increased resistance to heat flow in the $x$ direction. Experimental data are in good agreement with the curve representing the analytical model, which shows that the nature of heat transfer in the raster direction is well described by series and parallel combinations of thermal resistances through the material and air gaps. Even though the analytical modeling is carried out assuming rectangular cross-section of the extruded filaments, it nevertheless results in good agreement with experimental data. As the air gap increases from 0 mm to 0.76 mm in the case of ABS, there is a 54 % reduction in $k_x$, which is quite significant. This relationship between design parameters such as $w_a$ and ultimate thermal properties of the part as shown in Figure 2.3 is corroborated by cross-section imaging of these samples. There is some departure between thermal conductivity measurements and theoretical model when the air gap is very large. This is believed to occur because at large air gaps, filaments are not well supported by filaments in the underlying layer, due to which some mechanical distortion of the filaments might occur and cause minor departure from the microstructure assumed by the theoretical model.

Figure 2.4 shows cross-sections of ABS samples with zero and 0.25 mm air gap, at a filament width of 0.41 mm. These images clearly show change in the microstructure as the air gap increases, which causes the reduction in the measured raster-direction thermal conductivity. Figure 2.4 shows some distortion in the cross section of the filaments, particularly at low air gaps. However, because of the higher thermal resistance through the air gap compared to the filament, this is not expected to dramatically impact overall thermal conductivity.

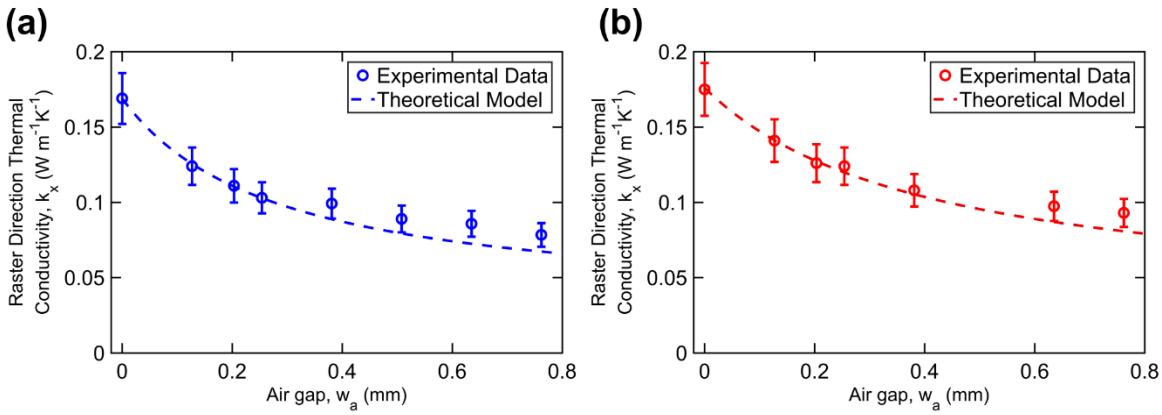


Figure 2.3 Measured thermal conductivity in the raster direction, $k_x$, as a function of air gap for (a) ABS; and (b) ULTEM filament materials. Predicted curves from the analytical model, equation (3) are also plotted in each case.

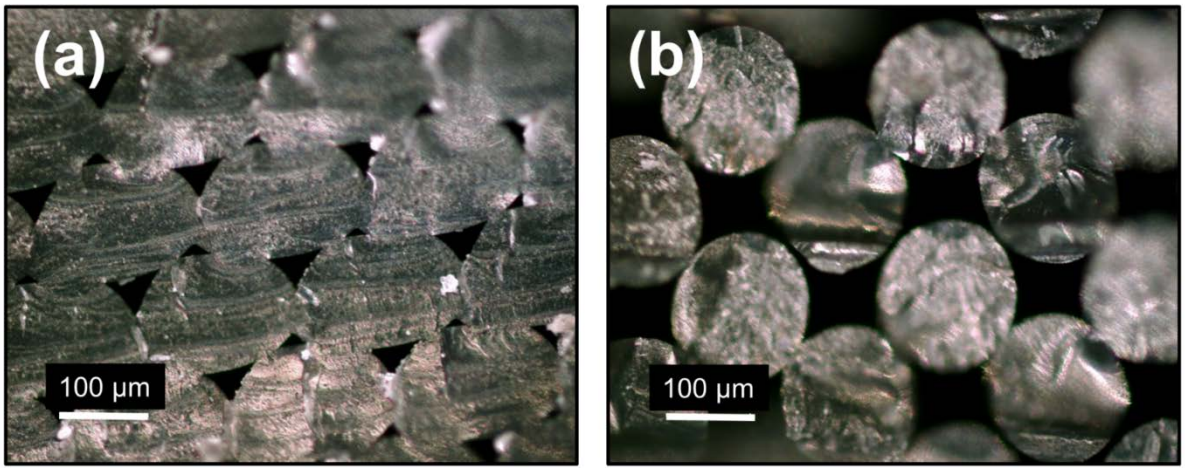


Figure 2.4 Cross section images of two ABS samples with (a) zero; and (b) 0.25 mm air gap, showing significant difference in microstructure. In each case, the raster direction, *x*, is normal to the plane of the image.

Experiments are then carried out to measure thermal conductivity in the build direction, $k_z$ for multiple values of air gap while the filament width is fixed at 0.41 mm, similar to measurements of thermal conductivity in the raster direction. Similar to previous experiment, samples of 5mm and 8mm thicknesses in which the build direction is aligned with the axial direction of the thermal conductivity measurement setup are designed and fabricated. Figure 2.5 plots these data and shows, similar to Figure 2.3, a reduction in $k_z$ as the air gap increases. Measurements indicate that

at any value of the air gap, thermal conductivity in the build direction, $k_z$, is significantly lower than in the raster direction, $k_x$. This establishes that thermal conductivity in the FDM-built part is significantly anisotropic. The built part offers greater impedance to heat flow in the build direction, $z$, than in the raster direction, $x$. This anisotropy, which may be represented by the ratio $k_z/k_x$ is also plotted in Figure 2.5. Figure 2.5 shows that the degree of anisotropy starts at close to 1.0 when the air gap is zero, and reduces sharply as the air gap increases. Eventually, this ratio plateaus out at large values of the air gap. The ratio $k_z/k_x$ is found to be as low as 0.60 at large air gap, which represents significant anisotropy in thermal conduction.

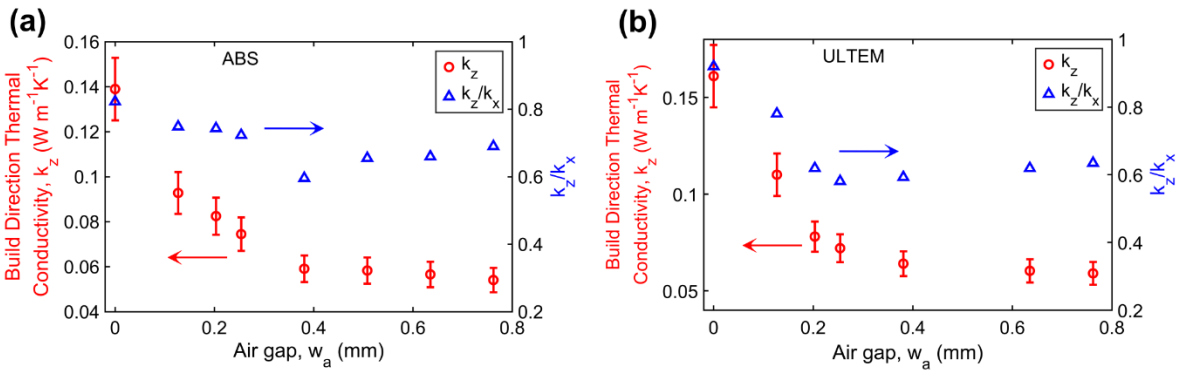


Figure 2.5 Measured thermal conductivity in the build direction, $k_z$, as a function of air gap for (a) ABS; and (b) ULTEM filament materials. The ratio $k_z/k_x$, which represents the degree of anisotropy is also plotted in each case.

The observation that thermal conductivity in the build direction, $k_z$ is always lower than in the raster direction, $k_x$ establishes the presence of significant thermal contact resistances at the interfaces between successive layers in the part. Data shown in Figures 2.3 and 2.4 are consistent with

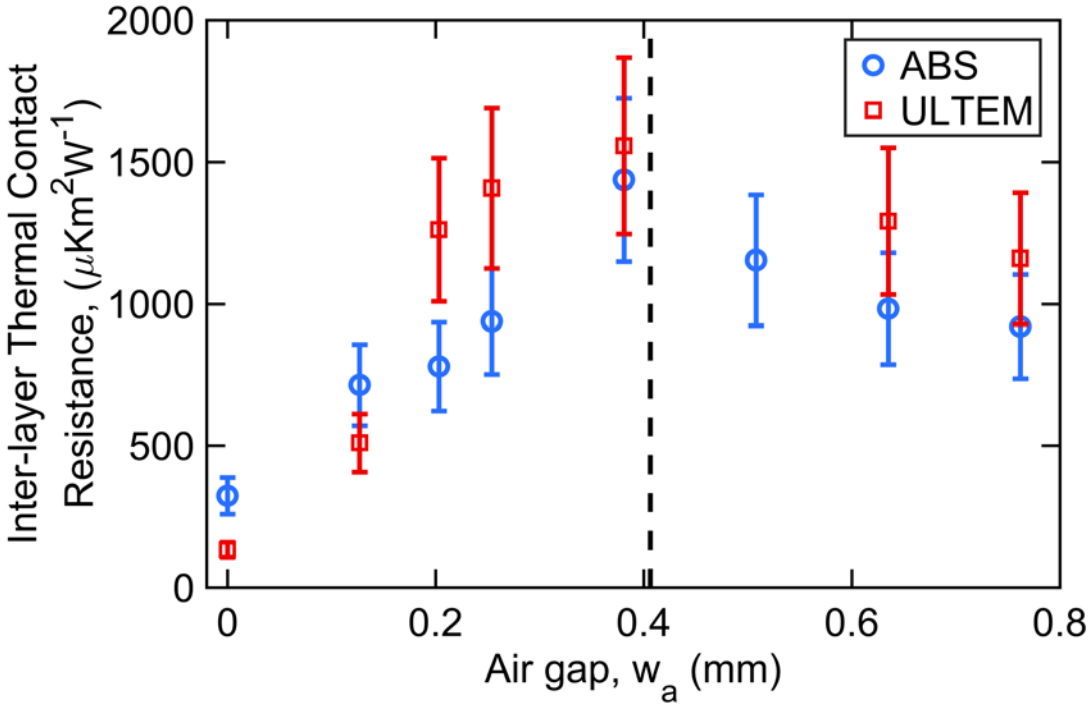


Figure 2.6 Measured inter-layer thermal contact resistance as a function of air gap for both ABS and ULTEM filament materials. Dashed vertical line in this Figure shows the filament width, which is held constant at 0.41 mm. Top x-axis shows values of the ratio $w_a/w_f$.

the theoretical model presented in section 2.2, specifically equations (2) and (3), which predict lower thermal conductivity in the build direction than in the raster direction. due to the presence of thermal contact resistance at interfaces between successive layers. The value of the interfacial thermal contact resistance at any specific air gap can be determined by using measured values of $k_x$ and $k_z$ in equation (4). Thermal contact resistance computed in this manner is plotted as a function of air gap in Figure 2.6, which shows that as the air gap increases, thermal contact resistance also goes up. This shows that with increasing air gap, there is increased impedance to heat flow in the build direction not only because of the increased fraction of air in the cross-section, but also because larger air gaps cause reduction in adherence between successive layers, and thus increased thermal contact resistance at the interfaces. Interestingly, once the air gap exceeds the

raster width, the thermal contact resistance does not rise any further, and actually reduces somewhat. This is likely because once the air gap exceeds raster width, the nature of contact resistance between successive layers changes, since filaments in successive layers are no longer in direct contact with each other. Accurately accounting for this interesting, non-monotonic effect of air gap on build-direction thermal contact resistance measured here is important for accurate thermal design. Careful consideration of these parameters may help design novel parts with ultra-low thermal conductivity without compromising on mechanical strength.

A set of finite simulations are carried out in order to establish the importance of the measured anisotropy in thermal conduction in additively manufactured components reported here. A thin, additively manufactured insulating wall of thickness 50 mm is considered, wherein heat flux of 100 $W/m^2$ enters the wall on one face and flows across the wall, while the other face is maintained at constant temperature. It is assumed that the thickness of the wall is aligned with the build direction, *z* axis. The wall is assumed to be large in the other two directions, as is the usual case for analyzing heat transfer through an infinite wall. Two simulations are carried out in order to demonstrate the importance of thermal conduction anisotropy. In the first case, the material is assumed to be isotropic, so that the values of $k_x$ and $k_z$ are the same. In the second case, the anisotropic nature of the material is accounted for, and the correct values of $k_x$ and $k_z$ based on measurements reported here are used. Figure 2.7 plots the temperature field in the thin wall for both isotropic and anisotropic cases. The peak temperature in the first case, where $k_x$ and $k_z$ are incorrectly assumed to be equal to each other is much lower than the more realistic second case, where thermal anisotropy is accounted for. This shows that neglecting the anisotropy

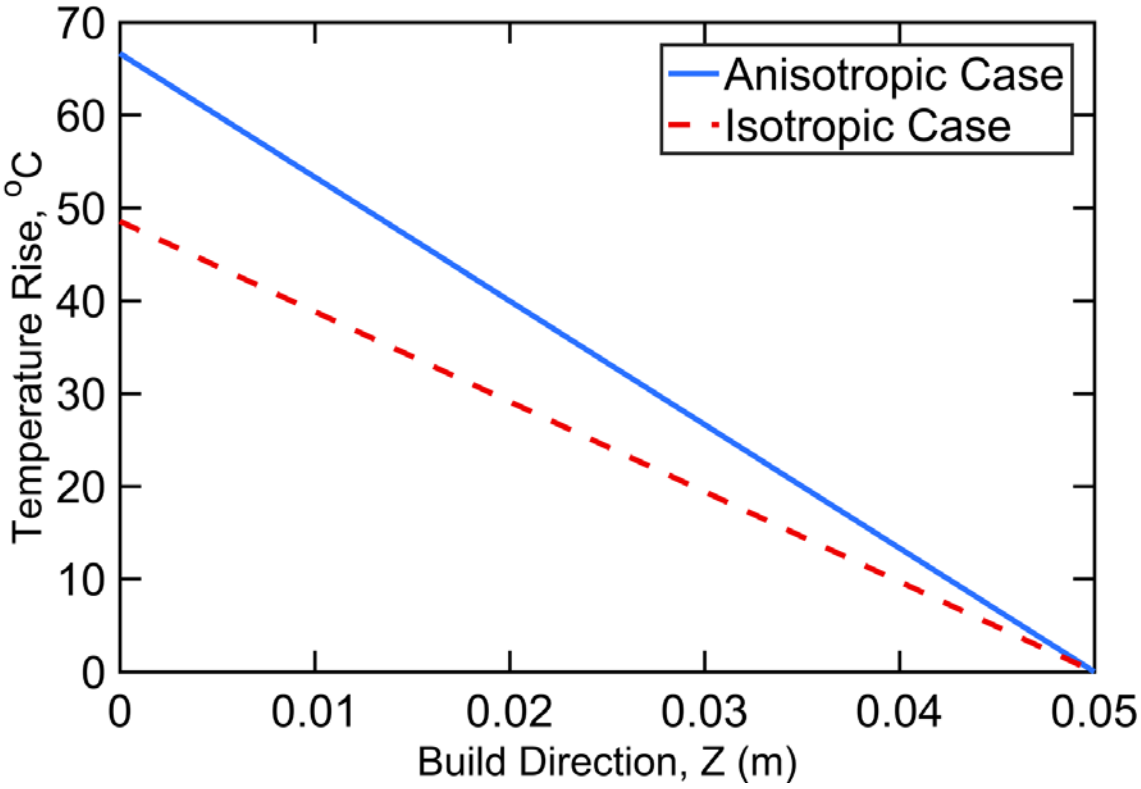


Figure 2.7 Finite element simulations of the steady-state temperature field in an additively manufactured thin wall. Comparison between results based on isotropic and anisotropic thermal conductivity are shown.

in the material that occurs due to the additive manufacturing process can lead to significant under-prediction of the temperature field in the material. As more and more functional parts begin to be additively manufactured, the effect of the manufacturing process on thermal properties, particularly on anisotropy in thermal conductivity must be correctly accounted for in order to ensure accurate design and operation of such parts.

# CHAPTER 3

## Improvement in build-direction thermal conductivity in extrusion-based polymer additive manufacturing through thermal annealing

**Published as:** Prajapati, H., Chalise, D., Ravoori, D., Taylor, R.M., Jain, A., 'Improvement in build-direction thermal conductivity in extrusion-based polymer additive manufacturing through thermal annealing,' *Additive Manufacturing*, 26, pp. 242-249, 2019.

## Introduction

While additive manufacturing offers significant advantages compared to traditional manufacturing technologies, deterioration in thermal and mechanical properties compared to properties of the underlying materials is a serious concern. In the context of polymer extrusion based additive manufacturing, post-process approaches, such as thermal annealing have been reported for improving mechanical properties based on reptation of polymer chains and enhanced filament-to-filament adhesion. However, there is a lack of similar work for improving thermal properties such as thermal conductivity. This paper reports significant enhancement in build-direction thermal conductivity of polymer extrusion based parts as a result of thermal annealing. Over 150% improvement is observed when annealed at 135 °C for 96 hours. The effect of annealing temperature and time on thermal conductivity enhancement is investigated through experiments. A theoretical model based on Arrhenius kinetics for neck growth and a heat transfer model for the consequent impact on inter-layer thermal contact resistance is developed. Predicted thermal conductivity enhancement is found to be in good agreement with experimental data for a wide range of annealing temperature and time. The theoretical model may play a key role in developing practical thermal annealing strategies that account for the multiple constraints involved in annealing of polymer parts. This work may facilitate the use of polymer extrusion additive manufacturing for parts that are required to withstand thermal loads.

### 3.1. Experiments

Experiments are carried out to investigate improvement in build direction thermal conductivity through thermal annealing. Next sub-sections describe various aspects of the experimental approach.

### 3.1.1. Sample design and printing

ABS samples are designed to facilitate build-direction thermal conductivity measurement and printed on a Stratasys Fortus 450mc tool. As described in section 3.1.3, thermal conductivity measurement through differential heat flux measurement requires two samples of the same cross section but different thicknesses. In this case, two samples of 4 mm and 8 mm thicknesses, and 36 mm by 36 mm cross-section are designed. These dimensions ensure sufficient difference in material thermal resistances of the two samples as well as compatibility with the measurement equipment. CAD drawings of the samples are prepared through SolidWorks and processed in Insight slicing software. The detailed toolpath is then exported as a .cmb file and fed into the control software of the 3D printer. Geometrical parameters of the sample include 0.25 mm layer height, 0.41 mm raster width and 0.25 mm air gap. These parameters are chosen in order to minimize neck formation during the printing process prior to annealing. Raster lines are stacked in the same orientation in all layers. The build direction in the printing process is aligned with the thickness of the samples, so that the build-direction thermal conductivity can be measured in isolation from thermal conductivity in other directions.

Figure 3.1(a) shows a picture of a representative pair of samples printed for build-direction thermal conductivity measurement.

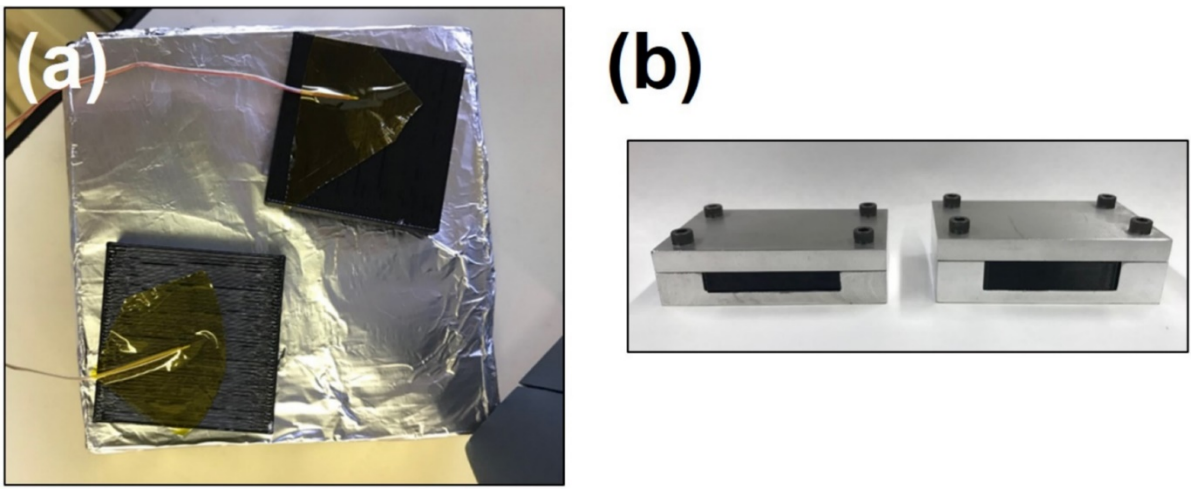


Figure 3.1 (a) Picture of a pair of samples for build-direction thermal conductivity measurement; (b) Picture of the sample holder for mounting samples during annealing process.

3.1.2. Experimental setup for thermal annealing

All thermal annealing experiments are carried out in a Boekel Scientific high temperature oven. A set of oven calibration tests are carried out in advance of the experiments, in order to account for possible difference between the set temperature and actual temperature of the sample inside the oven. In these experiments, a test sample is placed in the sample holder and kept in a fixed location of the oven. Figure 3.1(b) shows a picture of the sample holder used in this work. Temperature of the sample is measured with a T-type thermocouple and the set temperature of the oven is adjusted in order for the sample temperature to reach the desired value. By doing, oven temperature setting needed for each sample temperature of interest is determined.

In each experiment with an actual sample, the oven is first set to the desired temperature and allowed to reach steady state, as determined by stability of temperature measurement from a thermocouple inside the oven. The test sample, mounted in a sample holder in introduced. After the desired time duration for the annealing experiment has been reached, the oven is switched off

and allowed to cool down on its own. This prevents thermal shock to the sample if withdrawn from the oven and exposed abruptly to the relatively cold ambient. Once the oven has cooled down to room temperature, the sample is dismounted from the sample holder. Minor warping of samples is found to occur at corners in some cases, which is correctly by gently filing the corners of the sample on both faces.

A sample holder is designed and fabricated for holding the sample, thereby providing repeatability across multiple experiments. The sample holder is made from aluminum to provide the least temperature variation and thermal resistance around the sample. The bottom plate of the sample holder has a cavity to house the sample, while the top plate covers the sample. A cut is provided to insert a thermocouple to monitor the sample temperature during annealing.

### 3.1.3. Experimental setup for thermal conductivity measurements

Fox50 apparatus based on differential heat flux measurement method is used for measuring build direction thermal conductivity of samples before and after thermal annealing. This method is based on measurement of heat flux induced by a fixed temperature difference across the thickness of the sample. Interfacial thermal contact resistance between the sample surface and instrument is eliminated by separately measuring the heat fluxes $Q_1$ and $Q_2$ for two samples of different thicknesses $L_1$ and $L_2$ subjected to the same temperature difference $\Delta T$. As shown in Figure 3.2, the two key thermal resistance that combine in series to form the measured total thermal resistance comprise the material thermal resistance, which is proportional to the sample thickness, and the sample-to-instrument thermal contact resistance, which is assumed to be the same for both samples. This is a reasonable assumption since the surface finish of both samples is the same. The unknown sample-to-instrument thermal contact resistance may be eliminated by subtracting the

measured total thermal resistance. The thermal conductivity of the material can be shown to be given by [46,47]

$$k = \frac{Q_1 Q_2 (L_1 - L_2)}{(Q_1 - Q_2)\Delta T} \tag{1}$$

This method has been used extensively for measurement of thermal conductivity in a variety of engineering applications, including for additively manufactured samples [46,47].

Figures 3.2 shows a schematic to illustrate the two key thermal resistances in the thermal conductivity measurement approach.

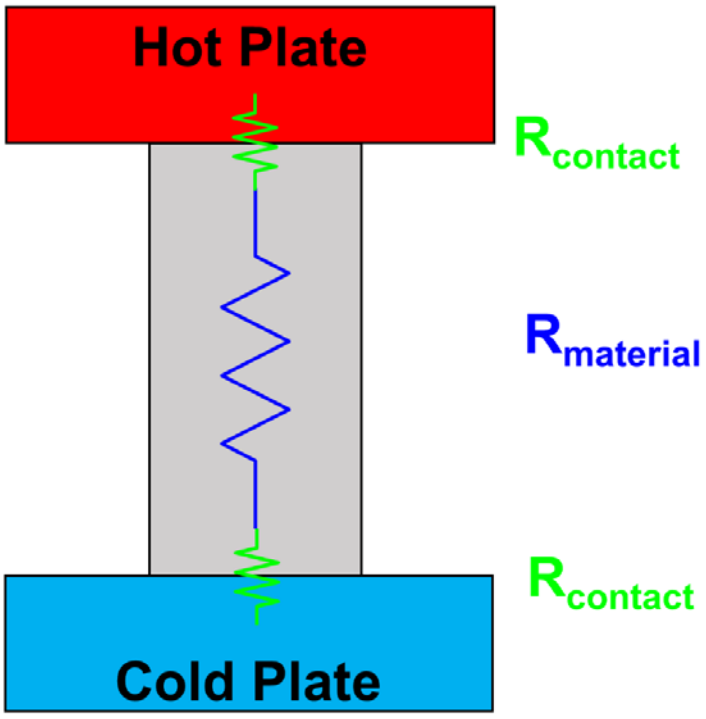


Figure 3.2 Schematic of various thermal resistances in the thermal conductivity measurement experiment.

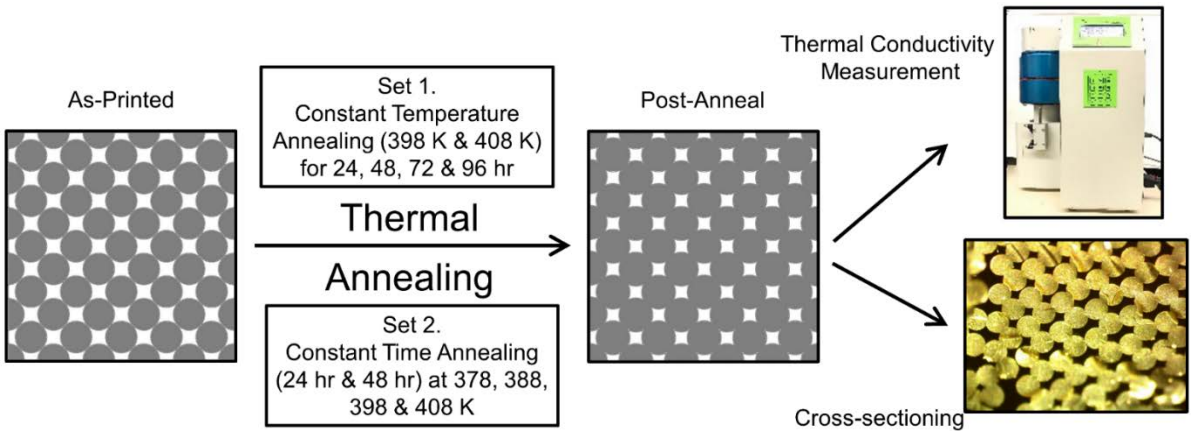


Figure 3.3. Schematic of the experimental flow followed in this work, including details of annealing times and temperatures for two sets of annealing experiments.

Figure 3.3 shows a schematic of the experimental approach, including details of the annealing times and temperatures investigated in this work.

### 3.1.4. Cross section visualization

After annealing and thermal property measurements, samples are cut normal to the raster direction, such that the plane of the cut reveals the cross-section microstructure of filaments. This facilitates quantitative measurement of filament-to-filament necking before and after annealing. These data play a key role in validating and determining the coefficients of the theoretical model. Since ABS is a thermoplastic material, any attempt to cut it with conventional methods will disrupt the internal structure due to local melting and redistribution of material. Instead, a small notch is made around the sample, which is then soaked in liquid Nitrogen for 1-2 minutes. This temporarily makes the sample brittle, which can be broken by applying an impact load from a hammer at the notch while the sample is still very cold. It is found that this approach results in a clean cut that does not disrupt the internal filament microstructure of the samples.

Cross-section images are taken with a MU1000 camera mounted on an AmScope microscope. Neck size is measured from images taken at the same zoom setting. An image of two lines with a spacing of 1mm captured by the camera is used for calibration and quantification of the magnification. All cross-section images are then taken with the same settings. Each image corresponding to a particular annealing time and temperature is found to have 10-20 visible necks. An average of these neck size measurements is recorded as the neck diameter for that particular annealing experiment.

## 3.2. Theoretical Modeling

Recent experiment measurements have shown lower thermal conductivity in the build direction compared to the raster direction due to significant thermal contact resistance between layers in the build direction [47]. This section proposes a theoretical model for determining the extent of enhancement in build-direction thermal conductivity when a sample is isothermally exposed to a high temperature $T$ for a time duration $t$. A relationship between the two key annealing parameters – temperature and time – and neck growth based on Arrhenius kinetics is discussed in Section 3.2.1. This neck growth is then shown to lead to reduced thermal contact resistance, and hence, increased thermal conductivity in sub-section 3.2.2.

### 3.2.1. Kinetic growth model

Microstructural growth in materials in response to thermal annealing is well known, with extensive experimental data and theoretical models in the past literature. For example, grain growth in crystalline materials occurs when exposed to high temperature for a certain time, and is used routinely for improving properties of traditionally manufactured metal parts [21]. The growth

of grains is typically based on Arrhenius kinetics and is modeled by a power law [48,49] of the following form

$$d^n - d_0^n = k_0 \cdot \exp\left(-\frac{E}{RT}\right) \cdot t \quad (2)$$

where $d_0$ is the initial size, $d$ is the increased size after annealing. $E$ is the activation energy for the neck growth process and $R$ is the universal gas constant. $n$ and $k_0$ are constants that are typically determined by comparison with experimental data [48,49]. It is proposed that neck growth in polymer AM samples is also characterized by a similar power law. In the present case where neck growth is considered in response to thermal annealing, $d_0$=0 since there is no necking initially. This assumption is justified because of significant filament-to-filament gap designed in the printing process. Further, past work shows that thermal penetration into previously deposited layers during the printing of a fresh layer is not strong enough to significantly increase neck size [50].

Thus, in the case of neck growth, equation (2) can be written as:

$$d^n = k_0 \cdot \exp\left(-\frac{E}{RT}\right) \cdot t \quad (3)$$

3.2.2. Heat transfer model

Total thermal resistance in the build direction is the sum of thermal resistances offered by each layer and the total contact resistance between layers [47]. Therefore, thermal conductivity ($k_z$) in the build direction is given by [47]:

$$\frac{1}{k_z} = \frac{1}{k_{layer}} + \frac{R_C}{h} \tag{4}$$

where $k_{layer}$ is the material thermal conductivity of the filament material, $R_C$ is the thermal contact resistance between the layers and $h$ is the layer height.

Thus, the baseline thermal conductivity prior to thermal annealing, $k_{z,0}$ can be written as:

$$\frac{1}{k_{z,0}} = \frac{1}{k_{layer}} + \frac{R_{C,0}}{h} \tag{5}$$

where $R_{C,0}$ is the baseline thermal contact resistance.

The increase in neck size increases the contact area between filaments, resulting in a reduction in thermal contact resistance between layers. The mathematical relationship between neck size and contact resistance is not known. In this paper, it is proposed that inter-layer thermal contact resistance in the annealed sample is related to the neck size as:

$$R_{C,a} = R_{C,0} - \beta \cdot d^m \tag{6}$$

where $\beta$ and $m$ (>1) are constants.

Equation (6) hypothesizes that a larger neck size will reduce thermal contact resistance due to the $d^m$ scaling. Further, because thermal contact resistance is likely to scale with the area of contact between filaments in adjacent layers, therefore, the value of $m$ may be expected to be close to 2, since the area of contact scales with the square of the neck size.

Using equations (4) and (6), an expression for thermal conductivity of the annealed sample may be written as:

$$\frac{1}{k_{z,a}} = \frac{1}{k_{layer}} + \frac{R_{C,0}}{h} - \frac{\beta}{h} \cdot d^m \tag{7}$$

Using equation (5), this simplifies to

$$\frac{1}{k_{z,a}} = \frac{1}{k_{z,0}} - \frac{\beta}{h} \cdot d^m \tag{8}$$

Equation (8) is a model that connects microstructure of the annealed part with its thermal conductivity. The neck size *d* in equation (8) is related to the annealing parameters *T* and *t* through the kinetic model, equation (3). Therefore, by combining the kinetic and heat transfer models, thermal conductivity of the annealed sample can be related to the annealing time (*t*) and temperature (*T*) as:

$$\frac{1}{k_{z,a}} = \frac{1}{k_{z,0}} - \frac{\beta}{h} \cdot \left(k_0 \cdot \exp\left(-\frac{E}{RT}\right) \cdot t\right)^{m/n} \tag{9}$$

Equation (9) is the key result that relates thermal conductivity enhancement with annealing time and temperature. The key assumptions behind this result include Arrhenius based neck growth kinetics, and the scaling of inter-layer thermal contact resistance with $d^m$. While equation (3) connects microstructure with process, equation (7) connects the microstructure with resulting thermal properties of the built part. In contrast with well-established experimental and theoretical work on annealing of metal parts, not much literature exists on thermal annealing of AM parts. Therefore, the validity of these assumptions needs to be established based on comparison with experimental data. Specifically, a number of parameters in the theoretical model – *m*, *n*, $\beta$, $k_0$ and *E* – must be determined by fitting experimental data with theoretical equations, and the accuracy of resulting relationships between *T*, *t*, *d* and $k_z$ must be established by comparison with experimental data. These important issues are addressed in Section 3.3.1.

Note that the model proposed in this section is not valid at very high temperatures where other physical processes, such as polymer melting become important, or at very low temperatures close to or lower than the glass transition temperature, where thermally-driven filament

deformation is no more significant. There is also an upper limit on possible thermal conductivity enhancement due to annealing, since thermal conductivity of the part clearly can not exceed that of the underlying material.

## 3.3. Results and discussion

### 3.3.1. Cross-section visualization and neck size measurement

Cross-sections of samples before and after thermal annealing are visualized and the neck size is measured using the technique discussed in section 3.1.4. Figure 3.4 shows a set of four images of cross-section images from four samples annealed at 135 °C (398 K) temperature for different times, including a baseline sample prior to annealing. Significant progression in neck size is seen as annealing time increases. This increase is central to the theoretical model for annealing-based thermal conductivity enhancement. Note that the build direction for cross-section images shown in Figure 3.4 is from bottom to top.

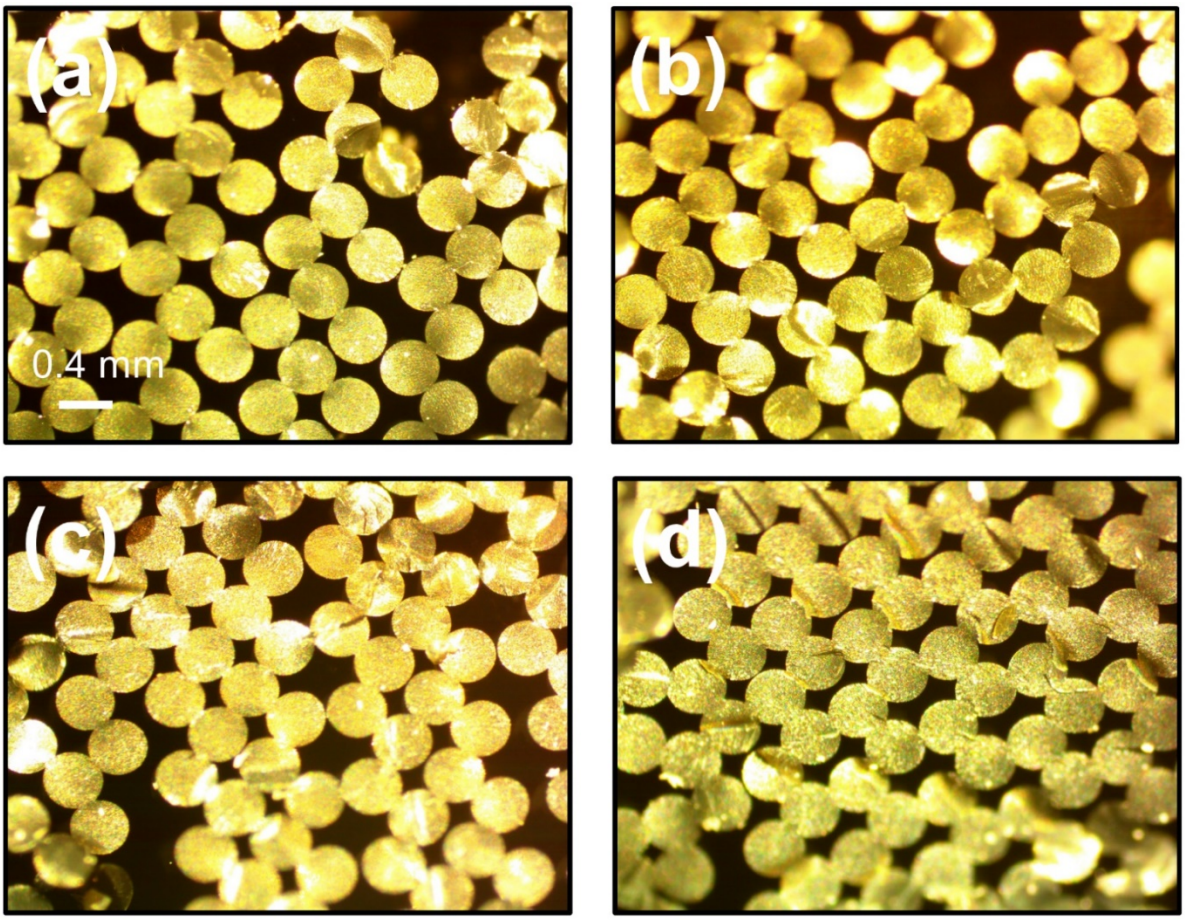


Figure 3.4 Cross-section images showing the extent of filament-to-filament necking in four samples annealed at 398 K temperature for different times. (a)-(d) show samples annealed for 12, 24, 48, and 96 hr respectively. Note that the build direction for each cross-section image is from bottom to top.

3.3.2. Parameter extraction from theoretical models

Equation (3) shows that for constant-temperature annealing experiments, the relationship between $d^n$ and *t* must be linear. Therefore, the value of *n* can be determined as that value which results in a linear $d^n$ vs. *t* plot. In order to examine this in detail, annealing experiments as described in section 3.1.2 are carried out at 398 K for 12, 24, 48 and 96 hours. In each case, the neck size *d* is determined using the process described in section 3.1.4. $d^n$ vs. *t* plots are generated for multiple values of *n*. Through least squares fitting, the most linear relationship between $d^n$

and $t$ is found to occur for a value of $n$ = 2.6. This best fit is shown in Figure 3.5, which shows an excellent linear fit between $d^{2.6}$ and $t$. The value of $n$ determined in this manner is in the same range as the power exponent for grain growth models [48, 49], even though the material systems are quite different.

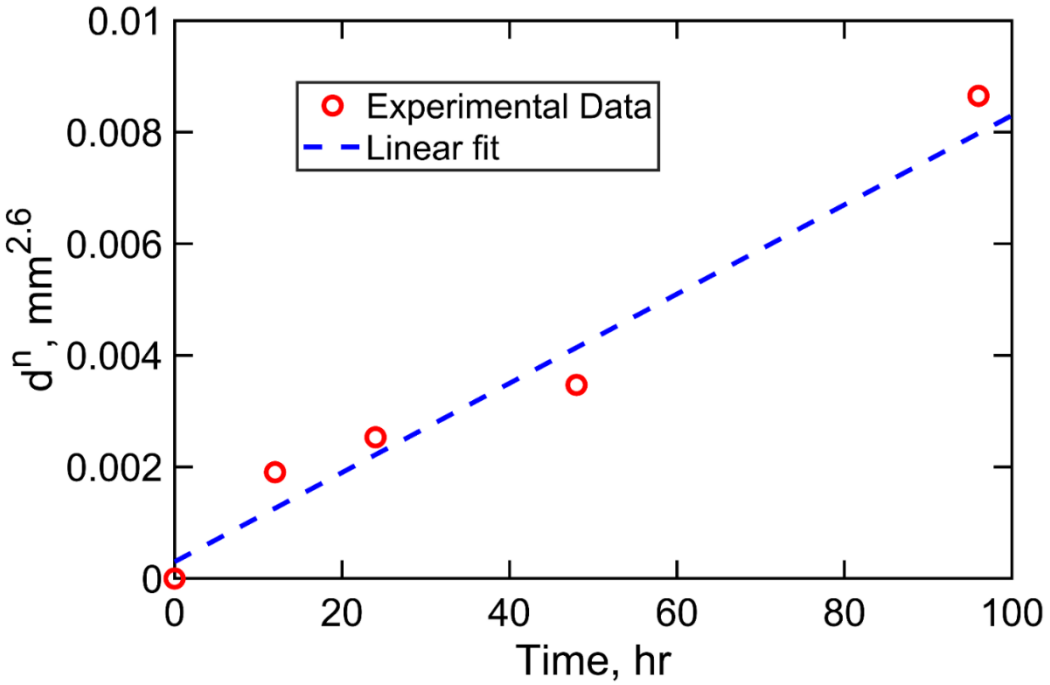


Figure 3.5 Plot of $d^n$ and $t$ for $n$=2.6, based on measurement of neck sizes of samples annealed at 398 K for different times. A value of $n$=2.6 results in the most linear fit, as predicted by the power law in the kinetic model.

Values of the other kinetic parameters – $E$ and $k_0$ – are obtained next. In order to do so, experimental data on neck size as a function of annealing temperature from experiments at constant annealing time are used. Taking logarithm of equation (3) results in:

$$ln(d) = -\frac{E}{nRT} + \frac{1}{n} \cdot \ln(k_0) + \frac{1}{n} \cdot \ln(t) \qquad (910)$$

which shows that for constant-time annealing experiments, a plot of ln($d$) vs. 1/$T$ is expected to be linear. The slope and intercept of this plot is given by $-E/nR$ and $\ln(k_0 t)/n$, respectively, from where $E$ and $k_0$ can be determined, since $n$ is already known, $d$ has been measured, and $t$ and $R$ are known constants. Figure 3.6 shows a ln($d$) vs. 1/$T$ plot based on experimental data for a constant time $t$ = 24 hours and temperatures of 378 K, 388 K, 398 K and 408 K. Figure 3.6 shows good linearity between the two. A slope of -6103.9 K and an intercept of 13.244 are obtained, based on which, the values of $E$ and $k_0$ are found to be 131.944 kJ/mol and $3.75\times10^{13}$ $mm^{-2.6}$/hr respectively.

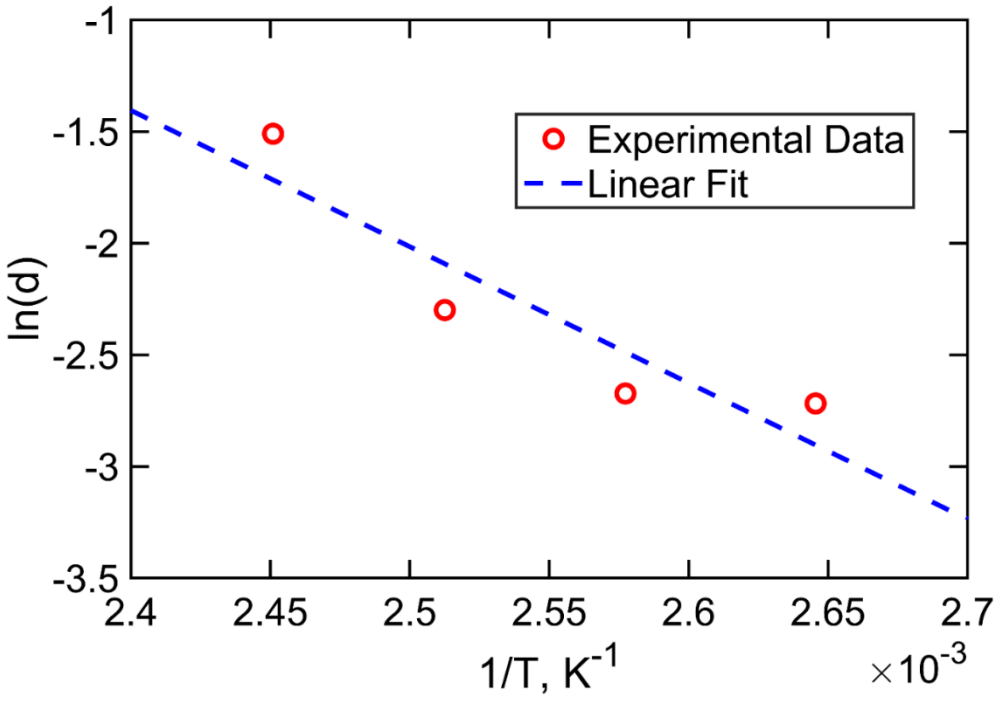


Figure 3.6 Plot of ln($d$) vs. 1/$T$ based on experimental data for a constant time $t$ = 24 hours. Slope and intercept of this plot facilitate determination of kinetics parameters $\beta$ and $E$.

Finally, the values of $m$ and $\beta$ – parameters that govern the relationship between microstructure and thermal properties – are determined by plotting $1/k_{z,0} - 1/k_{z,a}$ as a function of $d^m$. This utilizes measurements of neck size as described in section 3.1.4 and of thermal conductivity as described in section 3.1.3. Experimental data for annealing temperatures of 388 K,

398 K and 408 K at a constant annealing time of 24 hours are utilized. The value of $m$ is determined to be the value that results in linear relationship between $d^m$ and $1/k_{z,0} - 1/k_{z,a}$. Further, the slope of this relationship can be used to determine $\beta$. The best linear fit is found for a value of $m$ = 2.0, and is shown in Figure 3.7. Based on the slope of the best fit line in Figure 3.7, determined to be 91.95 K/W·m, and a layer height of $h$ = 0.4 mm based on experiments, the value of $\beta$ is calculated to be 36.78 K/W. The value of $m$=2.0 obtained from experimental data analysis is consistent with the expectation that the inter-layer contact resistance must scale with the contact area, which in turn scales with the square of the neck size, as discussed in section 3.1.2.

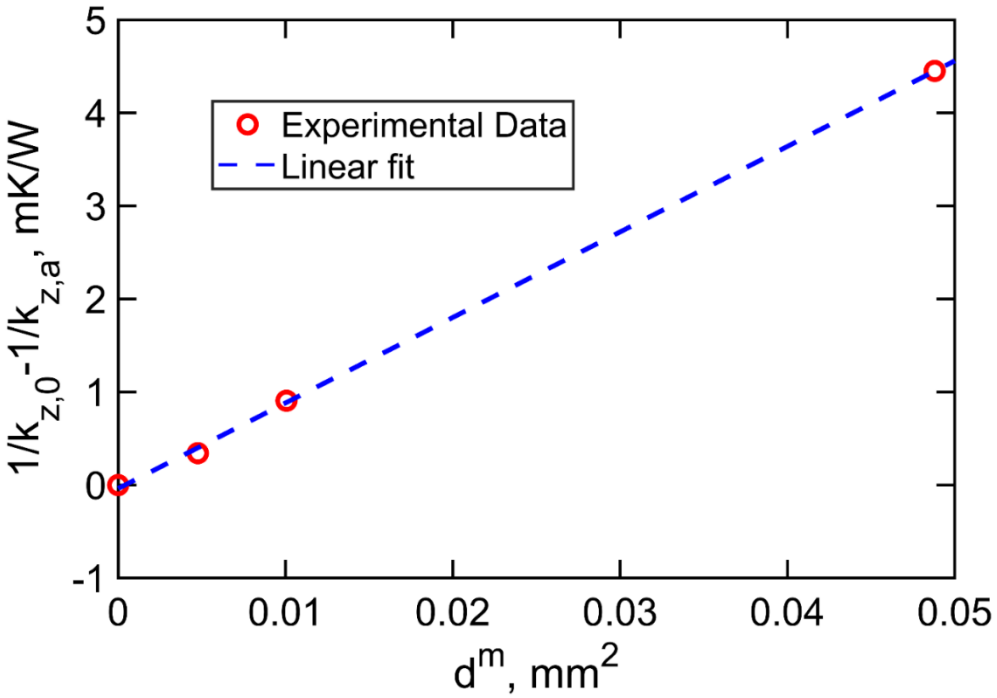


Figure 3.7 Plot of $1/k_{z,0} - 1/k_{z,a}$ as a function of $d^m$ for $m$=2.0, which results in the most linear fit, as predicted by the heat transfer model. Thermal conductivity and neck size measurements are based on experimental procedures described in section 3.1.

In this manner, experimental data at different annealing temperatures and times are utilized to validate the theoretical models and determine the key parameters involved in the models. Once these parameters are known, it is possible to theoretically predict the enhancement in thermal

conductivity for any annealing temperature and time. Note that the model parameters determined in this sub-section are specific to the filament material used here, and possibly to other process parameters as well, such as filament size, dispense temperature, as these parameters all affect the nature of bonding between adjacent filaments. Therefore, for a different material, or a different set of process parameters, these parameters may need to be determined again.

### 3.3.3. Comparison of experimental data with theoretical model

Based on model parameters determined in section 3.3.1, experimental measurements of thermal conductivity as a function of annealing temperature and time are compared with the theoretical model. Figure 3.8 plots measured post-annealing thermal conductivity as a function of annealing time for two different oven temperatures – 398 K and 408 K. At each data point shown in Figure 3.8, the sample is annealed using the process described in section 3.3.1, followed by thermal conductivity measurement as described in section 3.1.3. These data show significant enhancement in thermal conductivity with increasing time. While thermal conductivity enhancement is somewhat minor at small times, the rate of improvement goes up non-linearly at large times. As expected, thermal conductivity enhancement is greater for experiments at 408 K than at 398 K due to the higher temperature. Figure 3.8 also shows corresponding predictions of thermal conductivity enhancement based on the theoretical model, specifically equation 9, using the model parameters determined in section 3.3.1. Figure 3.8 shows that the theoretical model accurately captures the trend in experiments, for data at both annealing temperatures, with good agreement with experimental measurements.

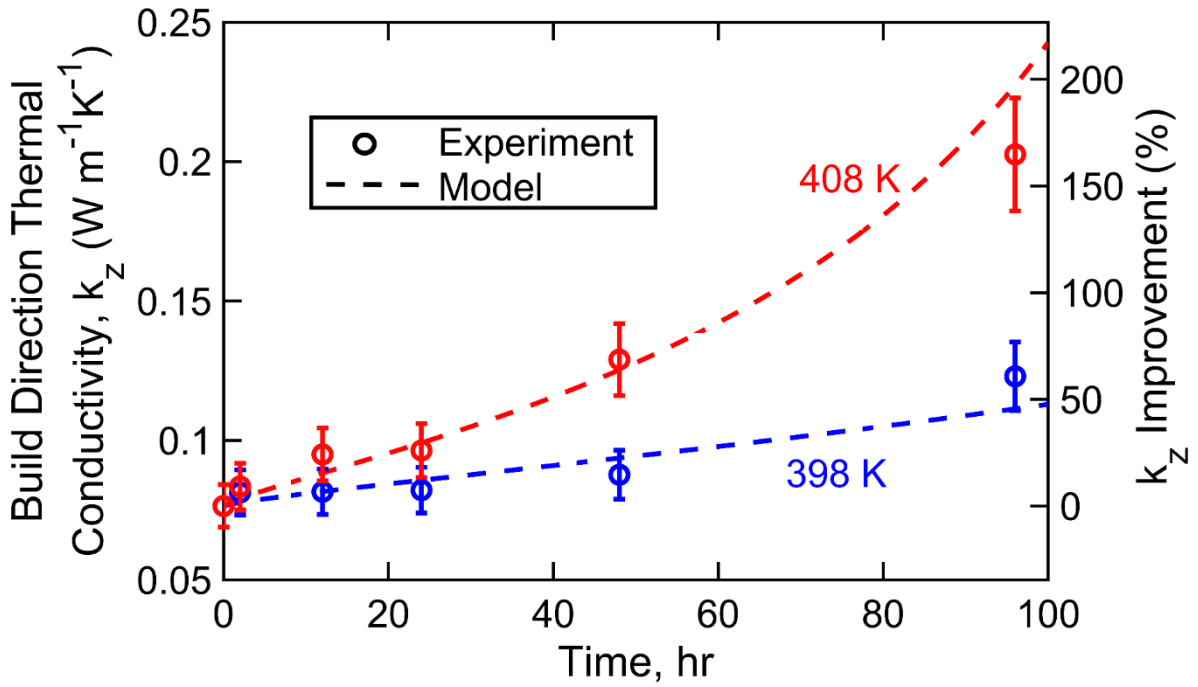


Figure 3.8 Comparison of measured thermal conductivity as a function of annealing time for two different oven temperatures – 398 K and 408 K – with prediction from the theoretical model.

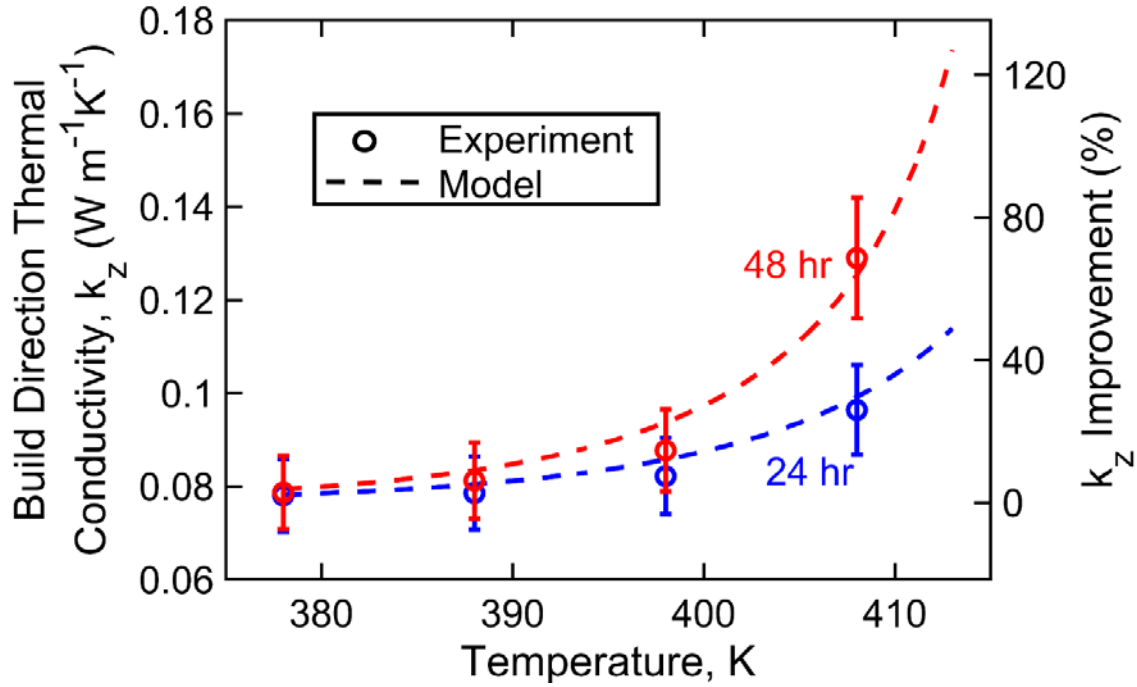


Figure 3.9 Comparison of measured thermal conductivity as a function of annealing temperature for two different anneal times – 24 hours and 48 hours – with prediction from the theoretical model.

For further comparison of experimental data with theoretical model, measured thermal conductivity values are plotted in Figure 3.9 as a function of annealing temperature for experiments carried out for the same time duration. Two sets of data – at 24 hours and 48 hours – are shown. Similar to Figure 3.8, this plot also shows increasing thermal conductivity with increasing annealing temperature, and greater thermal conductivity for the 48 hours data compared to 24 hours data, for any given annealing temperature. The gap between thermal conductivity for the two sets of data is particularly significant at high annealing temperature, such as 135 °C, showing that in order to obtain the same thermal conductivity enhancement, the annealing time can be significantly reduced by relatively small increase in annealing temperature. Theoretically, this happens because, as shown in equation (2), while dm increases linearly with t, the dependence on T is much stronger due to its occurrence in the non-linear, exponential term.

It is instructive to compare the thermal conductivity enhancement reported here with enhancement in fracture toughness reported by Hart, et al. [6] under similar annealing conditions. For example, Figure 3.8 shows over 150% enhancement in thermal conductivity for annealing at 135 °C for 96 hours. For similar conditions, Hart, et al. [6] reported around 2700% improvement in fracture toughness. As such, thermal conductivity of polymers does not vary over such a large range, as does a mechanical property such as fracture toughness. A 150% increase in thermal conductivity itself brings the value close to the baseline value of the filament material itself [51], which clearly is an upper limit for the thermal conductivity. Further, note that while the theoretical model for fracture toughness in Hart, et al. [6] predicts an exponential dependence on time, thermal conductivity is expected to increase much lesser with time, as shown in equation (9).

Uncertainty in thermal conductivity measurement is the key source of measurement uncertainty in data shown in Figures 3.7 and 3.8. Other sources of uncertainty include uncertainty in temperature measurement, sample thickness measurement, etc.

### 3.3.4. Annealing process design space

Based on the experimentally validated analytical model discussed in sections 3.3.1 and 3.3.2, the thermal design space for the annealing process can be explored in order to predict design parameters that result in desired thermal conductivity enhancement. Design of experiments based on predictions from the analytical model is particularly important because the annealing time must be minimized for increasing throughput, and also because there are several restrictions on the temperature range.

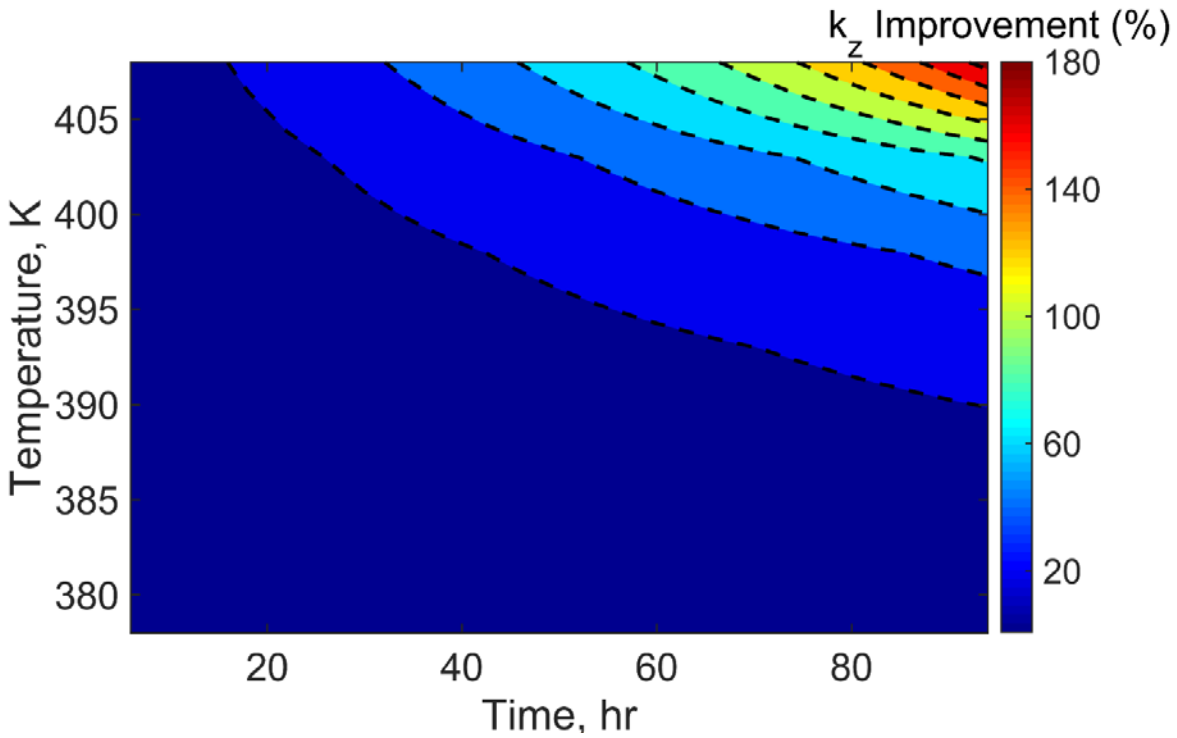


Figure 3.10 Colorplot of predicted post-annealing thermal conductivity in the (T,t) space.

The two key process parameters of relevance for thermal annealing include annealing temperature T and annealing time t. Figure 3.10 presents a colorplot of thermal conductivity

enhancement as a function of T and t. This plot offers several interesting insights. In general, the higher the value of T and/or t, the greater is the thermal conductivity enhancement. Specifically, the dependence on T is highly non-linear, with negligible improvement at low temperatures, regardless of the annealing time, and dramatically greater thermal conductivity improvement at greater times. There exist a number of (T,t) pairs that lead to the same thermal conductivity enhancement. As an example, Figure 3.10 shows multiple curves along each of which, all (T,t) points result in the same thermal conductivity enhancement. This indicates that there are several process design choices for the same eventual outcome. However, this is constrained by several other considerations. For example, while increasing temperature does offer the convenience of reduced annealing time for achieving the same outcome in terms of thermal conductivity enhancement, too high a temperature results in softening and mechanical distortion of the sample. On the other hand, annealing at low temperature for a very long time is unrealistic as it reduces throughput. Further, as discussed in a subsequent section, a sample takes some time to equilibrate to the oven temperature after being inserted, which could be several hours depending on the sample size. In between all of these conflicting considerations, one must determine an optimal strategy for obtaining the desired goal.

### 3.3.5. Non-isothermal annealing

The analytical model presented in Section 3.2 assumes that the sample anneals in isothermal conditions corresponding to the oven temperature. However, depending on the size of the sample, it is possible that the sample might take a significant amount of time to reach close to the oven temperature. If this time is comparable to the total anneal time, then annealing occurs in a non-isothermal manner, wherein the sample temperature itself changes with time. From a heat transfer perspective, the time taken for the sample to reach close to the oven temperature depends on the

thermal mass of the sample and rate of convective heat transfer from the oven ambient to the sample. When the Biot number is reasonably small, the sample may be assumed to be a lumped thermal mass [52], so that the thermal time constant is given by $\frac{\rho C_p V}{hA}$, where $\rho$ , $C_p$, $V$, h, and A are density, specific heat, volume, convective heat transfer co-efficient and surface area respectively. Based on the geometry of samples used in these experiments, and assuming free convection conditions inside the oven, the Biot number for present experiments is found to be 1.2-1.8, which is quite large. As a result, a simple lumped thermal mass assumption is not valid, and the thermal history of the sample during oven acclimatization must be determined through alternative approaches such as a finite-element simulation. Figure 3.11 plots temperature as a function of time for two samples of different sizes during oven acclimatization, starting from room temperature and up to the oven temperature of 135 °C. Figure 3.11 shows that the time taken for the sample to reach oven temperature is a function of the sample size. Isothermal conditions during annealing may not be assumed for relatively large samples.

The analytical model for thermal conductivity enhancement presented in section 3.1 can be extended to account for non-isothermal conditions. The neck size d, which equation (3) determines based on a constant temperature assumption must now consider changes in temperature with time, and therefore,

$$d^n = k_0 \cdot \int_0^t exp\left(-\frac{E}{RT(\tau)}\right) d\tau \tag{11}$$

so that the total enhancement in thermal conductivity over time t is given by a generalization of equation (9)

$$\frac{1}{k_{z,a}} = \frac{1}{k_{z,0}} - \frac{\beta}{h} \cdot \left( k_0 \cdot \int_0^t exp\left(-\frac{E}{RT(\tau)}\right) d\tau \right)^{m/n} \tag{12}$$

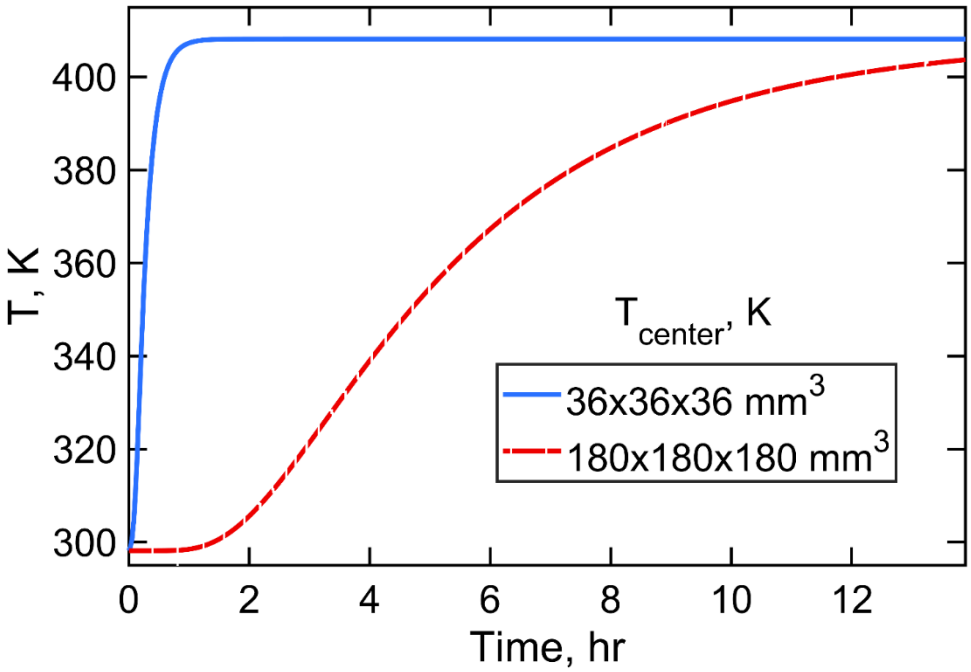


Figure 3.11 Temperature as a function of time after inserting a sample in an oven set at 135 oC for annealing. Plots are shown for two samples of different sizes.

# CHAPTER 4

## Measurement and modeling of filament temperature distribution in the standoff gap between nozzle and bed in polymer-based additive manufacturing

**Published as:** Prajapati, H., Ravoori, D., Jain, A., 'Measurement and modeling of filament temperature distribution in the standoff gap between nozzle and bed in polymer-based additive manufacturing,' *Additive Manufacturing*, 24, pp. 224-231, 2018.

## Introduction

Dispensing of a polymer filament above its glass transition temperature is a critical step in several polymer-based additive manufacturing techniques. While the nozzle assembly heats up the filament prior to dispense, it is important to minimize cooling down of the filament in the standoff distance between the nozzle tip and bed. While heat transfer processes within the nozzle assembly, such as filament melting, and on the bed, such as thermally-driven filament-to-filament adhesion, have been well studied, there is a lack of work on heat transfer in the filament in the standoff region. This paper presents infrared thermography based measurement of temperature distribution in the filament in the standoff region, and an analytical model for heat transfer in this region. The analytical model based on a balance between thermal advection and convective/radiative heat loss predicts an exponentially decaying temperature distribution, the nature of which is governed by the characteristic length, a parameter that combines multiple process parameters such as mass flowrate, filament diameter, heat capacity and cooling conditions. Experimental data in a wide range of process parameters are found to be in very good agreement with the analytical model. The thermal design space for ensuring minimal temperature drop in the standoff region is explored based on the analytical model. Experimental data and theoretical modeling presented here improve our fundamental understanding of heat transfer in polymer additive manufacturing, and may contribute towards design tools for thermal optimization of polymer based additive manufacturing processes.

### 4.1. Experiments

Experiments were carried out to quantitatively measure the temperature distribution in the filament in the standoff region after being extruded from the nozzle tip through infrared

thermography. A custom-built platform for filament dispensing with controlled process parameters and optical access for infrared thermography was designed and built for this purpose.

### 4.1.1. Extruder arrangement

Commercially available polymer AM platforms do not provide sufficient flexibility to vary process parameters of interest in this work and also do not offer good optical access to the standoff region. As a result, an in-house polymer extruder and dispenser setup was designed and assembled to facilitate careful variation and measurement of various parameters such as filament speed, nozzle diameter, etc. while also offering an optical access for an infrared camera to measure temperature variation along the length of the extruded material. Figure 4.1(a) presents a schematic of the experimental setup, showing the key components, including a control circuit, stepper motor, and heater-nozzle assembly. Stepper motor speed and heater block temperature were controlled by an Arduino Mega 2560 circuit board running a RAMPS A4988 stepper motor driver using Repetier-Host V2.0.5 software. The filament was fed through a NEMA 17 stepper motor to the Aluminum heater block. Calibration for the stepper motor was entered in the motor firmware and verified through test runs. 1.75mm diameter Acrylonitrile butadiene styrene (ABS) Black filament material from Makerbot was used in all experiments. Figure 4.1(b) shows a zoom-in image of the active area in the experiment, including the polymer dispensing nozzle, IR camera lens and a cooling fan in the background used in some of the experiments discussed in section 4.3.

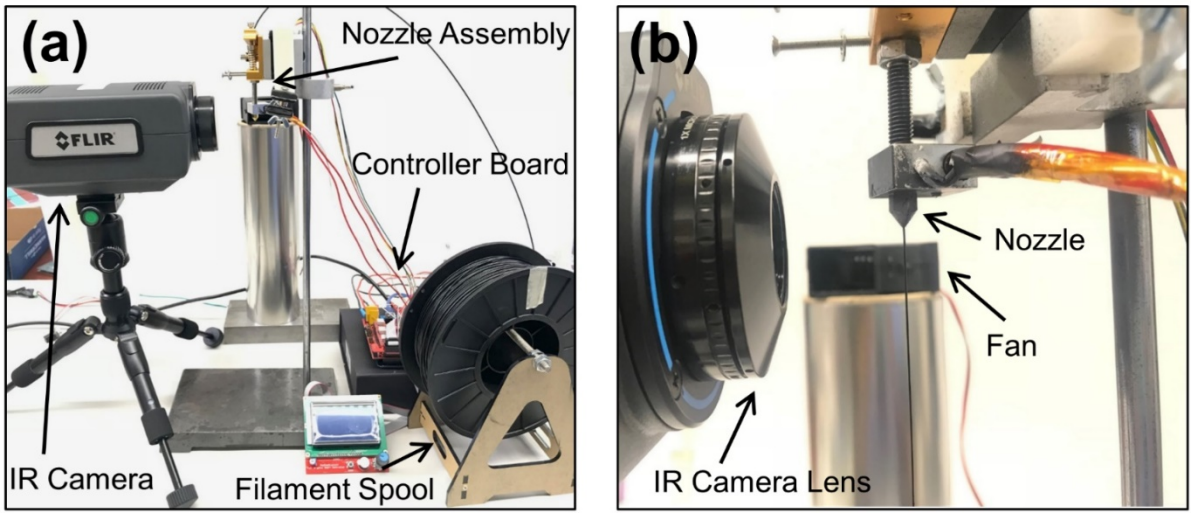


Figure 4.1 (a) Picture of the experimental setup showing the custom-built extruder assembly and infrared camera; (b) Zoom-in picture showing the nozzle tip and extruding filament.

There is no print bed under the filament being dispensed. This is justified because the print bed temperature is not expected to have a significant impact of filament temperature distribution in the standoff region due to the large value of the Peclet number [52], which is the ratio of thermal advection downstream to thermal diffusion upstream. This is discussed further in section 4.2. Separate experiments were carried out in which temperature distribution in the standoff region was measured in the presence of a print bed underneath that was maintained at a number of different experiments. These data confirm minimal effect of print bed temperature on measured filament temperature distribution.

As shown in Figures 4.1(a) and 4.1(b), a FLIR A6703sc InSb infrared camera was positioned at a fixed distance from the nozzle tip to capture temperature distribution along the length of the filament being dispensed. The spatial resolution of these measurements is around 15 μm. Calibration of the IR camera is described next.

4.1.2. Calibration for infrared thermography

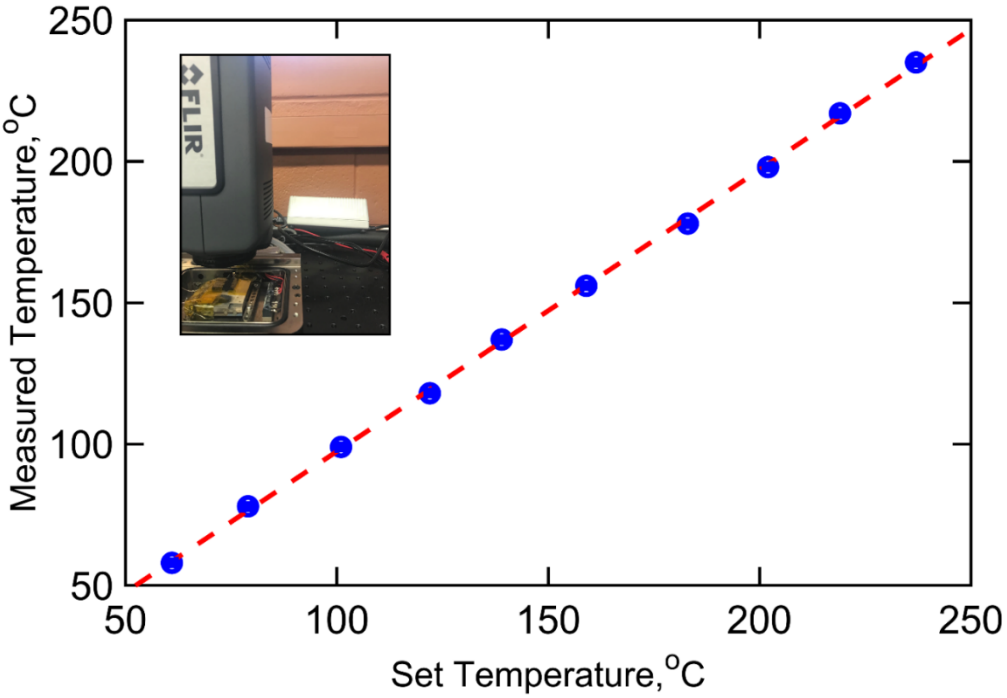


Figure 4.2 Calibration plot for infrared thermography based on comparison of temperature measured by infrared camera with thermocouple measurement between room temperature and 230 °C. Inset shows a picture of the calibration experiment.

While an infrared camera offers a convenient, non-invasive approach for temperature measurement of the entire filament length, careful calibration is needed to ensure accuracy. Experiments are carried out in advance to determine the emissivity of the polymer material and ensure that temperature measurement from the IR camera match well with an independent measurement. For this purpose, a small square sample is printed from the same polymer material that is used for extrusion experiments. This sample is placed on an Instec HCS662V constant temperature stage. Temperature of the top surface of the sample is measured by the infrared camera as well as a T-type thermocouple, monitored through a NI-9213 DAQ thermocouple module and LabView software. Temperature of the thermal stage is varied from room temperature to 230 °C at 20 °C intervals. Once sufficient time has elapsed at each temperature point to reach steady state,

temperature of the top surface of the sample is measured by the infrared camera and compared with thermocouple measurements. The experimental setup is shown in the inset of Figure 4.2.

### 4.1.3. Experiments

Once the various components of the experiment are set up and calibration is completed, a number of experiments are carried out to measure temperature distribution along the filament length and understand the effect of various process parameters on the temperature distribution. Filament dispense speed is varied between 2.2 mm/s and 20.2 mm/s by changing the speed of the stepper motor. At each stepper motor setting, the filament dispense speed is determined by measuring the filament length dispensed in a specific time interval. Diameter of the extruded filament is also measured through a micrometer. Nozzles of two different diameters – 0.4 mm and 0.6 mm – are used in this work. In order to investigate the effect of convective cooling, air flow at different volumetric flow rates ranging from $12.0\times10^5$ $m^3/s$ to $22.6\times10^5$ $m^3/s$ is impinged on the filament from a small fan, which can be seen in the background in Figure 4.1(b).

Heat capacity of the filament material – an important parameter for the theoretical model – is measured using a Differential Scanning Calorimeter (DSC) to be 1708 J/kgK. This value is found to vary by less than 3% in the temperature range of 180-200 °C. Further, mass density of the extruded material is determined to be 877 $kg/m^3$ by measuring the volume and weight of an extruded filament in a test run.

Key results obtained from experiments discussed in this section are presented in Section 4.3.

## 4.2. Mathematical Modeling

A mathematical model is developed for heat transfer in the filament in the standoff region in order to derive an expression for temperature distribution in the filament. Figure 1.2(a) shows a schematic of this process. The filament exits the nozzle tip located at $x$=0 at a temperature $T_0$ with a mass flowrate of $\dot{m}$ , and after traveling through the standoff distance, is deposited on the bed at $x=L$. Filament temperature at $x=L$, where the filament reaches the bed is of particular interest. The ambient temperature is assumed to be $T_\infty$. Convective cooling between the filament and the ambient is assumed, with a convective heat transfer coefficient $h_c$. Radiative heat transfer may also occur in the standoff region.

Temperature of the print bed under the filament being dispensed is not modeled, because in this case, advective heat transfer along the filament downstream is expected to dominate over thermal diffusion from the print bed into the filament in the standoff region. The ratio of the magnitude of these two phenomena, called the Peclet number [52] is estimated to be very large, around 200 due to the relatively large value of filament speed and low thermal diffusivity of the filament material. This indicates that the filament temperature distribution in the standoff region is largely unaffected by thermal diffusion from the print bed.

Temperature distribution within the filament, $T(x)$ between $x=0$ and $x=L$ is assumed to be in steady state. This is expected to be a reasonable assumption beyond the short time during which the filament first leaves the nozzle and travels through the standoff distance. Once filament motion is established within the standoff region, temperature at any location $x$ is expected to be independent of time. The validity of this assumption is confirmed through measurements discussed in Section 4.3.5. Further, temperature is assumed to vary only in the $x$ direction, and not within the cross-section of the filament. Thermal uniformity in the transverse direction is justified by the very

small value of the Biot number in the radial direction [52], estimated to be around 0.02 due to the very small size of the filament. An Eulerian approach is followed in order to determine an expression for $T(x)$. Energy conservation is considered in an infinitesimal element of thickness $dx$ located at distance $x$ from the nozzle tip during steady state, as shown in Figure 4.1(b). Thermal energy is advected into this element at the top face along with the extruding filament material, and advected out at the bottom face, as shown in the elemental energy balance schematic in Figure 4.1(b). These energy fluxes can be determined through heat capacity of the filament material and the local temperature. In addition, the element loses heat from its peripheral surface area due to convection, radiation or both. Axial thermal conduction effects are neglected due to the relatively large speed of the filament. As a result, the overall energy balance for the element is given by

$$\dot{m}C_pT = \dot{m}C_p\left[T + \frac{\partial T}{\partial x}dx\right] + h_cP[T - T_\infty]dx + \varepsilon\sigma P(T^4 - T_r^4)dx \quad (1)$$

where $P$ is the filament perimeter, assumed not to change along the filament. $C_p$ is the heat capacity of the filament material. $\dot{m}$ is the mass flowrate, given by $\dot{m} = \rho AV$, where $\rho$ is filament density, $A$ is the cross section area and $V$ is the filament speed. $\varepsilon$ and $\sigma$ are the emissivity of the filament and Stefan Boltzmann constant respectively. $T_r$ is the representative temperature of the surroundings to which the element radiates. $T_r$ is a combination of the temperatures of surfaces in the vicinity of the element, such as the nozzle tip, bed, etc. Equation (1) can be simplified to

$$\frac{\partial T}{\partial x} = -\frac{h_cP}{\dot{m}C_p}(T - T_\infty) - \frac{\varepsilon\sigma P}{\dot{m}C_p}(T^4 - T_\infty^4) \quad (2)$$

which is a non-linear ordinary differential equation for determining the temperature distribution in the filament. The initial condition at the nozzle tip, $x$=0 is simply $T$=$T_0$.

An explicit analytical solution for equation (2) is difficult to determine due to the non-linear term. While it can be solved numerically based on the explicit definition of the derivative of temperature in equation (2), an analytical solution is sought by linearizing the radiative term in equation (2), as is usually done, by writing an approximate radiative heat transfer coefficient, $h_r$ given by [52]

$$h_r = \varepsilon\sigma(T_{eff}^2 + T_r^2)\,(T_{eff} + T_r) \tag{3}$$

where $T_{eff}$ is the effective filament temperature, which can be approximated with the average filament temperature. Based on this approximation, equation (2) can be re-written as

$$\frac{\partial T}{\partial x} = -\frac{h_{eff}P}{\dot{m}C_p}(T - T_\infty) \tag{4}$$

where $h_{eff}$= $h_c$+ $h_r$ is the effective heat transfer coefficient given by the sum of convective and radiative heat transfer coefficients. Based on this simplification, an expression for the temperature distribution in the filament is found to be

$$\theta = \frac{T - T_\infty}{T_0 - T_\infty} = \exp\left(-\frac{x}{x_0}\right) \tag{5}$$

where the characteristic length $x_0$ is given by

$$x_0 = \frac{\dot{m}C_p}{h_{eff}P} \tag{6}$$

This completes the derivation for the temperature distribution in the filament. Equation (5) shows that filament temperature reduces exponentially with distance away from the nozzle, and the nature of the exponential decay is governed by the characteristic length $x_0$, which represents the distance by which the temperature has decayed by 1/e=0.368. Filament temperature at the end of the standoff region can be found by putting $x=L$ in equation (5).

The treatment above assumes that thermophysical properties of the filament, such as heat capacity and density do not change appreciably with temperature. This is a reasonable assumption due to the narrow temperature range in a well-designed stand-off gap.

Note that equation (5) predicts two very different regimes of the temperature field depending on the value of the characteristic length $x_0$. When $x_0$ is much larger than the standoff distance $L$, equation (5) shows that $\theta$ is close to 1, i.e., there is negligible temperature drop in the filament, which reaches the bed at roughly the same temperature as the nozzle tip. In the other extreme, when $x_0$<<L, equation (5) shows that $\theta$ is close to 0, i.e., the filament cools down to the ambient temperature, which is undesirable for polymer additive manufacturing. These regimes are investigated further, and $x_0$ is calculated for typical values of the underlying parameters relevant for polymer AM in section 4.3.

In general, both convection and radiation may be important heat loss mechanisms. The magnitude of these components can be estimated through an approximate computation of radiative and convective heat fluxes. If under a given set of experimental conditions, radiation is not significant, then equation (5) will remain a valid solution with $h_r$=0. In conditions where radiation is expected to be important, either equation (5) can be solved numerically, or, as an approximation, the radiative heat transfer coefficient $h_r$ can be computed from equation (3), so that the solution is given by equation (5), with $h_{eff}=h+h_r$. In general, modeling of radiative heat transfer is quite

complicated, particularly in this case, due to the presence of a surface hotter than the filament (nozzle) as well as one that is cooler than the filament (platform bed).

## 4.3. Results and discussion

### 4.3.1. Infrared thermography calibration

Temperature of a small part printed with the same filament material used in this work is measured by the infrared camera at a number of different temperatures following the procedure discussed in section 4.1. Figure 4.2 plots the temperature measured by the infrared camera against the temperature measured by a thermocouple located next to the point of infrared temperature measurement, while the entire setup is mounted on a temperature-controlled stage. Figure 4.2 shows that over the entire measurement range, temperature measured through infrared thermography is close to the temperature measured by the thermocouple. All measurement points lie very close to the ideal 45° line on which the infrared measured temperature is equal to the set temperature. This establishes the accuracy of the infrared based temperature measurement method. The emissivity of the filament material is determined to be 0.92 through this calibration and used throughout this work.

### 4.3.2. Filament temperature measurement and comparison with analytical model

Infrared thermography enables non-invasive measurement of temperature distribution along the entire standoff region simultaneously. This is carried out for a number of different process parameters in order to understand the effect of these parameters on the temperature distribution and to compare against the analytical model.

In the first set of experiments, the filament temperature distribution is measured at five different filament speeds. Measurements are carried out for 0.4 mm and 0.6 mm nozzle diameters, which are most commonly used for polymer-based additive manufacturing. The nozzle temperature is maintained at 230 °C. No active cooling is provided, as is typical of polymer AM processes. Figures 4.3(a) and 4.3(b) summarize these data by plotting the measured filament temperature as a function of *x* for multiple extruder speeds for 0.4 mm and 0.6 mm diameter nozzles respectively. The extruder speeds listed in these Figures are different for different diameter nozzles. These are values measured for five available motor speed settings in the experimental setup. In each case, filament temperature drops as *x* increases, which is expected due to increased convective heat loss along the filament length. Further, filament temperature also reduces as the filament speed goes down, which is also expected due to the reduced advection of thermal energy at lower filament speeds.

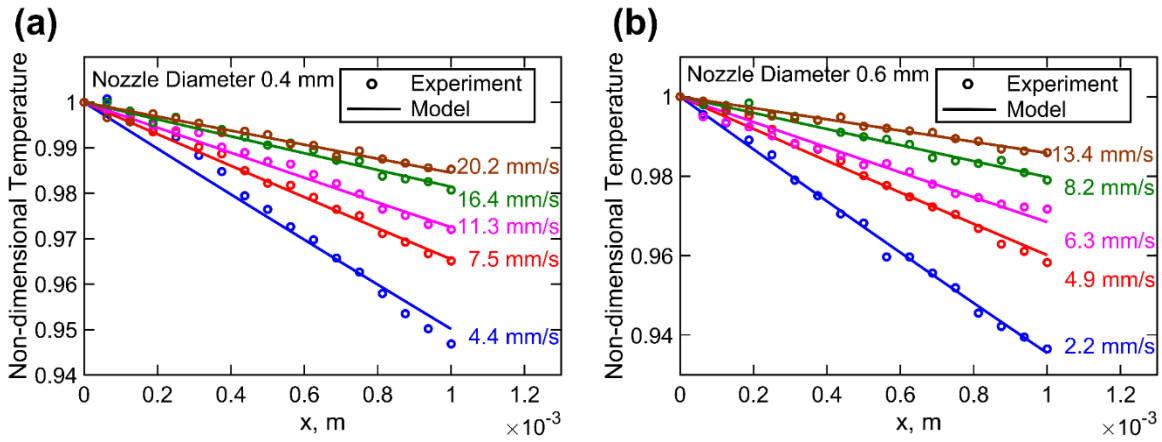


Figure 4.3 Comparison of measured temperature distribution in the standoff region as a function of *x* with prediction from theoretical model for multiple filament speeds. (a)-(b) present this comparison for 0.4 mm and 0.6 mm nozzle diameters.

Figures 4.3(a) and 4.3(b) also plot the temperature distribution predicted by the analytical model given by equation (5). Insets in each figure show the distribution at low values of *x*. There is very good agreement between the experimental data and analytical model over a broad range of

parameters. For each nozzle, as the filament speed increases, there is greater amount of heat advected into any point in the filament in the standoff region, resulting in lower and lower temperature drop in the standoff region. This is the desired regime of operation for a polymer AM process that corresponds to a large value of the characteristic length $x_0$. Note that the heat transfer coefficients for the theoretical model plots in Figure 4.3 are in the 20-40 W/m$^2$K range. This is somewhat greater than values for free convection heat transfer [52] because of two possible reasons. Firstly, the downwards motion of the filament in the stand-off region relative to the ambient air may result in some air flow, and hence, enhanced convection heat transfer. Secondly, the measured heat transfer coefficient includes contributions from radiative heat transfer, which may also raise the value of the heat transfer coefficient above those expected for free convection alone.

Note that the perimeter $P$ in equation (5) for the analytical model curves in Figure 4.3 is computed based on the actual diameter of the extruded filament, and not the nozzle diameter, due to the well-known phenomenon of polymer swelling in nozzle based extrusion [53]. The perimeter is assumed to stay constant throughout the standoff region, which is verified through measurement of the diameter of the extruded filament at a number of axial locations.

Note that the axial coordinate $x$ in these measurements and calculations varies over a much larger range than the typical standoff distance, which is usually less than 1 mm. This is done in order to expand the range of the characteristic length $x_0$ and facilitate investigation of both low $x_0$ and large $x_0$ regimes.

Further, note that in Figure 4.3 as well as subsequent figures, temperature is plotted in the non-dimensional form as given by equation (5). This ensures consistency of results for different values of nozzle and ambient temperatures. As an example, for nozzle and ambient temperatures

of 200 °C and 25 °C respectively, a range of 0.05 on the *y* axis in Figure 4.3 corresponds to a temperature drop of 8.75 °C.

The effect of active cooling of the filament during extrusion is considered next. A set of experiments is carried out where the filament is cooled with impinging air flow from a fan at different speeds. As the air speed increases, greater convective heat transfer, and therefore, a greater value of $h_c$ is expected. This is expected to push the filament into the small $x_0$ regime, where convective heat loss dominates and results in significant temperature drop across the standoff region. Figures 4.4(a) and 4.4(b) plot temperature as a function of *x* for a number of cooling conditions at two different filament speeds for a 0.4 mm diameter nozzle. Similar data are plotted

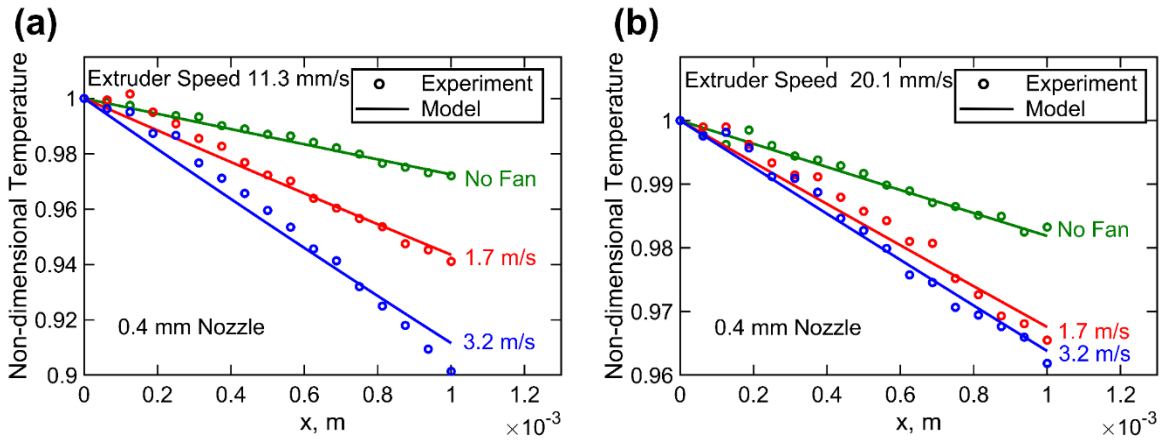


Figure 4.4 Comparison of measured temperature distribution in the standoff region as a function of *x* with prediction from theoretical model for three different cooling conditions. (a) and (b) present this comparison for two different filament speeds. The nozzle diameter is 0.4 mm in both cases.

for a 0.6 mm diameter nozzle in Figures 4.5(a) and 4.5(b). Data show, as expected, greater temperature drop as more and more cooling is provided. There is good agreement between experimental data and the predicted thermal behavior based on the theoretical model. In Figure 4.4(b), experimental data and model for the two forced cooling cases are very close to each other, which is likely because the high filament speed in this case results in reduced sensitivity on flow

speed for forced convection cooling. Clearly, as shown in Figures 4.4 and 4.5, active cooling of the filament in the standoff region is undesirable, as it leads to reduced filament temperature when it reaches the bed. Some cooling, however, is always expected even in the absence of forced air flow due to free convection heat transfer.

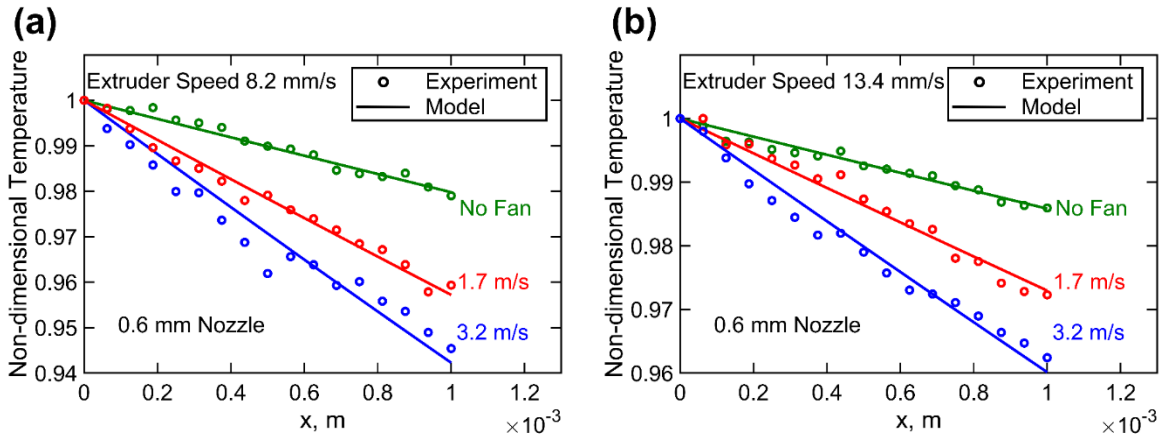


Figure 4.5 Comparison of measured temperature distribution in the standoff region as a function of *x* with prediction from theoretical model for three different cooling conditions. (a) and (b) present this comparison for two different filament speeds. The nozzle diameter is 0.6 mm in both cases.

Finally, experiments are carried out for studying the effect of the nozzle diameter on thermal characteristics of the filament in the standoff region. Nozzles of two different outlet diameters are used to dispense the filament at two different motor speeds, and temperature field is measured in each case. Figure 4.6 presents these experimental measurements as a function of *x*, as well as the corresponding analytical model curves. As with previous figures, there is very good agreement between experimental data and analytical model for a number of nozzle diameters. As the nozzle diameter increases, Figure 4.6 shows lower reduction in temperature at a larger nozzle diameter, which occurs due to increased advection of heat along with the dispensed filament. This is consistent with the definition of the characteristic length in equation (6), which shows that for the same filament speed, characteristic length increases with increasing nozzle diameter, thereby resulting in reduced temperature drop across the standoff region. This Figure also shows that the

larger the filament speed, the lower is the temperature drop, which is again consistent with the theoretical result. Note that an advantage of a larger nozzle is the reduced pumping work needed to push the filament through the nozzle.

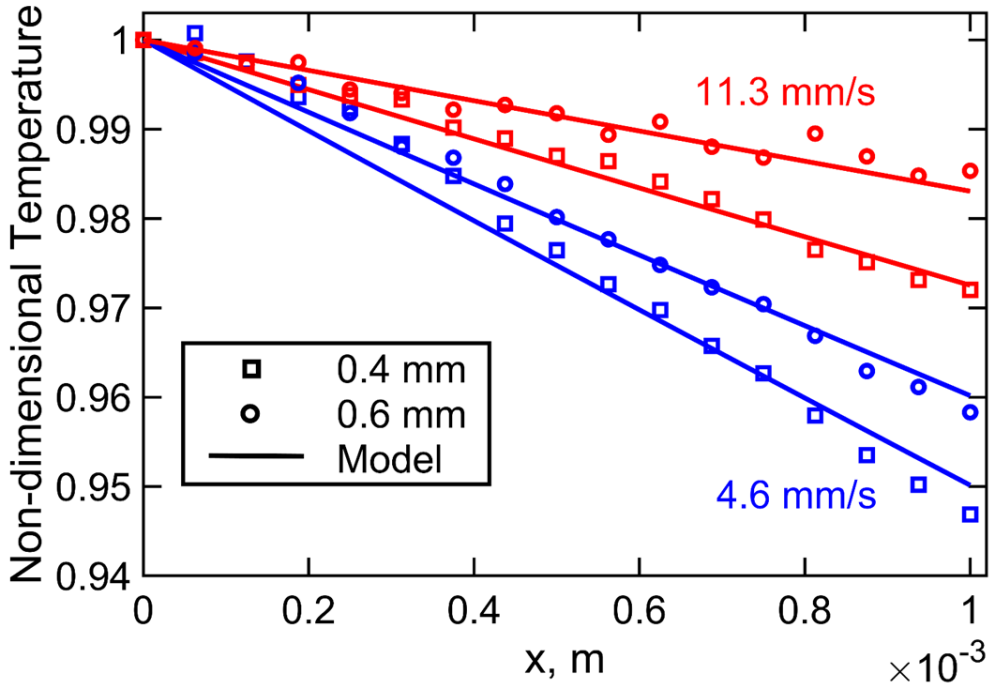


Figure 4.6 Comparison of measured temperature distribution in the standoff region as a function of x with prediction from theoretical model for two different nozzle diameters.

Figures 4.3-4.6 demonstrate the quantitative agreement between experimental data and the analytical model derived in section 4.1. This validates the analytical model, and establishes it as a useful tool for thermal design of the extrusion process. As shown in these measurements, the desired effect of minimum temperature drop in the standoff region can be achieved by a combination of large mass flowrate, large heat capacity, low filament diameter and minimum convective cooling. Some of these requirements present trade-offs and challenges with respect to other considerations. For example, a large mass flowrate and low filament diameter requires very large pressure in the nozzle assembly. Reduced filament diameter may also affect throughput

because the extruder will need to make passes to cover the same area, although, it may improve spatial resolution of the print.

4.3.3. Thermal regimes based on characteristic length

Equation (5) shows that the temperature in the filament decays exponentially as distance from the nozzle tip increases. Specifically, filament temperature at the end of the standoff region, $x=L$, a key parameter that ultimately affects bond quality between adjacent filaments is given by

$$\theta_L = \frac{T(L) - T_\infty}{T_0 - T_\infty} = \exp\left(-\frac{L}{x_0}\right) \quad (7)$$

The characteristic length, $x_0$, given by equation (6) is a key parameter that governs the temperature distribution. $x_0$ represents the balance between two processes – heat advection due to material flow and heat loss from the periphery of the filament. Based on the value of $x_0$ relative to $L$, there exist two distinct regimes with very different nature of temperature decay. When $x_0/L$ is very large, heat advection is much larger than heat loss, due to the dominance of mass flowrate and heat capacity over convective/radiative heat transfer coefficient and perimeter. In this regime, sufficiently large amount of heat continues to enter into the filament region, due to which, the temperature of the filament does not decay much through the filament length. This is also seen mathematically from equation (5) that shows that $\theta$ tends to 1 when $x_0/L$ is large. This regime can be interpreted as being an advection-dominated regime. On the other hand, when $x_0/L$ is small, there is relatively greater rate of heat loss than advection, and therefore, most of the filament cools down to the ambient temperature. The low $x_0$ regime is convection-dominated, wherein equation (5) shows that $\theta$ tends to 0 when $x_0/L$ is small.

Clearly, an effective dispensing process for additive manufacturing must be in the advection-dominated, large $x_0/L$ regime, which can be ensured through a large filament mass flowrate, large heat capacity filament material, small filament radius and low rate of cooling. By doing so, it can be ensured that the filament is dispensed on the bed at about the same temperature as the nozzle tip. Some of these considerations present significant challenges in the operation of the nozzle assembly. For example, having to simultaneously ensure large mass flowrate and small filament radius will require very large filament speed.

For any practical polymer additive manufacturing process, equation (6) can be used to determine the value of $x_0$ and therefore determine which regime the process lies in. As an illustration, for a 0.6 mm diameter nozzle extruding ABS ($\rho$=877 kg/m$^3$, $C_p$=1708 J/kgK) at 20 mm/s, $x_0$ is found to be 0.14 m, which is at least two orders of magnitude larger than typical standoff distance (less than 1 mm). This indicates that heat transfer in a typical polymer printing process is advection dominated. Assuming nozzle tip temperature of 200 °C, ambient temperature of 25 °C and a standoff distance of 0.5 mm, temperature at the end of the standoff region is found to be 199.4 °C, indicating negligible temperature drop in the standoff region under this set of parameters. If the nozzle diameter is changed to 0.1 mm, $x_0$ is now found to be 0.023 m, resulting in a lower temperature of 196.2 °C at the end of the standoff region due to reduced dominance of advection. Note that these parameters have been chosen as an illustration. These parameters can vary over a broad range of polymer AM processes, and the model is capable of thermally characterizing the process, given the values of these parameters.

4.3.4. Design space exploration with analytical model

The analytical heat transfer model presented in section 4.1,and validated through experimental measurements can be used for design space exploration. Specifically, the range of various process parameters that ensure the thermal objective of minimum temperature drop in the standoff region can be determined based on the experimentally validated model. Figure 4.7(a) plots temperature at the end of the standoff region as a function of mass flowrate. The standoff region is assumed to be 0.5 mm long. 0.4 mm diameter nozzle is assumed. Heat transfer coefficient is

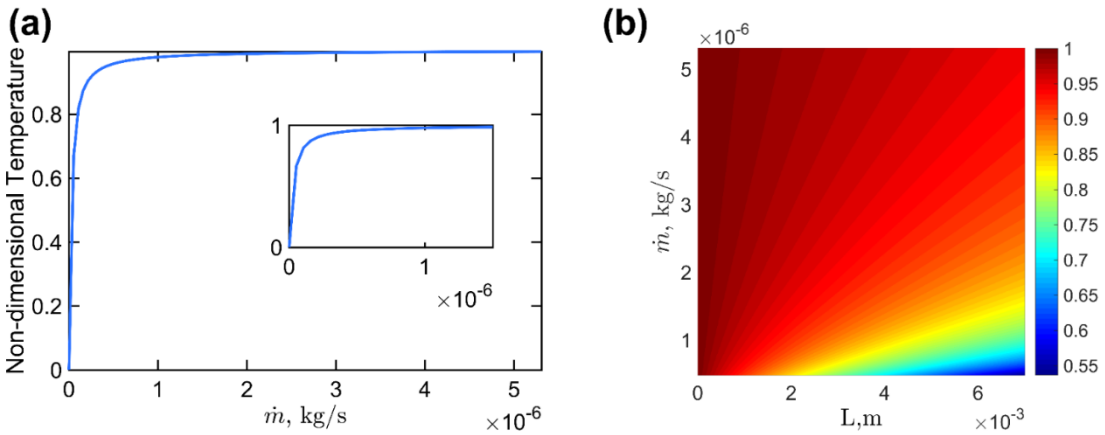


Figure 4.7 (a) Theoretically predicted temperature rise at the end of the standoff region as a function of mass flowrate, with all other parameters held constant. (b) Colormap showing the variation of theoretically predicted temperature rise at the end of the standoff region as a function of standoff distance and mass flowrate.

taken to be 31 W/m$^2$K. Figure 4.7(a) shows that temperature drop across the standoff region decreases as the extruder speed goes up. There is a certain threshold value of the mass flowrate that will meet a given specification of the maximum acceptable temperature drop. Beyond that threshold, any filament mass flowrate is thermally acceptable. This mass flowrate threshold shown in Figure 4.7(a) is rather small, and is likely to be met by any reasonably designed polymer AM process.

The standoff distance itself is an important design variable, which is usually chosen to be a small value. Figure 4.7(b) presents a colormap of temperature at the end of the standoff region as a function of ABS filament mass flowrate $\dot{m}$ and standoff distance L. Nozzle diameter of 0.4 mm and natural convection cooling conditions are assumed. Figure 4.7(b) shows that the computed temperature depends on both variables. There is a distinct region of large $\dot{m}$ and small $L$ where the temperature is very close to the nozzle tip temperature ($\theta$ close to 1). On the other hand, when mass flowrate is relatively small and the standoff distance is relatively large, there is significant temperature drop in the standoff region ($\theta$ close to 0). Figure 4.7(b) shows that a large standoff distance can be compensated somewhat by increasing the mass flowrate in order to meet the same thermal objective of a fixed temperature drop in the standoff region.

Design curves such as Figures 4.7(a) and 4.7(b) demonstrate the capability of the experimentally validated analytical model presented here for accurate thermal analysis of the process. This could be used for understanding and operating the process in a parameter space that ensures good thermal design. These design curves can also be used for understanding and optimizing trade-offs between thermal performance and other system-level objectives.

### 4.3.5. Validation of steady assumption

A key assumption made in the theoretical analysis presented in section 4.1 is that the filament temperature field in the standoff region remains steady. This is analogous to the steady state assumption commonly made in internal fluid flow analysis. In order to validate this assumption, the filament temperature field is measured at multiple times while the filament continues to be dispensed. Filament temperature is plotted as a function of the axial coordinate, $x$, for multiple times in Figure 4.8(a), showing that while the filament temperature changes with $x$,

there is no appreciable change in filament temperature with time. For further validation of the assumption of steady temperature, the filament temperature is measured as a function of *x* at multiple times for two different filament speeds. These data, plotted in Figure 4.8(b) show that at both speeds, the temperature vs. *x* plot remains invariant with time. This further confirms a key assumption underlying the theoretical model.

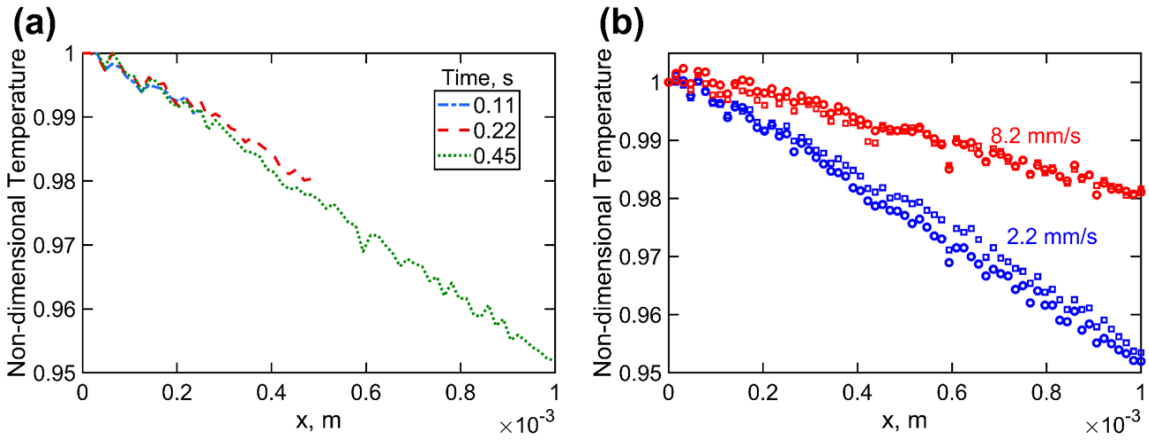


Figure 4.8 Validation of steady state assumption: (a) Measured filament temperature in the standoff region as a function of x at four different times. (b) Filament temperature in the standoff region as a function of x measured at two different times (shown as circles and squares) for two different speeds.

# CHAPTER 5

## Measurement of the in-plane temperature field on the build plate during polymer extrusion additive manufacturing using infrared thermometry

## Introduction

The process of filament-to-filament adhesion during polymer extrusion additive manufacturing (AM) is critically influenced by temperature distribution around the filament. Direct measurement of temperature distribution around the filament being deposited is, therefore, important for fully understanding this critical process. While past papers have reported side-view (x-z) temperature measurement using infrared (IR) thermography, this paper presents measurement of the in-plane (x-y) temperature field on the build plane by infrared thermography carried out from under the build plate. A small part of the build plate is replaced by an infrared-transparent window. In conjunction with an infrared right-angle prism mirror positioned underneath, direct measurement of in-plane temperature distribution is carried out with an infrared camera. With a thin graphite coating on the build plate, in-plane temperature field on the build plane is obtained, whereas experiments without the graphite coating result in direct measurement of the filament temperature distribution. Bottom-view measurements are shown to agree well with side-view measurements. Temperature fields on the build plate are measured as functions of time for single-line and multi-line printing. A few key features revealed by measurements include symmetrical and asymmetrical temperature distributions for single and multi-line printing, respectively, upstream-downstream asymmetry, and the thermal influence between lines being limited only to the adjacent line. The in-plane temperature measurement approach complements past side-view measurements, and improves upon our understanding of thermal phenomena during polymer AM.

## 5.1. Experimental Setup

### 5.1.1. Additive Manufacturing Platform

An open source Anet A8 3D printer is used in this work, using 1.75 mm diameter, black color Acrylonitrile butadiene styrene (ABS) filament. The layer height is 0.4 mm and nozzle diameter is 0.4 mm. The nozzle is heated up to 230 °C, while the print bed is maintained at 88 °C. The 3D printer is modified to accommodate optical access to the platform bed. The platform bed comprises a 6.20 mm thick Aluminum plate, in which a small, 12.70 mm diameter through-hole with 3.20 mm step is drilled. Bed heating is provided by 20 BNC Nichrome wire folded into nine turns and sandwiched between Kapton tape to form a 3.8 Ω resistive heater, which is attached to the platform bed using adhesive. NTC 3950 100K Ohm thermistor is attached to the bed to monitor and control the bed temperature. Two layers of cardboard are provided on the back side of the bed for thermal insulation, with a through-hole provided for optical access. One layer of Kapton tape is applied on the top surface of the bed to provide adhesion to the dispensed filament (ABS). The bed is installed on the 3D printer and elevated using a threaded rod. The bed is leveled by adjusting the elevation at five points – four corners and center – such that a sheet of paper slides through with minimum resistance.

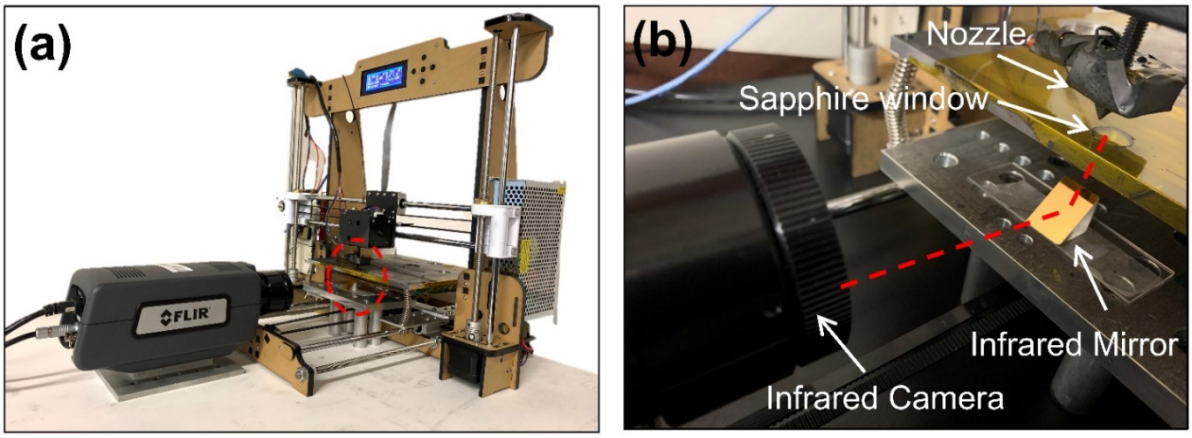


Figure 5.1 Pictures of the experimental setup for measurement of in-plane temperature distribution on the print bed. (a) presents a picture of the overall experimental setup, and (b) presents a zoomed-in picture showing the IR-transparent window, IR mirror and IR camera lens. Optical path from the build plane to the IR camera is shown schematically with a broken line.

### 5.1.2. Infrared thermography setup and calibration

A 12.70 mm diameter IR-transparent Sapphire window is placed in the through-hole in the print bed described in the previous sub-section. A right-angled, gold-coated infrared mirror is placed directly under the Sapphire window. A FLIR A6703sc infrared camera is aligned with the mirror. The camera operates in the 3.0-5.0 µm wavelength range with a spatial resolution of 37 µm and frame rate of 60 Hz.

Figure 5.1 presents a picture of the experimental setup, showing the build plate with an IR-transparent Sapphire window, an IR mirror directly underneath and an IR camera placed horizontally across the mirror. The optical path for the infrared signal is shown with a broken red line. Experiments are carried out both with and without a thin (< 1 µm) graphite layer sprayed on the build plate. Since graphite is opaque to infrared radiation, the presence of graphite enables measurement of temperature on the build plane. On the other hand, experiments without the graphite layer directly measure temperature of the filament above the build plane. Since the

graphite is very thin, it has negligible thermal mass, and does not impact the temperature field itself.

Note that a key general limitation of the present approach of measuring temperature distribution from the bottom is that only temperature on the build plate is accessible. Temperature distribution in further layers in case of multi-layer printing can not be determined due to the IR-opaque nature of filament material.

Calibration of the measured infrared signal is a critical process that affects the accuracy of temperature measurements. Since infrared emission passes through a complicated path including the IR-transparent window and IR mirror, it is important to carry out calibration in identical settings as the actual experiment. There are two possible approaches for calibration – infrared intensity could be measured at multiple known temperatures in order to create a look up table to be used to convert measured infrared intensity during actual experiments to temperature [41]. Alternately, the emissivity of the surface of interest could be determined such that there is best-possible agreement between a set of known temperatures and predicted temperatures corresponding to each [45]. In the present case, the latter approach is used due to good linearity observed in calibration data. In calibration experiments, the Instec HCS662V hot stage capable of being maintained at desired temperatures is placed on the platform bed in such a way that the stage and IR window are aligned. A K-type thermocouple is used to measure temperature of top surface of the stage. Measurements are carried out in 70-240 oC range, which covers the entire temperature range expected during actual experiments. Sufficient time is provided to reach steady state at each temperature, following which, the infrared intensity in measured. The hot stage is coated with the same graphite spray and covered with Kapton tape that are also used on the platform bed during actual experiments. Emissivity of the graphite film covered with Kapton tape

is determined by comparison of infrared-based temperature with thermocouple-based measurement over the entire temperature range of calibration. A separate calibration experiment is carried out using a pre-fabricated ABS sample, for use with filament temperature measurements without graphite. Calibration results are discussed in Section 5.2.7.

## 5.2. Results and Discussion

### 5.2.1. Thermal images

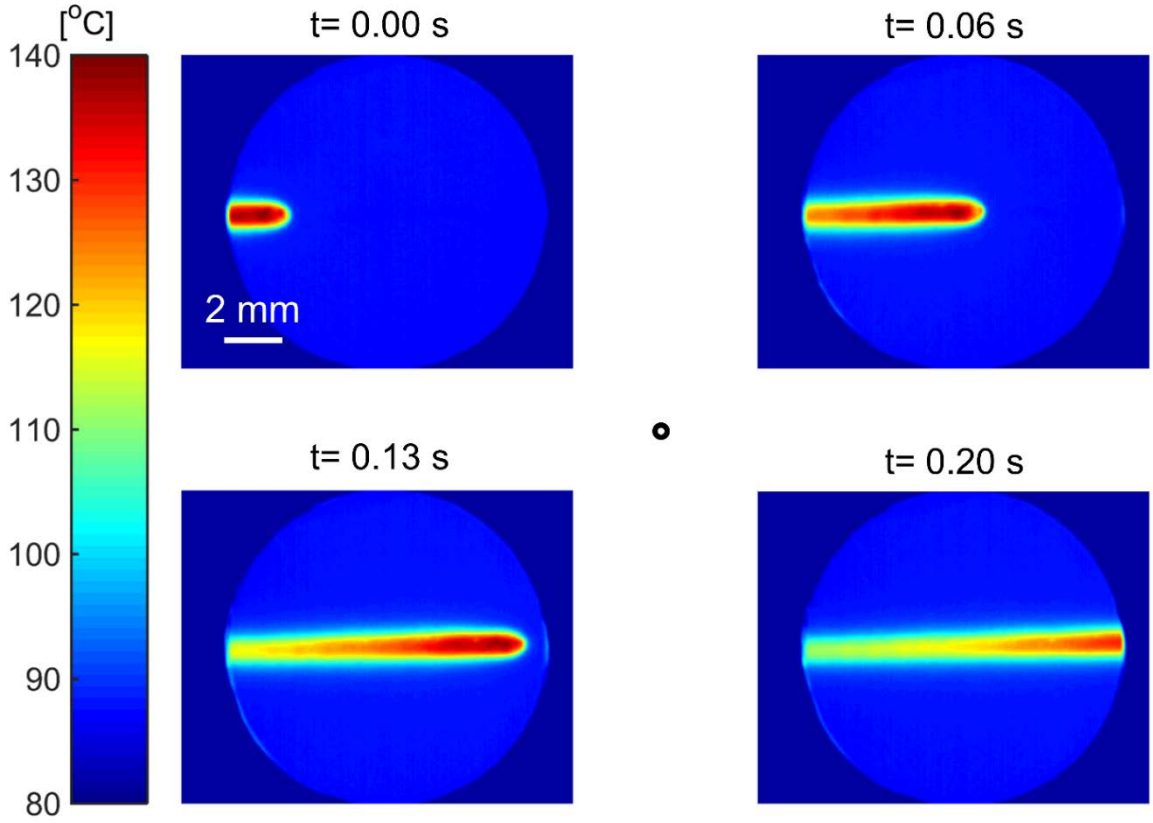


Figure 5.2 Measured temperature distribution on the build plane at four different times during single-line dispense from left to right across the viewing window at 3600 mm/min raster speed. For reference, the circle in the center represents the nozzle size.

This section presents measured colormaps of temperature fields during the polymer AM process. Detailed line plots of the temperature distribution are presented and discussed in section 5.2.4.

Figure 5.2 shows a succession of build plate temperature distribution at multiple times for single-line printing, where the nozzle rasters from left to right at 3600 mm/min speed. Emissivity calibration for graphite is used in Figure 5.2. The circular, light-blue region in these images is the IR-transparent window on the build plate through which the imaging is carried out. The nozzle size is shown as a circle for comparison. These images clearly capture the temperature distribution in the xy build plane, showing the motion of the peak temperature as the nozzle traverses from left to right. There is a significant temperature distribution behind the nozzle, with very little impact upstream. These are both consistent with results from moving heat source theory [29]. There is also a strong temperature gradient in the y direction. The zone of influence in the y direction is limited to around 2 mm.

In contrast with Figure 5.2 that presents temperature distribution on the build plane, Figure 5.3 presents thermal images without the IR-opaque graphite layer on the build plane. In this case, the IR camera directly measures temperature distribution on the filament. In addition to the filament, the nozzle is also visible as it moves from left to right. Filament temperatures reported in Figure 5.3 are significantly greater than print bed temperatures in Figure 5.2, as expected. Note that the thermal images in Figure 5.3 are calibrated based on separately-measured emissivity of ABS. As a result, the temperature field displayed in Figure 5.3 for regions other than the ABS filament may have some error.

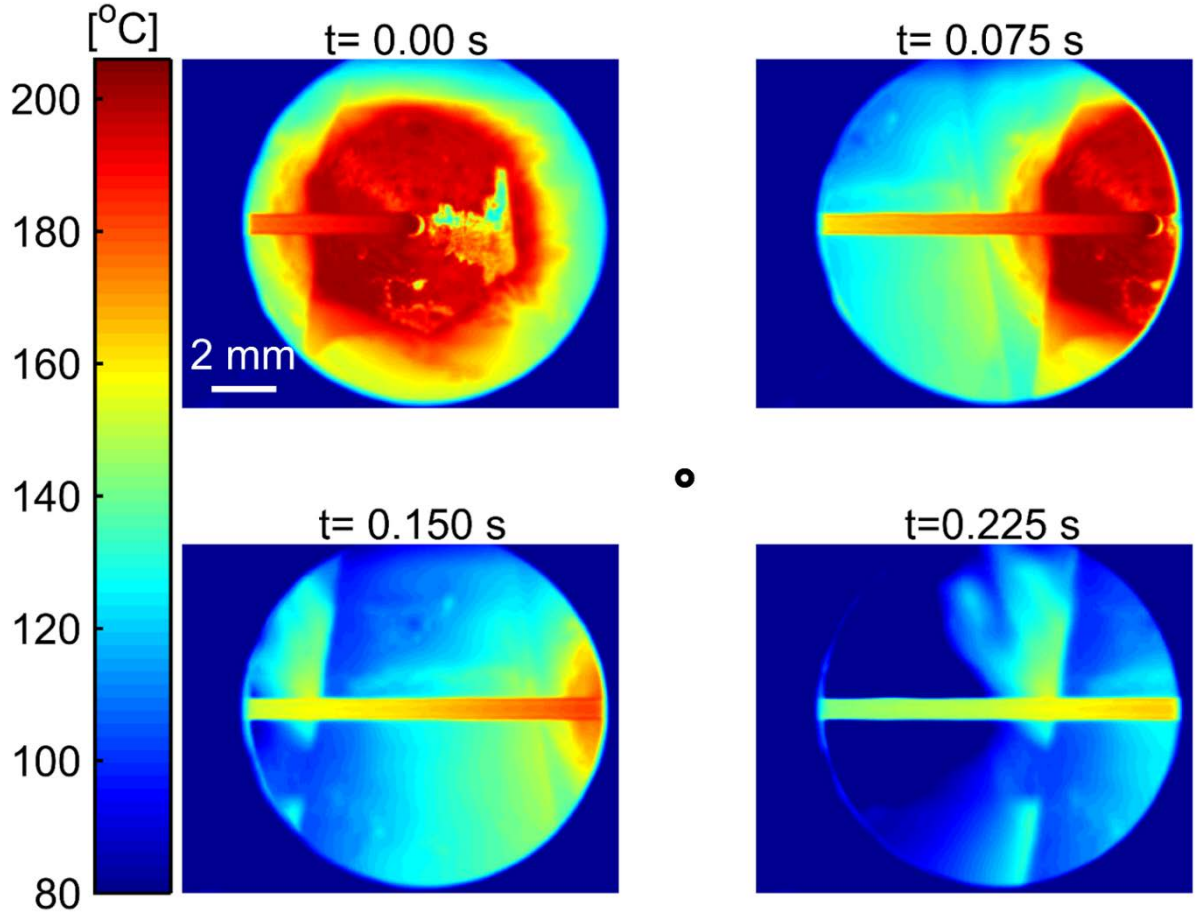


Figure 5.3 Measured temperature distribution without graphite layer on the build plate, which facilitates measurement of filament temperature. Process conditions are identical to Figure 3.

For further demonstration of the capability to measure the in-plane temperature field on the print bed, Figures 5.4(a)-(d) present similar succession of IR thermal maps for a case where the nozzle takes a U-turn to print the next line. The line-to-line gap is 0 μm in this case, and nozzle moves at 3600 mm/min. The U-turn taken by the nozzle is quite apparent by following the head of the temperature distribution in this case.

Finally, Figure 5.5 illustrates a more complicated printing pattern, where the nozzle is programmed to follow a circular path. The corresponding circular nature of the temperature distribution can be seen clearly. Figure 5.5 demonstrates the capability of bottom-view in-plane temperature field measurement even when the nozzle follows a complicated geometry.

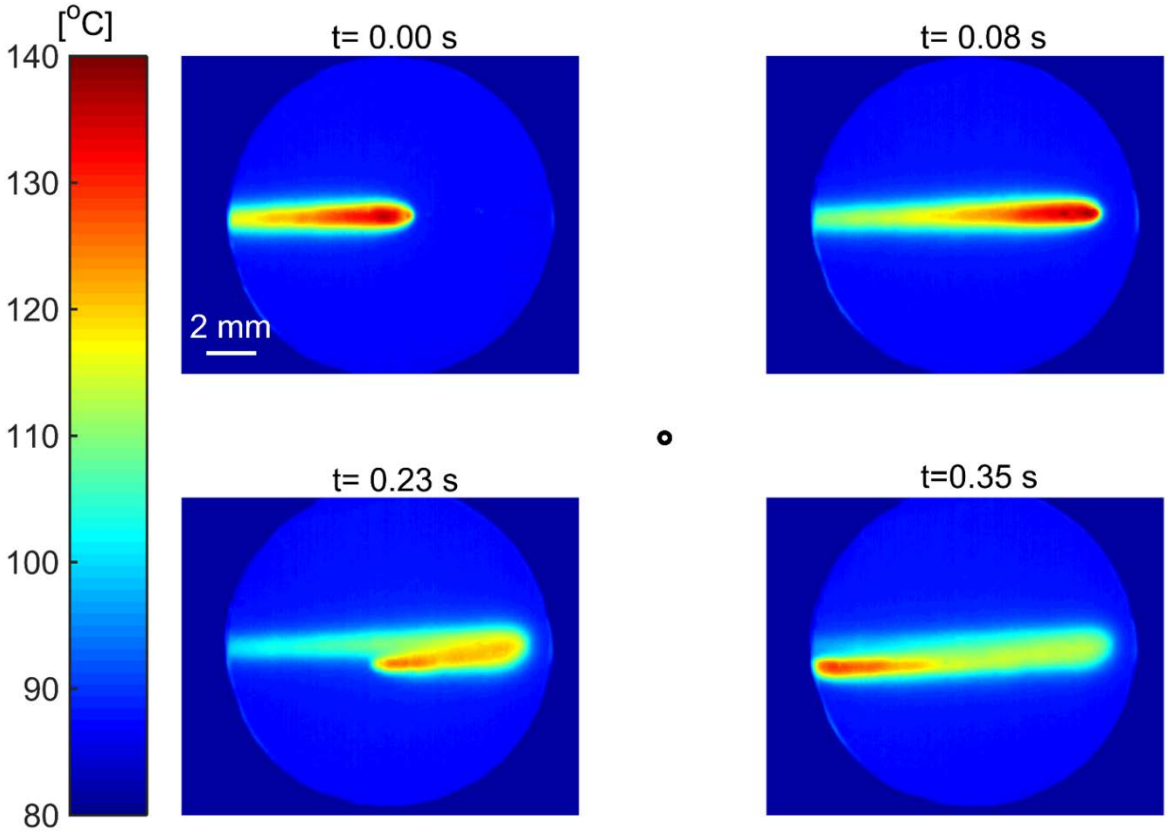


Figure 5.4 Measured temperature distribution on the build plane at four different times during two-line dispense where the nozzle move from left to right across the viewing window at 3600 mm/min raster speed and then takes a U-turn to print the second line.

Each of the thermal images shown in Figures 5.2-5.5 contain quantitative, experimentally measured temperature data. Such data may be extracted from transient temperature colormaps for a quantitative understanding of heat transfer during the rastering process, as discussed in Section 3.4. Further, the ability to measure the filament temperature from the bottom view offers an opportunity to validate the bottom-view measurements approach by comparison with filament temperature measurement from the side-view. This is discussed in Section 5.2.2.

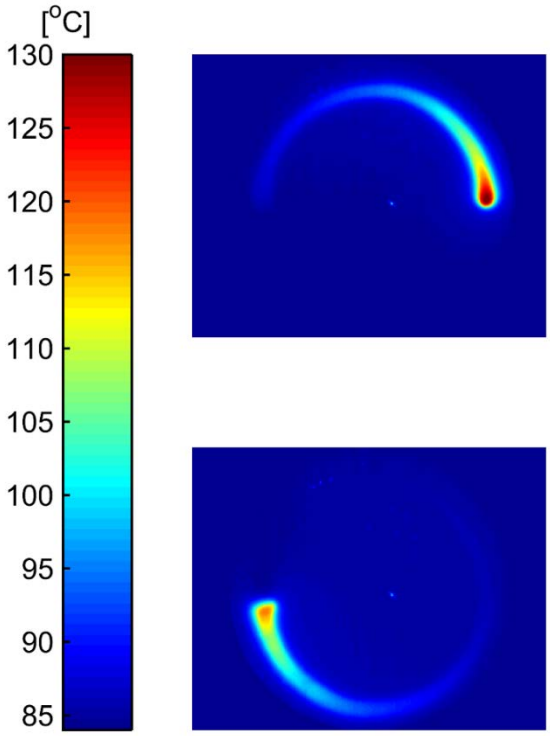


Figure 5.5. Measured temperature distribution on the build plane at two different times during dispense in a circular path at 2500 mm/min.

5.2.2. Validation of bottom-view measurement by comparison with side-view measurement

In the absence of graphite coating on the print bed, the bottom-view approach facilitates measurement of the filament temperature and its evolution with time, such as shown in Figure 5.3. It is of interest to compare such measurements against side-view measurements in order to validate the bottom-view measurement approach. To do so, temperature as a function of time at a specific point on the filament is extracted from the bottom-view measurement shown in Figure 5.3. The printing process is repeated with the same process parameters, but with the infrared camera positioned sideways in order to measure the filament temperature from the side. Figure 5.6 compares temperature as a function of time at a point on the filament measured with the bottom-

view and side-view approaches. There is good agreement between the two independent approaches for filament temperature measurement, with both curves decaying at roughly the same rate.

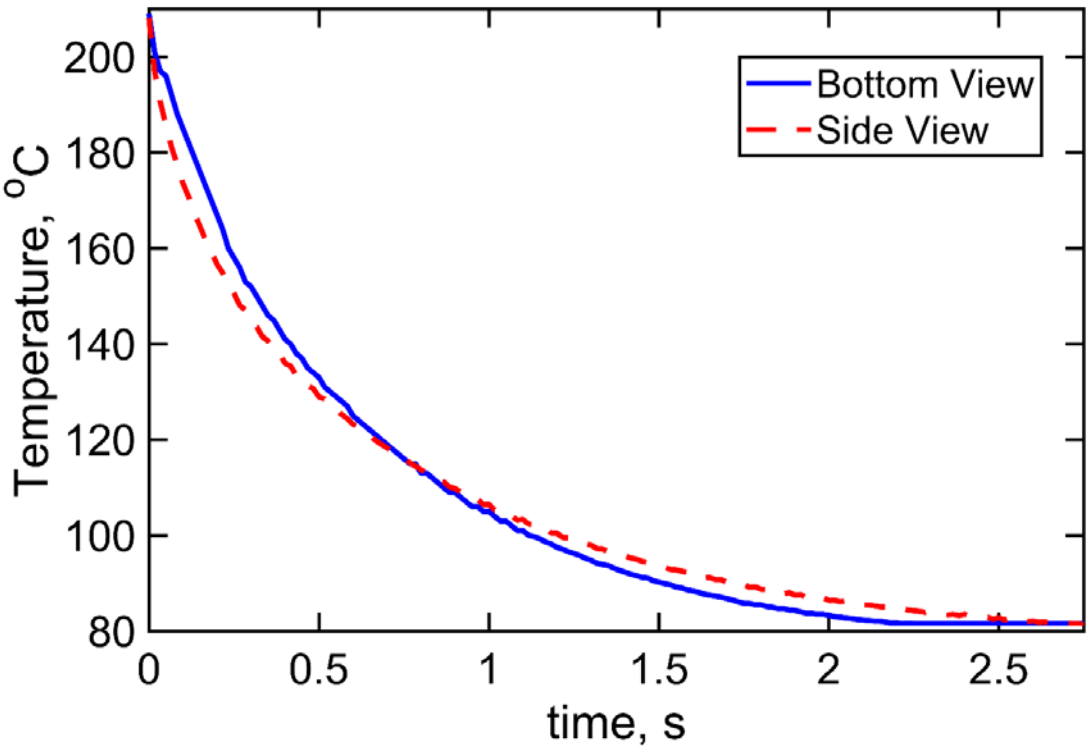


Figure 5.6 Comparison of temperature decay with time at two points on the filament for bottom-view and side-view measurements.

5.2.3. Comparison of experimental data with thermal model

Experimental data for temperature distribution on the build plane during nozzle rastering are compared with a heat transfer model based on moving heat source theory. This model accounts for diffusion of thermal energy deposited along with the hot filament [45] and predicts the temperature distribution on the build plane as a function of space and time, assuming constant thermal properties of the substrate. Energy deposited on the substrate is estimated by integrating the temperature-dependent heat capacity of ABS. Enthalpy of glass transition is included in the

calculation. The raster speed is taken to be 3600 mm/min, which matches the experimental conditions in Figure 5.2. Figure 5.7 presents temperature colormaps from the thermal model at three different times while the nozzle rasters from left to right. For comparison, the corresponding colormaps from experimental measurements for the same process parameters is shown in Figures 5.2(a)-(c). Note that the circle in experimental data corresponds to the IR-transparent Sapphire window, within which, measurements are taken.

A comparison of Figure 5.7 with Figure 5.2 shows reasonable agreement between the experimental data and thermal model, with the trends in the thermal model matching the experimental observations. Both predict a trailing off of the temperature behind the moving nozzle. The width of the thermal zone of influence in the y direction is also similar for measurements and model. In general, the predicted temperature is a little lower than observed experimentally, which may be due to the presence of the low thermal conductivity Kapton tape in the experiments, which is not accounted for in the moving heat source model.

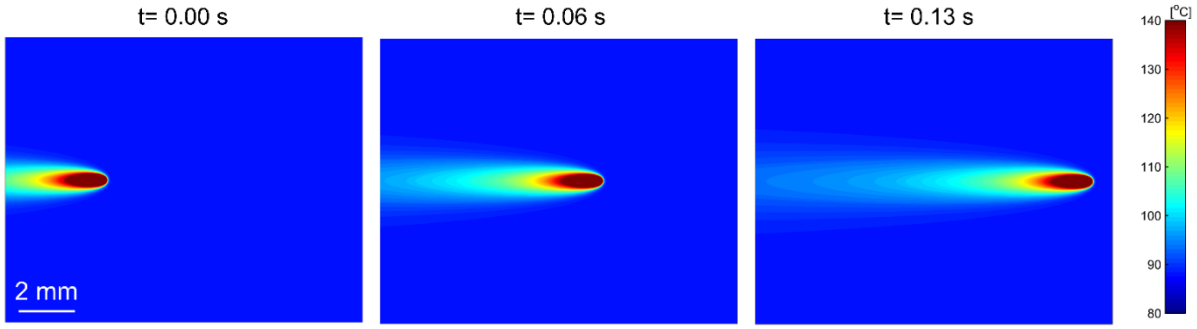


Figure 5.7 Prediction of in-plane temperature distribution during single line rastering based on a moving heat source thermal model. Process parameters are the same as for Figure 5.2.

Note that there are several limitations in the thermal model that may influence the extent of agreement with experimental measurements. Variation of thermal properties of the substrate with temperature is neglected. Thermal properties of Sapphire are not well-known at high temperatures,

and are estimated using limited available data [54]. The model neglects convective heat loss from the print bed to the surrounding air, as well as heat transfer from the hot nozzle to the print bed. The latter may be negligible in the present experimental conditions due to the high nozzle speed. Further, the thermal model neglects the presence of the thin Kapton tape due to difficulties in modeling a moving heat source in a two-layer body. This may be largely reasonable due to the very thin Kapton tape compared to the Sapphire thickness, but may affect the predicted spread of temperature field. Within these limitations, the consistency of experimental measurement of the in-plane temperature distribution with the thermal model is encouraging and provides validation of the experimental approach for measurement of in-plane temperature distribution.

Extraction of quantitative thermal information from thermographs obtained from bottom-view measurements, such as those shown in Figures 5.2-5.5, is discussed in subsequent sub-sections.

### 5.2.4. Temperature distribution in x and y directions: Single line printing

Figure 5.8 plots print bed temperature as a function of y at a fixed location along the raster line at multiple times. Plots before and after t=0, when the nozzle reaches the y axis are presented in Figures 5.8(a) and 5.8(b), respectively. Figure 5.8(a) shows a slow increase in temperature initially, followed by a rapid change as the nozzle approaches the y axis. There is some upstream influence of the rastering nozzle as seen by temperature rise even before the nozzle reaches the y axis. Also note the very rapid rise in temperature along the y axis as the nozzle gets close. There is dramatic temperature rise between t=-0.03 s and t=0.00 s, which correspond to successive frames captured at about 60 frames per second.

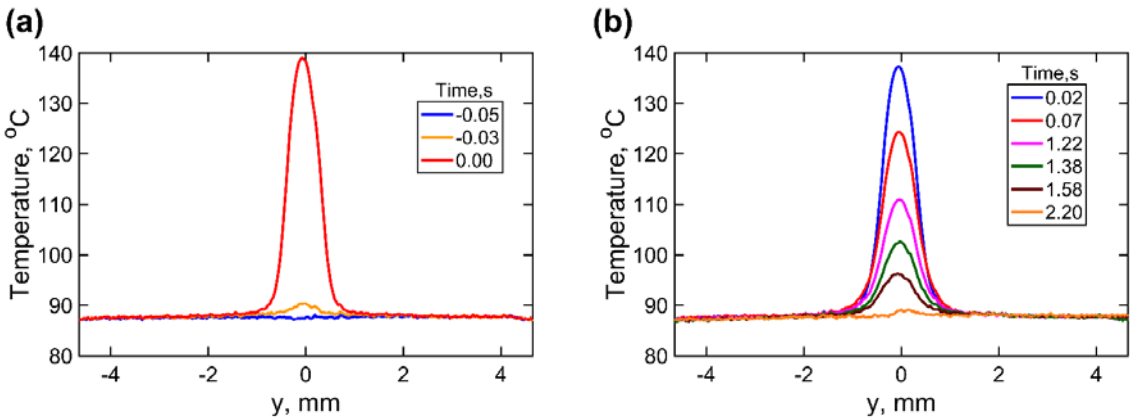


Figure 5.8 Measured build plane temperature distribution in the y direction at multiple times during single-line rastering along the x axis at 3600 mm/min. (a) and (b) present plots at multiple times before and after nozzle passes over the y axis at t=0.

The highest temperature is measured when the nozzle is directly above the y axis along the raster line. The thermal zone of influence is limited to around 2.0 mm around the raster line – beyond this zone, no thermal influence of the rastering process is observed. The region that experiences a temperature greater than the glass transition temperature is even narrower.

Temperature plots after the nozzle has crossed the y axis are shown in Figure 5.8(b). These plots are characterized by a gradual drop in temperature, taking around 1.2 seconds for the peak temperature to drop below glass transition temperature. Within around 2.2 seconds, the thermal influence of the rastering process disappears completely.

In each plot in Figures 5.8(a) and 5.8(b), there is excellent symmetry in the measured temperature distribution about the x axis. This is expected since this is a single-line rastering experiment, and therefore, there is no influence from neighboring pre-deposited lines that might still be hot. Results from two-line rastering experiments are discussed in subsequent Figures.

Plots of temperature distribution along the raster line are presented in Figure 5.9(a) and 5.9(b). Plots prior to the nozzle reaching the y axis are presented in Figure 5.9(a), while those afterwards are presented in Figure 5.9(b). At any time prior to the nozzle reaching the y axis, there is strong upstream-downstream asymmetry, with a sharp, linear region behind the nozzle and sudden drop in temperature ahead of the nozzle. This is consistent with dominance of thermal advection over thermal diffusion, in this case, due to relatively large nozzle speed and low thermal diffusivity of the print bed. The location of the temperature peak moves, as expected, corresponding to nozzle motion from left to right. However, the peak temperature does not change appreciably over time behind the nozzle. The cooling down process along the x axis after the nozzle has passed is presented in Figure 5.9(b), showing gradual reduction in temperature over time. Within around two seconds, the region plotted in Figure 5.9(b) completely cools down to the temperature of the print bed.

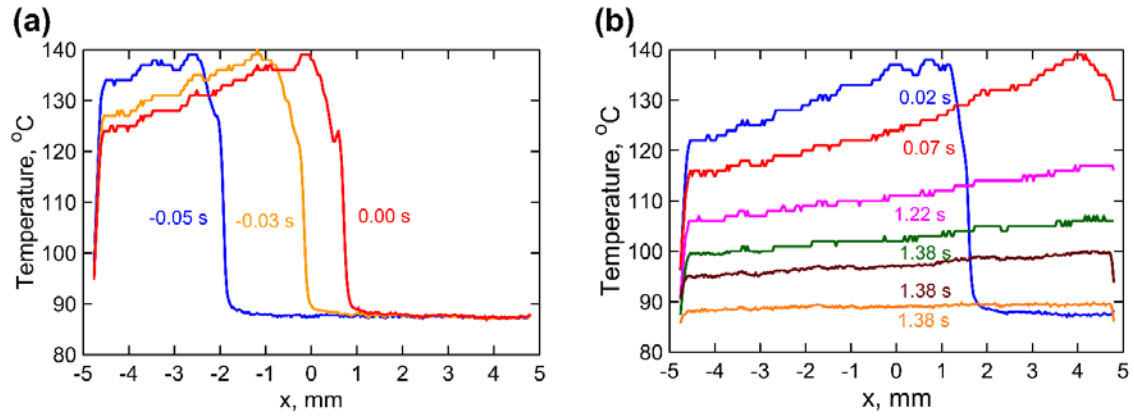


Figure 5.9 Measured build plane temperature distribution in the x direction along the raster line at multiple times during single-line rastering along the x axis at 3600 mm/min. (a) and (b) present plots at multiple times before and after nozzle passes over the y axis at t=0.

In conjunction with measurement of the in-plane temperature field on the build plate, temperature distribution on the filament surface is also measured as a function of time. Figure 5.10 plots these data as a function of time, starting at t=0 just after filament deposition. As expected, the

temperature reduces with time over the entire filament surface. Figure 5.10 shows that while there is some gradient in the temperature distribution across the filament, the filament temperature becomes more and more uniform as it decays with time.

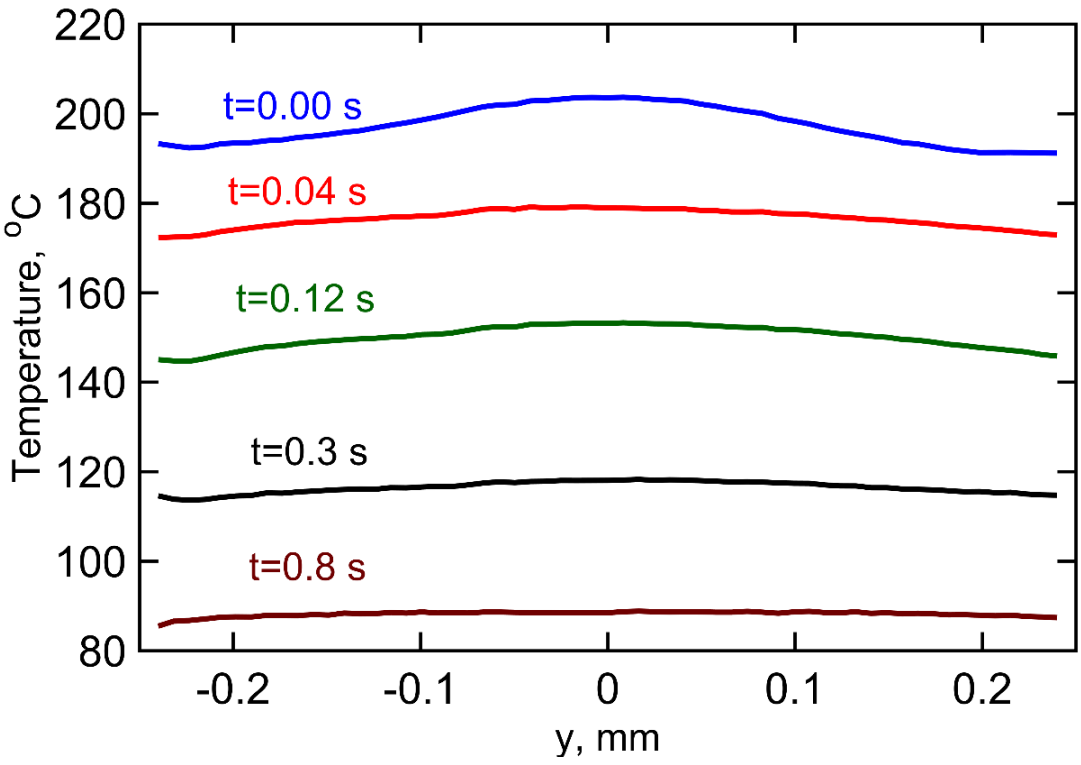


Figure 5.10 Measured temperature distribution across the filament at multiple times, starting at deposition (t=0).

5.2.5. Temperature distribution in y direction: Multi-line printing

The previous sub-section discussed single-line rastering experiments that are shown to exhibit strong symmetry about the x axis in Figure 5.8. Multi-line printing is an important process, as it may help understand filament-to-filament adhesion between in-plane neighbors. Measurements of temperature of filament-to-filament interface as well as the print bed during multi-line printing is discussed next.

Temperature at the filament-to-filament interface is of specific interest because this temperature governs the extent and quality of bonding between the two filaments. Specifically, this interface must remain above glass transition temperature for as long as possible [55,56]. Past papers have reported this critical temperature as a function of time for the interface between neighboring filaments in the build (z) direction. Similar to neighbors in the build direction, good bonding between in-plane neighbors is also critical for good properties of the built part. Using bottom-view measurement, Figure 5.11 plots the measured interface temperature between filaments that are in-plane neighbors as a function of time. These curves are plotted for three different values of the filament-to-filament gap. As expected, the interface temperature is the highest – and decays at the lowest rate – when the filaments are closest to each other, at a 0 μm gap. The rate of decay is larger for the other two gaps investigated here. Considering the glass transition temperature of 106 °C for ABS, the interface for the 0 μm case remains above glass transition for around 0.25 s. Figure 5.11 also shows an even shorter time above glass transition when the filament-to-filament gap is greater than 0 μm. The measured time above glass transition, even for the 0 μm gap case, is lower than reported by Seppala and Migler [41]. This is likely due to several reasons – firstly, Seppala and Migler reported this for neighboring filaments in the build direction, whereas the present work investigates in-plane neighbors. In their case, the recently printed, underlying layers may have been warm, whereas in the present case, the underlying layer is the print bed itself. Further, the print bed was set at 110 °C by Seppala & Migler, whereas it is set at 88 °C in the present work.

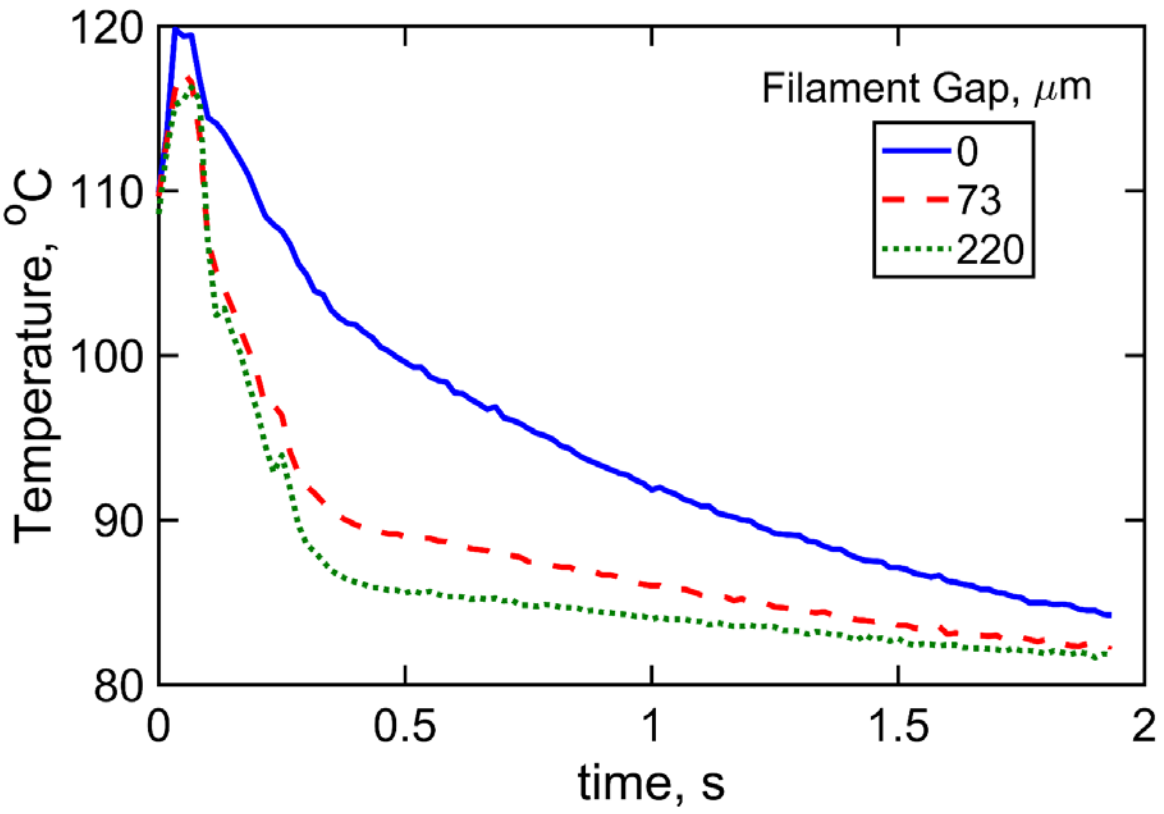


Figure 5.11 Measurement temperature of the interface between in-plane neighboring filaments as a function of time for three different filament-to-filament gaps.

Figure 5.12 presents build plate temperature along the y axis for two-line printing, where the nozzle takes a U-turn at the end of the first line to dispense the second line with a gap of 0 μm between lines. The location y=0 corresponds to the first raster line, whereas the second line is rastered at y=-0.590 mm. Data in Figure 5.12 are presented at multiple times starting at t=0.18 s, which corresponds to the nozzle reaching the end of the first line. At this point, Figure 5.12 shows a symmetric temperature distribution, as expected. Once the nozzle turns around and returns towards the y axis, a peak develops around y=-0.590 mm, corresponding to the second line. The temperature of the first raster line is still decaying, which results in a two-peak temperature distribution at t=0.22 s. The peak corresponding to the first raster line is relatively smaller, and

decays rapidly, so that by the time the temperature at the second line peaks at around t=0.25 s, the thermal effect of the first line has nearly disappeared. Afterwards, the temperature distribution

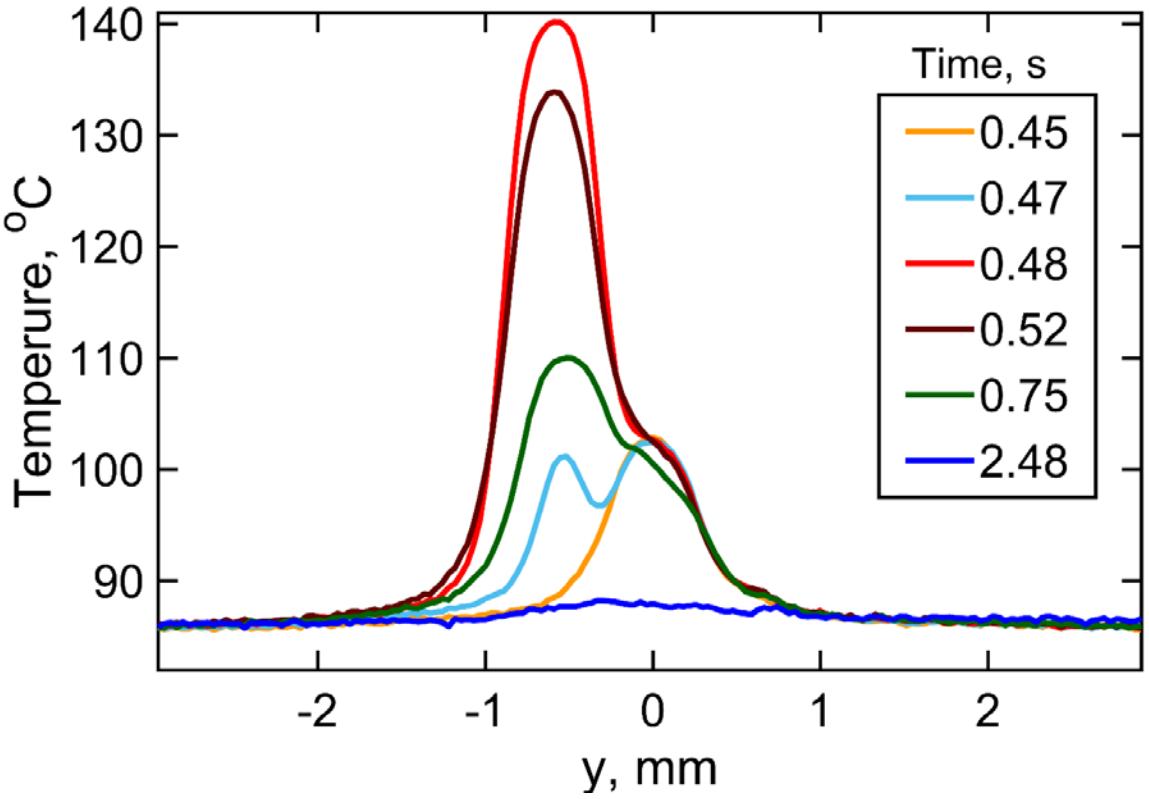


Figure 5.12 Measured build plane temperature distribution in the y direction at multiple times during double-line rastering of 28 mm length at 3600 mm/min. The line-to-line gap is 0 µm.

decays somewhat similar to Figure 5.8(b), except for the peak shifted to the location of the second raster line. The asymmetry in Figure 5.12 represents an overlap of the heating up of the second line and cooling down of the first line, and is in contrast with the symmetric temperature curves for single-line printing shown in Figures 5.8(a) and 5.8(b).

### 5.2.6. The role of the graphite layer

The graphite layer plays a key role in the measurements described here. Due to its IR-opaque nature, when sprayed on the print bed, it enables the infrared camera to measure the temperature field on the build plate. In the absence of the graphite layer, the infrared camera sees beyond the

print bed, and with emissivity calibration for ABS, measures the temperature distribution on the filament. In order to illustrate the key role of the graphite layer, experiments are carried out in which only the left half of the Sapphire window is sprayed with graphite. In such a case, the left half measures the build plate temperature distribution, while the right half simultaneously measures temperatures of surfaces beyond the build plane, including the filament. Figure 5.13 plots the measured temperature distribution at multiple times for 3600 mm/min raster speed. As expected, both in-plane temperature distribution (on the left) and filament temperature distribution (on the right) are obtained simultaneously. Note that temperature data for the left and right halves are obtained with separate emissivity calibrations – for graphite and ABS, respectively.

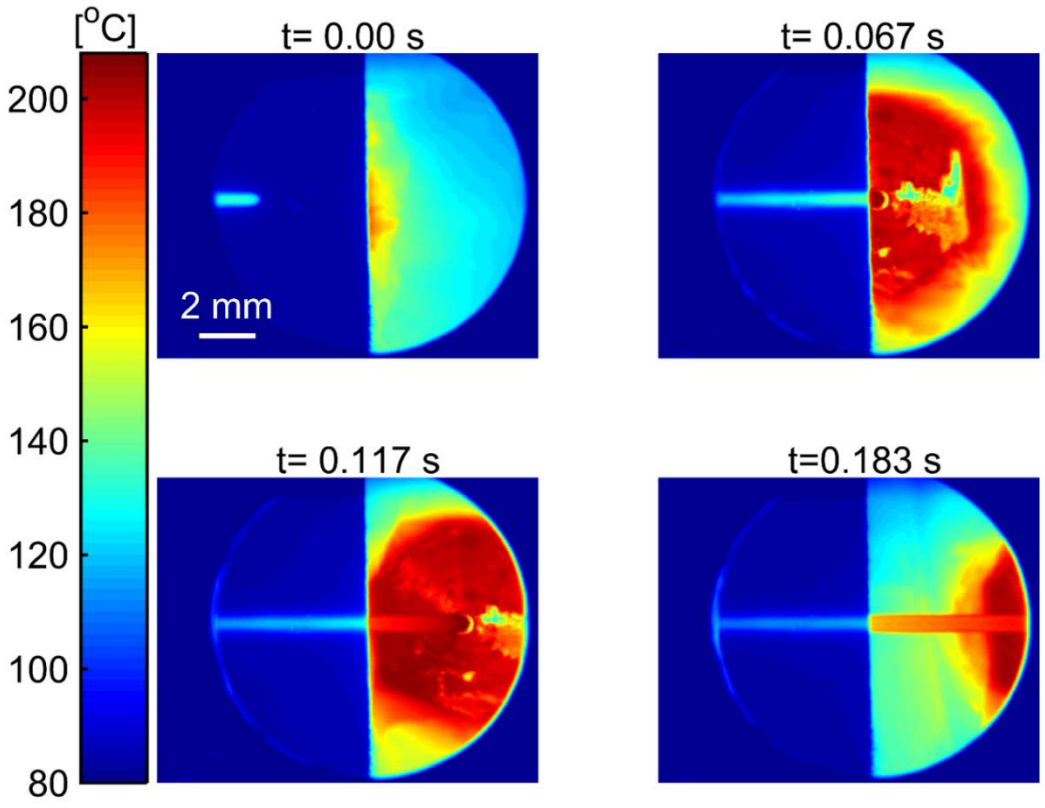


Figure 5.13 Measured temperature field when only the left half of the Sapphire window is sprayed with graphite. Colormaps are shown at four different times as the nozzle traverses at 3600 mm/min from left to right.

5.2.7. Calibration

Supplementary Figure S1 [57] plots results from calibration experiments described in Section 5.1.2. An emissivity value of 0.81 for the graphite film is found to be result in excellent agreement between the measured temperature and set temperature. Experimental data are linear and very close to the ideal 45° line shown in Supplementary Figure 5.14. Note that this calibration curve covers and goes beyond the temperature range expected in the actual experiments. A separate calibration experiment is carried out for the ABS material resulted in similar data, and used for experiments that measure the filament temperature.

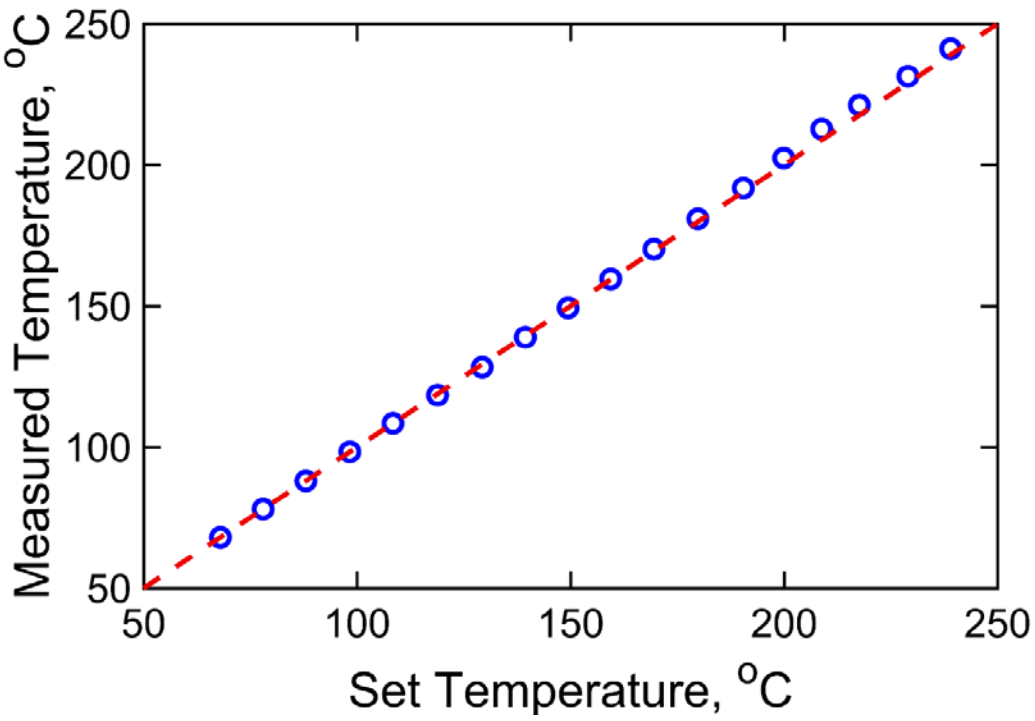


Figure 5.14. Comparison of set temperatures with infrared-measured temperature for calibration experiment.

5.2.8. Effect of Sapphire window

In the present experiments, a portion of the Aluminum bed is replaced with a Sapphire window to enable infrared thermography, which would not be possible with the IR-opaque Aluminum. It is

important to estimate the impact of use of the Sapphire window on the temperature field. Experiments are carried out to compare temperature rise during filament dispense on the Sapphire window with that on the Aluminum bed for the same process conditions. Since in-plane infrared thermography on the Aluminum bed is not possible due to the IR-opaque nature of Aluminum, temperature measurement in this comparison experiment is carried out using a thermocouple attached to the Sapphire or Aluminum, over which the filament is dispensed. Measured temperature as a function of time for both cases is presented in Supplementary Figure S2 [57]. Supplementary Figure 5.15 shows that the Sapphire window and Aluminum bed have similar thermal responses to the filament dispensing process. The nature of temperature decay is similar in both cases, although the peak temperature is somewhat different in the two cases. The measured peak temperature for Sapphire is somewhat lower than Aluminum, which may be due to slight differences in the positioning of the thermocouple bead with respect to the rastering filament, both of which are of comparable physical size. Also note that the temperature rise measured is lower than expected for both cases, which is likely because of the relatively large thermal mass of the thermocouple bead in comparison to the size of the rastering filament.

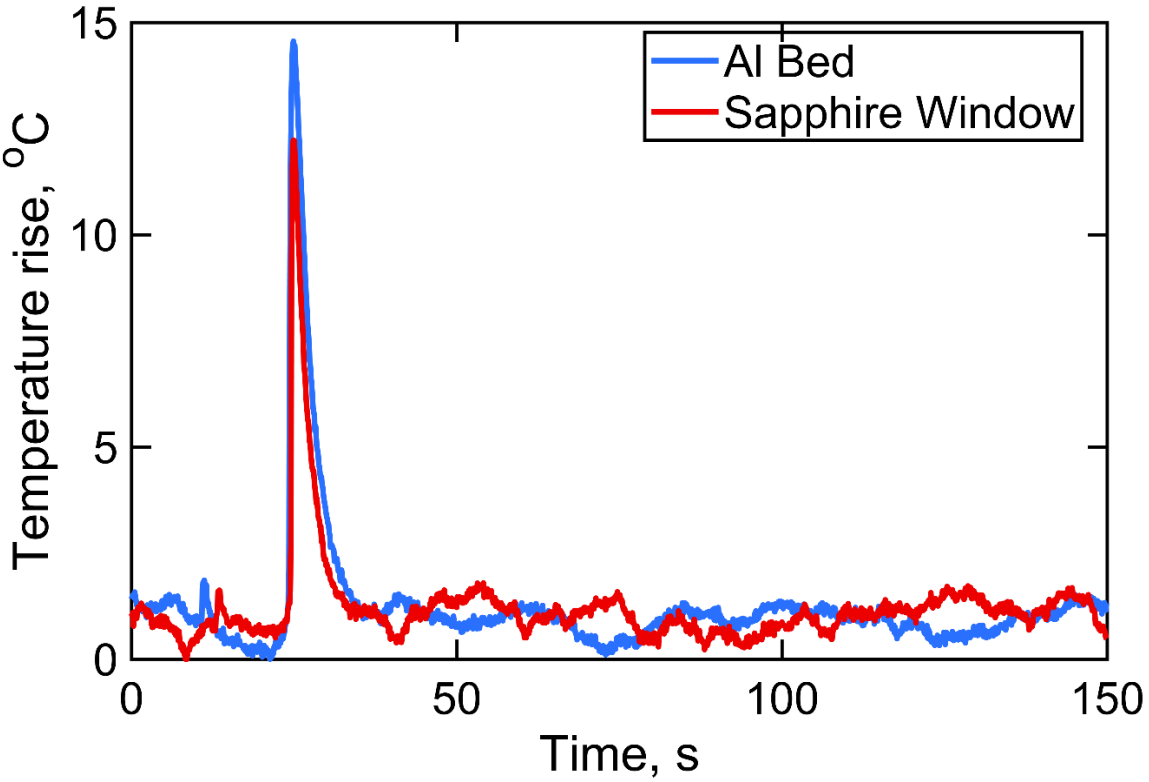

Figure 5.15. Comparison of thermocouple-measured temperature of Sapphire and Aluminum beds during the deposition of a single filament in identical conditions.

# CONCLUSIONS

In chapter 2, measurements of thermal conductivity of additively manufactured components, showing significant difference in the measured values in two orthogonal directions. Such anisotropy presents both challenges and opportunities, and regardless, must be accurately accounted for in design of additively manufactured components that must serve a thermal function. This paper shows that strong interfacial thermal contact resistance in the build direction is the fundamental reason for such anisotropy, and presents useful data on the dependence of this key parameter on process conditions. It is expected that the theoretical insights on thermal conduction in additively manufactured parts from this work, as well as experimental data on anisotropic thermal conductivity and interfacial thermal contact resistance will facilitate the use of additive manufacturing processes for building components with unique thermal properties.

In chapter 3, The annealing-driven enhancement reported here restores the thermal conductivity of the part to nearly the thermal conductivity of the underlying material. The theoretical model presented here provides key insights into the nature of annealing-driven enhancement, and is in good agreement with experimental data. Optimal design of the annealing process based on results discussed here may help improve thermal properties of polymer extrusion based parts, and facilitate the use of such parts in applications where significant heat loads are expected.

In chapter 4, an important and previously unaddressed heat transfer process in polymer extrusion based additive manufacturing processes through both experimental measurements and analytical modeling. Heat transfer processes in the standoff region play a key role in determining the filament temperature as it reaches the bed. Results from this work help identify the key process and material parameters that affect heat transfer in the standoff region. Two distinct regimes of heat transfer in the standoff region are identified based on the value of a single parameter that combines mass

flowrate, heat capacity, filament size and cooling conditions. The good agreement of the analytical model with experimental data is encouraging. Results presented here may help develop practical design tools to improve thermal performance as well as address tradeoffs between heat transfer and other performance parameters of extrusion based polymer additive manufacturing.

Chapter 5, It is important to contrast the present method and results with past work that reported side-view measurements of the temperature field [15, 16]. While side-view measurements provide thermal information about inter-layer filament bonding, the present work provides information about intra-layer filament bonding. Both bonding processes are important and contribute towards good thermal and mechanical properties of the printed part. Side-view measurements reported earlier and in-plane measurements reported in this work may be viewed as being complementary – together, they provide a more complete thermal picture of the polymer AM process than just by themselves.

A key limitation of the present work is that bottom-view measurement is limited to printing of the first layer only. Because bottom-view thermography requires an IR-transparent substrate, the method does not work well for subsequent layers when the material underlying the deposition process is the polymer itself, which is not transparent to IR. In such a case, some thermal information may be obtained using a side-view measurement, although measurements of the temperature between in-plane neighbors will be very challenging even with side view measurements.

This work complements previously reported infrared-based temperature measurements of polymer AM processes by measuring the in-plane view of the temperature field instead of the side-view. The additional information obtained through this work helps understand important thermal phenomena, such as in-plane filament-to-filament interface temperature, the extent of in-plane

thermal influence of a hot filament, as well as the impact of process parameters such as filament-to-filament gap on such thermal transport phenomena. It is expected that enhanced understanding of filament-to-filament adhesion driven by robust temperature field measurements will help design polymer AM process to produce parts with novel thermal and mechanical properties.

REFERENCES

[1] D. Dimitrov, K. Schreve, N. de Beer, 'Advances in three dimensional printing – state of the art and future perspectives,' *Rapid Prototyping J.*, **12**, 2006, pp. 136-147.

[2] D.T. Pham, R.S. Gault, 'A comparison of rapid prototyping technologies,' *Int. J. Machine Tools & Manufacture*, **38**, 1998, pp.1257–1287.

[3] J.-P. Kruth, M.C. Leu, T. Nakagawa, 'Progress in Additive Manufacturing and Rapid Prototyping,' *CIRP Annals Manufacturing Technology*, **2**, 1998, pp. 525-540.

[4] S. Bose, S. Vahabzadeh, A. Bandyopadhyay, 'Bone tissue engineering using 3D printing,' *Materials Today*, **12**, 2013, pp. 496-504.

[5] D.W. Hutmacher, 'Scaffolds in tissue engineering bone and cartilage,' *Biomaterials*, **21**, 2000, pp. 2529-2543.

[6] K.R. Hart, R.M. Dunn, J.M. Sietins, C.M.H. Mock, M.E. Mackay, E.D. Wetzel, 'Increased fracture toughness of additively manufactured amorphous thermoplastics via thermal annealing,' *Polymer*, **144**, pp.192-204, 2018.

[7] J. Kotlinski, 'Mechanical properties of commercial rapid prototyping materials,' *Rapid Prototyping Journal*, **20**, 2014, pp. 499-510.

[8] T. Osborn, E. Zhou, R., Gerzeski, D. Mollenhauer, G.P. Tandon, T.J. Whitney, E.V. Iarve, 'Experimental and Theoretical Evaluation of Stiffness Properties of Fused Deposition Modeling Parts,' In: *American Society of Composites – 30$^{th}$ Technical Conference*, 2015.

[9] S. Sheth, R.M. Taylor, A. Adluru, 'Numerical Investigation of Stiffness Properties of FDM Parts as a Function of Raster Orientation,' *Proceedings of the Annual Solid Freeform Fabrication Symposium, Austin,* 2017.

[10] S.H. Ahn, M. Montero, D. Odell, S. Roundy, P.K. Wright, 'Anisotropic material properties of fused deposition modeling ABS,' *Rapid prototyping journal,* **8**, pp 248-257, 2002.

[11] H. Kim, E. Park, S. Kim, B. Park, N. Kim, S. Lee, 'Experimental Study on Mechanical Properties of Single- and Dual-Material 3D Printed Products,' *Procedia Manufacturing,* **10**, 2017, pp. 887–897.

[12] A.R. Torrado, D.A. Roberson, 'Failure Analysis and Anisotropy Evaluation of 3D-Printed Tensile Test Specimens of Different Geometries and Print Raster Patterns,' *J. Failure Analysis and Prevention,* **1**, 2016, pp. 154-164.

[13] C. Ziemian, M. Sharma, S. Ziemian, 'Anisotropic Mechanical Properties of ABS Parts Fabricated by Fused Deposition Modelling,' In: 'Mechanical Engineering', M. Gokcek (Ed.), InTech, 2012.

[14] A. Bellini, S. Guceri, 'Mechanical characterization of parts fabricated using fused deposition modeling,' *Rapid Prototyping J.*, **4**, 2003, pp. 252-264.

[15] Z. Weng, J. Wang,T. Senthil, Lixin Wu 'Mechanical and thermal properties of ABS/montmorillonite nanocomposites for fused deposition modeling 3D printing,' *Materials & Design*, **102**, 2016, pp. 276-283.

[16] K.-P. Weiss, N. Bagrets, C. Lange, W. Goldacker, J. Wohlgemuth, 'Thermal and mechanical properties of selected 3D printed thermoplastics in the cryogenic temperature regime', IOP Conf. Series: Materials Science and Engineering, **102**, 2015, pp. 012022.

[17] C. Shemelya, A. De La Rosa, A. Torrado, K. Yu, J. Domanowski, P. Bonacuse, R. Martin, M. Juhasz, F. Hurwitz, R. Wicker, B. Conner, E. MacDonald, D.A. Roberson, 'Anisotropy of thermal conductivity in 3D printed polymer matrix composites for space based cube satellites,' *Additive Manufacturing*, **16**, 2017, pp. 186-196.

[18] S.-Y. Chung, D. Stephan, M.A. Elrahman , T.-S. Han, 'Effects of anisotropic voids on thermal properties of insulating media investigated using 3D printed samples', *Construction and Building Materials*, **111**, 2016, pp. 529-542.

[19] D. Ravoori, L. Alba, H. Prajapati, A. Jain, 'Investigation of Process-Structure-Property Relationships in Polymer Extrusion Based Additive Manufacturing Through In Situ High Speed Imaging and Thermal Conductivity Measurements,' *Additive Manufacturing*, **23**, pp. 132-139, 2018.

[20] T. Sonsalla, A.L. Moore, W.J. Meng, A.D. Radadia, L.Weiss, '3-D printer settings effects on the thermal conductivity of acrylonitrile butadiene styrene,' *Polymer Testing*, **70**, pp. 389-395, 2018.

[21] W.D. Callister Jr., D.G. Rethwisch, '*Fundamentals of materials science and engineering: an integrated approach,*' John Wiley & Sons, 2012.

[22] M. G. Wyzgoski, "Effects of oven aging on ABS, poly(acrylonitrile-butadiene-styrene)," Polym. Eng. Sci., vol. 16, no. 4, pp. 265–269, Apr. 1976.

[23] M.D. Wolkowicz, S.K. Gaggar, 'Effect of thermal aging on impact strength acrylonitrile-butadiene-styrene (ABS) terpolymer,' *Polymer Engineering & Science*, **21**, pp.571-575, 1981.

[24] Y.H. Kim, R.P. Wool, 'A theory of healing at a polymer-polymer interface,' *Macromolecules*, **16**, pp.1115-1120, 1983.

[25] P.G. de Gennes, 'Reptation of a polymer chain in the presence of fixed obstacles,' *Journal of Chemical Physics*, **55**, pp.572-579, 1971.

[26] S. Mazur, 'Coalescence of polymer particles,' Polymer Powder Technology, New York: John Wiley & Sons, 1995.

[27] C. Bellehumeur, L. Li, Q. Sun, P. Gu, 'Modeling of bond formation between polymer filaments in the fused deposition modeling process,' *Journal of Manufacturing Processes*, **6**, pp.170-178, 2004.

[28] O. Pokluda, C. Bellehumeur, J. Vlachopoulos, 'Modification of Frenkel's model for sintering,' *AIChE journal*, **43**, pp. 3253-3256, 1997.

[29] Q. Sun, G.M. Rizvi, C.T. Bellehumeur, P. Gu, 'Effect of processing conditions on the bonding quality of FDM polymer filaments,' *J. Manufac. Process*, **14**, 2008, pp. 72-80.

[30] S.F. Costa, F.M. Duarte, J.A. Covas, 'Estimation of filament temperature and adhesion development in fused deposition techniques,' *J. Mater. Processing Technol.*, 245, 2017, pp. 167-179.

[31] A.K. Sood, R.K. Ohdar, S.S. Mahapatra, 'Experimental investigation and empirical modelling of FDM process for compressive strength improvement,' *J. Adv. Research*, **3**, 2012, pp. 81-90.

[32] M. A. Yardimci, S. Güçeri, ‘Conceptual framework for the thermal process modelling of fused deposition,’ *Rapid Prototyping J.*, **2**, 1996, pp. 26-31.

[33] J.H. Park, M.Y. Lyu, S.Y. Kwon, H.J. Roh, M.S. Koo, S.H. Cho, ‘Temperature Analysis of Nozzle in a FDM Type 3D Printer Through Computer Simulation and Experiment,’ *Elastomers and Composites*, **51**, 2016, pp.301-307.

[34] F. Peng, B.D. Vogt, M. Cakmak, ‘Complex flow and temperature history during melt extrusion in material extrusion additive manufacturing,’ *Additive Manufacturing*, **22**, 2018, 197-206.

[35] M.E. Mackay, Z.R. Swain, C.R. Banbury, ‘The performance of the hot end in a plasticating 3D printer,’ *J. Rheology*, **61**, 2017, pp. 229-236.

[36] J. Go, S.N. Schiffres, A.G. Stevens, A.J. Hart, ‘Rate limits of additive manufacturing by fused filament fabrication and guidelines for high-throughput system design,’ *Additive Manufacturing*, **16**, 2017, pp. 1-11.

[37] E.L. Gilmer, D. Miller, C.A. Chatham, C. Zawaski, J.J. Fallon, A. Pekkanen, T.E. Long, C.B. Williams, M.J. Bortner, ‘Model analysis of feedstock behavior in fused filament fabrication: Enabling rapid materials screening,’ *Polymer*, 2017, available at https://doi.org/10.1016/j.polymer.2017.11.068.

[38] A. Bellini, S. Guceri, M. Bertoldi, ‘Liquefier Dynamics in Fused Deposition,’ *J. Manufac. Sci. & Eng.*, **126**, 2004, pp. 237-246.

[39] J. Go, A.J. Hart, ‘Fast Desktop-Scale Extrusion Additive Manufacturing,’ *Additive Manufacturing*, **18**, 2017, pp. 276-284.

[40] D.D. Phan, Z.R. Swain, M.E. Mackay, ‘Rheological and heat transfer effects in fused filament fabrication,’ *J. Rheology*, **62**, 2018, pp. 1097–1107.

[41] J.E. Seppala, K.D. Migler, ‘Infrared thermography of welding zones produced by polymer extrusion additive manufacturing,’ *Additive Manufacturing*, **12**, 2016, pp. 71-76.

[42] H. Xia, J. Lu, S. Dabiri, G. Tryggvason, ‘Fully resolved numerical simulations of fused deposition modeling. Part I: fluid flow,’ *Rapid Prototyping J.*, **24**, 2018, pp. 463-476.

[43] D’Amico, A., Peterson, A., ‘An adaptable FEA simulation of material extrusion additive manufacturing heat transfer in 3D,’ *Additive Manufacturing*, **21**, 2018, pp. 422-430.

[44] A. Bendada, M. Lamontagne. ‘A new infrared pyrometer for polymer temperature measurement during extrusion moulding,’ *Infrared Phys. & Technol.*, **46**, 2004, pp.1-15.

[45] Ravoori, D., Lowery, C., Prajapati, H., Jain, A., ‘Experimental and theoretical investigation of heat transfer in platform bed during polymer extrusion based additive manufacturing,’ Polymer Testing, 73, pp. 439-446, 2019.

[46] V. Vishwakarma, C. Waghela, Z. Wei, R. Prasher, S.C. Nagpure, J. Li, F. Liu, C. Daniel, A. Jain, ‘Heat transfer enhancement in a Lithium-ion cell through improved material-level thermal transport,’ *J. Power Sources*, **300**, pp. 123-131, 2015.

[47] H. Prajapati, D. Ravoori, R.L. Woods, A. Jain, ‘Measurement of Anisotropic Thermal Conductivity and Inter-Layer Thermal Contact Resistance in Polymer Fused Deposition Modeling (FDM),’ *Additive Manufacturing*, **21**, pp. 84-90, 2018.

[48] M.A. Guitar, K. Woll, E. Ramos-Moore, F. Mücklich, 'Study of grain growth and thermal stability of nanocrystalline RuAl thin films deposited by magnetron sputtering,' *Thin Solid Films*, **527**, pp.1-8, 2013.

[49] X. Wang, L. Hu, K. Liu, Y. Zhang, 'Grain growth kinetics of bulk AZ31 magnesium alloy by hot pressing,' *Journal of Alloys and Compounds*, **527**, pp.193-196, 2012.

[50] J.E. Seppala, K.D. Migler, 'Infrared thermography of welding zones produced by polymerextrusion additive manufacturing,' *Additive Manufacturing*, **12**, pp.71-76, 2016.

[51] www.professionalplastics.com/professionalplastics/ThermalPropertiesofPlasticMaterials.pdf accessed 10/26/2018.

[52] F.P. Incropera, D.P. DeWitt, T.L. Bergman, A.S. Levine, Introduction to Heat Transfer, 5th ed., John Wiley & Sons, 2006.

[53] R.I. Tanner, 'A theory of die-swell revisited,' *J. Non-Newtonian Fluid Mech.*, **129**, 2005, pp. 85–87.

[54] M. Vollmer, K.-P. Möllmann, 'Infrared Thermal Imaging: Fundamentals, Research and Applications,' 2nd Ed., Wiley-VCH Verlag, 2017, ISBN: 9783527413515.

[55] Seppala, J. E., Hoon Han, S., Hillgartner, K. E., Davis, C. S., and Migler, K. B., 2017, "Weld Formation during Material Extrusion Additive Manufacturing," Soft Matter, 13(38), pp. 6761–6769.

[56] Yang, F., and Pitchumani, R., 2002, "Healing of Thermoplastic Polymers at an Interface under Nonisothermal Conditions," Macromolecules, 35(8), pp. 3213–3224.

[57] https://www.dupont.com/content/dam/dupont/products-and-services/membranes-and-films/polyimde-films/documents/DEC-Kapton-summary-of-properties.pdf, last accessed 3/26/2020

# BIOGRAPHICAL INFORMATION

Hardikkumar Prajapati received a Bachelor of Engineering in Mechanical Engineering from The Maharaja Sayajirao University of Baroda. Before coming to the USA, he worked as a Technical Sales Engineer at Aerzen Machine India Private Limited for two years. He started his Master of Engineering in Mechanical Engineering in Fall 2015 and finished in Fall 2016 from the University of Texas at Arlington (UT Arlington). Immediately after the Master of Engineering, he started his Ph.D. in Mechanical Engineering at the same university. He worked as a Module Engineering Intern at Intel Corporation during the Summer of 2018. His research at UT Arlington focused on the understanding of heat transfer phenomena in polymer extrusion-based additive manufacturing. In the near future, he aspires to pursue his career in industry.

Email: hardik.prajapati@icloud.com